

CHARACTERIZATION AND MODELING OF  
FERROMAGNETIC SHAPE MEMORY Ni-Mn-Ga IN A  
COLLINEAR STRESS-FIELD CONFIGURATION

DISSERTATION

Presented in Partial Fulfillment of the Requirements for  
the Degree Doctor of Philosophy in the  
Graduate School of The Ohio State University

By

LeAnn Faidley, B.S., B.S., M.S., M.S.

\* \* \* \* \*

The Ohio State University

2006

Dissertation Committee:

Marcelo Dapino, Co-Adviser

Gregory Washington, Co-Adviser

Stephen Bechtel

C.H. Menq

Approved by

---

Co-Adviser

---

Co-Adviser

Graduate Program in  
Mechanical Engineering

© Copyright by

LeAnn Faidley

2006

## ABSTRACT

Ferromagnetic Shape Memory Alloys (FSMAs) in the Nickel-Manganese-Gallium system have been shown to exhibit large magnetically induced strains of up to 9.5% due to magnetically driven twin variant reorientation. In order for these strains to be reversible, restoring stresses or magnetic fields need to be applied orthogonal to the drive field. This leads to a typical implementation of Ni-Mn-Ga in applications involving the use of electromagnets, which tend to be heavy, bulky and narrowband. This dissertation presents the investigation of the behavior of  $\text{Ni}_{50}\text{Mn}_{28.7}\text{Ga}_{21.3}$  in a unique configuration in which a magnetic field produced by a solenoid is applied along the axis of a cylindrical rod and the strain is measured *collinearly* to the field while axial loads are applied. A strain mechanism is proposed where imperfections and inclusions in the sample create internal stresses that provide the restoring forces while also limiting the maximum strain from the sample by limiting the motion of the twin boundaries. This mechanism explains the presence and reduced magnitude of the -0.41% quasi-static strain that has been measured in this sample in the collinear configuration. This dissertation also expands the experimental testing of Ni-Mn-Ga into the dynamic domain most usually found in applications through a set of swept-sine tests. These tests demonstrate a 250% shift of elastic modulus with applied dc bias field that makes these materials extremely promising for variable stiffness applications. Finally, this document presents a model for the strain of Ni-Mn-Ga.

A Gibb's Free Energy approach is used to describe an idealized hysteresis kernel that does not account for the inhomogeneities in pinning site strength and internal field. A stochastic homogenization method is then implemented that estimates the inhomogeneities as probability distributions. The implementation and testing of this model is discussed in detail and results showing simulations that fall within 3% of the data are presented demonstrating the power of this method for future design and control of applications for Ni-Mn-Ga in solenoid based transducers.

This dissertation is dedicated to the community of faith at Buckeye Lutheran Campus Ministry and its extension into IMOK, LSM, NSI, and UIA. Without the loving support and encouragement of my brothers and sisters in these families this work would never have been completed and without the growth opportunities provided by these organizations I would not be who I am today.

Thank you.

## ACKNOWLEDGMENTS

I would like to take this opportunity to thank my advisors and other committee members for their guidance, assistance, and support throughout the past five years. Dr. Dapino's technical knowledge was of great assistance and his enthusiasm for the project and the puzzles that went with it was very refreshing. Dr. Washington's support, mentorship, and faith in me kept me going when I felt like giving up and his excitement about seeing where my project could go and for finding the answers to the questions taught me much about the research process. Dr. Bechtel, Dr. Menq, and Dr. Sanders' assistance was very valuable and their patience was much appreciated. In addition Dr. Lograsso at Iowa State University and Dr. Smith at University of North Carolina were extremely helpful and I am very thankful for their insights.

My funding for this work was provided by The Ohio State University and by the Ohio Space Grant Consortium. I am very appreciative of their support. The program run by OSGC was an incredible experience and the encouragement provided by the many people I met at OSGC symposiums was a model for my future interaction with younger students.

My years at OSU would certainly not have been this same without the wonderful group of people I have had the opportunity to work with. I would like to thank all of the many professors who have been so willing to share their knowledge with me. I would also like to acknowledge my fellow students in ISSL and SMSL. They have

helped me overcome issues with my project, worked through homework assignments with me, discussed everything from courtship customs around the world to Startcraft strategies; I look forward to continued work with them all in our futures.

Research does not take place in a vacuum and my work would never have been possible without the moral and emotional support of people from the rest of my life. My parents Barb and LeVern and my brothers Galen and Eric deserve credit for creating the foundation on which my abilities are based and for continuing to edge me on throughout the process. My friends, Ben, Kriss, Dave, Jen, Frank, Jon, Ryan, and many others supported me, encouraged me, laughed with me, relaxed with me, fed me, distracted me, and most of all cared for me. They made my experience here one I will remember fondly and are in large part responsible for my success. My fellow Chapelites at Buckeye Lutheran Campus Ministry and IMOKers through Lutheran Student Movement deserve thanks for providing me with a family in Ohio who, whether they knew it or not, were always there for me. Last but certainly not least, I would like to express my heartfelt appreciation to my boyfriend, Wil, who in the past 2 months has given me so much encouragement, support, guidance, patience, love, and hope for the future.

## VITA

April 11, 1976 .....	Born - Rome, Italy
May 1994 .....	High School Diploma, American Overseas School of Rome, Italy
May 1999 .....	B.S. Engineering Science, Iowa State University
December 1999 .....	B.S. Physics, Iowa State University
August 2001 .....	M.S. Engineering Mechanics, Iowa State University
August 2005 .....	M.S. Mechanical Engineering, The Ohio State University
2001-present .....	Graduate Fellow, The Ohio State University

## PUBLICATIONS

### Refereed Publications

L.E. Faidley, M.J. Dapino, G.N. Washington, “Homogenized Strain Model for Ni-Mn-Ga Driven with Collinear Field and Stress”. *Journal of Intelligent Materials Structures and Systems*, under review.

L.E. Faidley, M.J. Dapino, G.N. Washington, T.A. Lograsso, “Modulus Shift with Magnetic Field in Ferromagnetic Shape Memory Ni-Mn-Ga”. *Journal of Intelligent Materials Structures and Systems*, Vol. 17(2), pp. 123-131, Feb. 2006.

L.E. Faidley, M.J. Dapino, G.N. Washington, “Strain Model for Ni-Mn-Ga with Collinear Field and Stress”. *Proceedings of IMECE 2005*, Paper #79092, Nov 2005.



L.E. Faidley, M.J. Dapino, G.N. Washington, T.A. Lograsso, R.C. Smith, “Dynamic Response in the DC-20kHz Range and Delta-E Effect in Ferromagnetic Shape Memory Ni-Mn-Ga”. *Proceedings of IMECE 2003*, Paper #43198, Nov 2003.

### **Proceedings Publications**

L.E. Faidley, M.J. Dapino, G.N. Washington, “A homogenized strain model for Ni-Mn-Ga driven with collinear field and stress. *Proceedings of SPIE Smart Structures and Materials*, No. 6170-46, in publication.

L.E. Faidley, M.J. Dapino, G.N. Washington, T.A. Lograsso, “Reversible Strain in Ni-Mn-Ga with Collinear Field and Stress”. *Proceedings of SPIE Smart Structures and Materials*, Vol. 5761, p. 501-512, March 2005.

L.E. Faidley, M.J. Dapino, G.N. Washington, T.A. Lograsso, “Dynamic Behavior and Stiffness Tuning in Solenoid Based Ni-Mn-Ga Transducers”. *Proceedings of SPIE Smart Structures and Materials*, Vol. 5387, p. 519-527, March 2004.

L.E. Faidley, M.J. Dapino, G.N. Washington, T.A. Lograsso, R.C. Smith, “Analytical and Experimental Issues in Ni-Mn-Ga Transducers”. *Proceedings of SPIE Smart Structures and Materials*, Vol. 5049, p. 1-12, March 2003.

L.E. Faidley, M.J. Dapino, A.B. Flatau, “Characterization of a Small Terfenol-D Transducer in Mechanically Blocked Configuration”. *Proceedings of SPIE Smart Structures and Materials*, Vol. 4327, p. 521-532, March 2001.

L.E. Faidley, B.J. Lund, A.B. Flatau, F.T. Calkins “Terfenol-D Elasto-Magnetic Properties Under Varied Operating Conditions Using Hysteresis Loop Analysis”. *Proceedings of SPIE Smart Structures and Materials*, Vol. 3329, p. 856-865, March 1998.

## **FIELDS OF STUDY**

Major Field: Mechanical Engineering

Studies in Smart Materials: Characterization & Modeling: Prof. Dapino, Prof. Washington

# TABLE OF CONTENTS

	Page
Abstract . . . . .	ii
Dedication . . . . .	iv
Acknowledgments . . . . .	v
Vita . . . . .	vii
List of Tables . . . . .	xii
List of Figures . . . . .	xiii
Chapters:	
1. Introduction . . . . .	1
1.1 Introduction and Motivation . . . . .	1
1.2 Organization of this Dissertation . . . . .	5
2. Background Information . . . . .	7
2.1 Review of Smart Materials . . . . .	7
2.1.1 Magnetostrictive Materials . . . . .	9
2.1.2 Shape Memory Alloys . . . . .	10
2.2 Ferromagnetic Shape Memory Alloys . . . . .	12
2.2.1 Properties . . . . .	12
2.2.2 Active Mechanism . . . . .	15
2.2.3 Modeling . . . . .	19
2.3 Contribution to the Field: Collinear Stress-Field Configuration . .	21

3.	Characterization of Ni-Mn-Ga in Collinear Stress-Field Configuration . . .	23
3.1	Discussion of the Collinear Stress-Field Configuration . . . . .	23
3.2	Solenoid Transducer Design . . . . .	24
3.2.1	Magnetic Circuit . . . . .	25
3.2.2	Water Cooled Driving Coil . . . . .	28
3.2.3	Sensing Elements . . . . .	29
3.2.4	Transducer Modifications . . . . .	31
3.3	Review of Previous Quasi-Static Testing of $\text{Ni}_{50}\text{Mn}_{28.7}\text{Ga}_{21.3}$ . . . .	32
3.3.1	Sample Manufacture . . . . .	33
3.3.2	Strain Measurements . . . . .	34
3.3.3	Magnetization Testing . . . . .	36
3.4	Dynamic Testing: Investigation of Modulus Shifts . . . . .	36
3.4.1	Magnetic Excitation . . . . .	38
3.4.2	Mechanical Excitation . . . . .	42
3.4.3	Discussion of Results . . . . .	45
3.5	Concluding Remarks . . . . .	49
4.	Modeling of the Ferromagnetic Shape Memory Effect . . . . .	50
4.1	Parallel Configuration Strain Mechanism . . . . .	51
4.2	Gibbs Free Energy Formulation . . . . .	52
4.3	Complementary Driving Force . . . . .	57
4.4	Volume Fraction Model Development . . . . .	59
4.5	Hysteresis Kernel Model . . . . .	60
4.6	Stochastic Homogenization . . . . .	66
4.6.1	Stochastic Homogenization Method for Magnetostrictive Ma- terials . . . . .	67
4.6.2	Stochastic Homogenization Method Applied to Ni-Mn-Ga in the Collinear Stress-Field Configuration . . . . .	70
4.7	Model Implementation . . . . .	73
4.7.1	Coding . . . . .	73
4.7.2	Parameter Determination . . . . .	75
4.7.3	Distribution Truncation . . . . .	76
4.8	Model Results and Error Analysis . . . . .	80
4.9	Concluding Remarks . . . . .	85
5.	Conclusions . . . . .	86
5.1	Contributions to the Field . . . . .	86
5.2	Summary of Findings . . . . .	88

5.3	Future Work . . . . .	89
Appendices:		
A.	Transducer Machine Drawings . . . . .	91
	A.1 Transducer Design . . . . .	92
	A.2 Modified Transducer Design . . . . .	102
B.	Model Code . . . . .	114
	B.1 Stochastic Homogenization Code . . . . .	114
	B.2 Parameter Identification Code . . . . .	120
	B.3 Kernel Model Code . . . . .	125
	Bibliography . . . . .	126

## LIST OF TABLES

Table	Page
2.1 Summary of active material effects. . . . .	8
3.1 Characteristic temperatures for $\text{Ni}_{50}\text{Mn}_{28.7}\text{Ga}_{21.3}$ . . . . .	33
3.2 Magnetic properties for $\text{Ni}_{50}\text{Mn}_{28.7}\text{Ga}_{21.3}$ at 0.1 Hz. . . . .	37
3.3 Summary of results for modulus shift with varying magnetic field. . . . .	49
4.1 Parameters in terms of measured data. . . . .	61
4.2 Model parameters obtained from measurements collected at various stress values. . . . .	63
4.3 Error comparison for various choices of parameter source data. . . . .	65
4.4 Values for model coefficients. . . . .	76
4.5 Error associated with each of the methods used to eliminate the discontinuity at maximum field. . . . .	79
4.6 Constrained optimization results for parameters under various loads. . . . .	81
4.7 Error comparison for parameters determined for various loading conditions. . . . .	84

## LIST OF FIGURES

Figure	Page
1.1 Field and stress in a solenoid. . . . .	3
1.2 Field-stress orientation for conventional and proposed configurations.	4
1.3 Field and stress in an electromagnet. . . . .	5
2.1 Joule magnetostriction produced by a magnetic field $H$ . (a) $H$ is approximately proportional to the current $i$ that passes through the solenoid when a voltage is applied to it, (b) the rotation of magnetic dipoles changes the length of the sample and (c) curve $\Delta L/L$ vs. $H$ obtained by varying the field sinusoidally (inset). [15] . . . . .	10
2.2 Shape memory effect in a uniaxial SMA in which a residual strain $\epsilon_r$ is recovered through heating. [79] . . . . .	11
2.3 (a) Relative orientation of sample, strain gauge, and applied field for measurements shown in (b) and (c). (b) Strain vs applied field in the $L2_1$ [austenite] phase at 283 K. (c) Same as (b) but data taken at 265 K in the martensitic phase. [93] . . . . .	13
2.4 Ni-Mn-Ga crystal structure (a) austenite and (b) martensite [76]. . .	15
2.5 Self-accommodating twin structure developed when austenitic Ni-Mn-Ga cools into the martensitic phase. . . . .	16
2.6 Strain mechanism for Ni-Mn-Ga under an orthogonal field-stress pair. (a) No field applied. (b) - (d) Sample elongation due to increasing field. (e) Sample length remains unchanged when field is removed. (f) Sample contraction due to a compressive stress. . . . .	18

3.1	Solenoid based test transducer. . . . .	25
3.2	Magnetic circuit components for solenoid transducer. . . . .	26
3.3	Components of the central section of the experimental transducer. . .	27
3.4	Coil schematic showing various components of the water cooled driving coil. . . . .	29
3.5	Variation of the magnetic induction at different heights from the bottom of the solenoid for 60V applied voltage. . . . .	30
3.6	Components of the central section of the prestress capable modified transducer. . . . .	32
3.7	Strain vs magnetic field for $\text{Ni}_{50}\text{Mn}_{28.7}\text{Ga}_{21.3}$ at zero load and 0.1 Hz.	35
3.8	Maximum strain from $\text{Ni}_{50}\text{Mn}_{28.7}\text{Ga}_{21.3}$ under various loads at 0.1 Hz.	36
3.9	Strain vs magnetic field for $\text{Ni}_{50}\text{Mn}_{28.7}\text{Ga}_{21.3}$ at zero load and 0.1 Hz.	37
3.10	Research transducer as used for magnetic excitation modulus tests. .	38
3.11	Experimental setup used for dynamic testing of Ni-Mn-Ga. . . . .	39
3.12	Comparison of experimental and 1DOF model results for frequency (f) as a function of load (m). . . . .	41
3.13	Dynamic magnetic excitation of $\text{Ni}_{50}\text{Mn}_{28.7}\text{Ga}_{21.3}$ for various applied bias fields and 60 gram load. . . . .	42
3.14	Dynamic magnetic excitation of $\text{Ni}_{50}\text{Mn}_{28.7}\text{Ga}_{21.3}$ for various applied bias fields and 250 gram load. . . . .	43
3.15	Shaker set-up used for dynamic modulus shift verification. . . . .	44
3.16	Dynamic mechanical excitation of Ni-Mn-Ga for various applied fields and a 50g load. . . . .	45
3.17	Calculated elastic modulus shift and damping trend for various loads.	46

3.18	Loading stress-strain curves for Ni-Mn-Ga under various bias fields [51].	48
4.1	Strain mechanism for Ni-Mn-Ga driven by a collinear stress and field pair in the presence of pinning sites. (a) No field applied. (b) - (d) Sample contraction due to increasing field. (e) Return to original length with the field is removed. . . . .	51
4.2	Two-dimensional variants: notation and orientation. . . . .	53
4.3	Magnetization vs field curve for $\text{Ni}_{50}\text{Mn}_{28.7}\text{Ga}_{21.3}$ . [51] . . . . .	61
4.4	Maximum strain per input axial stress for $\text{Ni}_{50}\text{Mn}_{28.7}\text{Ga}_{21.3}$ . [51] . . .	61
4.5	Data points for parameter identification. . . . .	62
4.6	Predicted strain compared with actual strain for parameters calculated from various data sets. . . . .	64
4.7	Local magnetization $\overline{M}$ given by expression (4.34). [79] . . . . .	69
4.8	Comparison of steel data with model results obtained from Equation (4.33). [79] . . . . .	69
4.9	Distributions for (a) interaction field $H_i$ , (b) pinning site strength $k_2$ . (c) effect of the $k_2$ distribution on the hysteresis kernels. . . . .	72
4.10	Comparison of model results and experimental data for the $\sigma = -0.0125$ MPa loading condition using various implementation methods: (a) using full distribution, (b) using method (i), (c) using method (ii), and (d) using method (iii). . . . .	77
4.11	Hysteresis kernels produced by relation (4.29) showing both physical and non-physical behaviors. . . . .	78
4.12	Truncated distributions for (a) pinning site strength $k_2$ and (b) interaction field $H_i$ . . . . .	80
4.13	Constrained optimization fits to data for various loads: (a) $\sigma_y = -0.0125$ MPa, (b) $\sigma_y = -0.13$ MPa, (c) $\sigma_y = -0.27$ MPa, (d) $\sigma_y = -0.41$ MPa. . . . .	82



4.14 Overall optimized simulation of strain compared to data for various loads: (a) $\sigma_y = -0.0125$ MPa, (b) $\sigma_y = -0.13$ MPa, (c) $\sigma_y = -0.27$ MPa, (d) $\sigma_y = -0.41$ MPa. . . . .	83
A.1 Cross-section of transducer assembly showing all relevant parts. . . .	92
A.2 Bottom plate made from AISI 1018 magnetic steel. . . . .	93
A.3 Magnetic base made from AISI 1018 magnetic steel. . . . .	94
A.4 Bottom cap of sample housing made from AISI 1144 stress proof magnetic steel. . . . .	95
A.5 Sample housing made from AISI 303 stainless (non-magnetic) steel. .	96
A.6 Pick-up coil spool made of Aluminum 6061-T6. . . . .	97
A.7 Push rod made of AISI 1144 stress proof magnetic steel. . . . .	98
A.8 LVDT platform made of AISI 303 stainless (non-magnetic) steel. . . .	99
A.9 Top plate made from AISI 1018 magnetic steel. . . . .	100
A.10 Outer casing made from AISI 1018 magnetic steel pipe. . . . .	101
A.11 Cross-section of modified transducer assembly showing all relevant parts.	102
A.12 Base of modified transducer made of AISI 1018 magnetic steel. . . . .	103
A.13 Bottom cap of sample casing for modified transducer made of AISI 1018 magnetic steel. . . . .	104
A.14 Outer shell of sample casing for modified transducer made of AISI 1144 non-magnetic steel. . . . .	105
A.15 Upper cap of sample casing for modified transducer which acts as the prestress bolt made of AISI 1018 magnetic steel. . . . .	106
A.16 Pick-up coil spool for modified transducer made of Aluminum 6061-T6.	107
A.17 Push rod for modified transducer made of AISI 1018 magnetic steel. .	108

A.18 Bearing brace for modified transducer made of AISI 1018 magnetic steel.	109
A.19 Top plate for modified transducer made of AISI 1018 magnetic steel. .	110
A.20 Bottom plate for modified transducer made of AISI 1018 magnetic steel.	111
A.21 Outer casing for modified transducer made from AISI 1018 magnetic steel pipe. . . . .	112
A.22 Cooling sleeve for modified transducer made of copper piping. . . . .	113

# CHAPTER 1

## INTRODUCTION

### 1.1 Introduction and Motivation

Large strains and magnetic activation make nickel-manganese-gallium (Ni-Mn-Ga) and other Ferromagnetic Shape Memory Alloys (FSMAs) extremely attractive as actuator elements since materials exhibiting both large displacements and fast response times have been rare. These qualities make FSMAs promising for applications such as underwater communications, structural morphing of unmanned aerial vehicles, and tunable stiffness resonators for noise and vibration control applications. Many of these applications require FSMA devices of compact size, high energy density, broad frequency response, and few moving parts which are most easily achievable by solenoid based actuators. However, results in the literature focus primarily on actuators driven by an electromagnet with the stress axis oriented orthogonal to the magnetic field axis, as this configuration allows for reversible strains. This work experimentally and analytically investigates the response of Ni-Mn-Ga to the collinear field-stress pair encountered in solenoid based transducers. Driving the material with a collinear field and stress is unusual since current martensite reorientation theories do not support the existence of reversible deformations in this configuration. If strains

were achievable, the benefit of this approach would lie in the ability to drive the material with a solenoid transducer that offers enhanced bandwidth and energy density relative to standard electromagnet drives. Solenoid transducers such as the one shown in Figure 1.1 involve smaller volume and weight than electromagnet transducers and also reduce demagnetization effects and eddy current losses. In order to establish the response of Ni-Mn-Ga in the collinear configuration, dynamic tests have been performed to extend the work done by Malla et al. [53, 52] on quasi-static material characterization in this configuration to the dynamic regime. This knowledge will prove valuable in the development of a more thorough understanding of the physical strain mechanisms occurring in this material. A related goal of this research is the derivation of an analytical model that will make use of theoretical understanding and experimental data on the strain behavior of Ni-Mn-Ga. The specific outcome of the modeling effort is to accurately simulate the strain for a specified magnetic field and mechanical loading conditions.

Ferromagnetic shape memory Ni-Mn-Ga is attractive for transducer applications because it has exhibited strains of 6% [43, 60] to 9.5% [84] when exposed to magnetic fields as low as 400 kA/m. Such strains are on the order of those possible from shape memory alloys (SMAs), but because they are generated in response to magnetic fields a higher frequency bandwidth is possible [20]. As is the case with shape memory materials, the large deformations exhibited by Ni-Mn-Ga alloys originate in the pseudo-elasticity associated with the reorientation of martensitic twin variants. Unlike nickel titanium and other shape memory materials, in which the ability to do work stems from thermomechanical transformation between the martensite and austenite phases, the main actuation mechanism in Ni-Mn-Ga takes place in the low

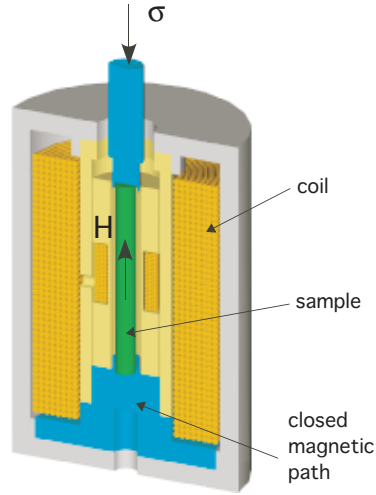


Figure 1.1: Field and stress in a solenoid.

temperature martensite phase and is driven by magnetic fields or mechanical stresses. Because Ni-Mn-Ga lacks the restoring mechanism that the phase transformation in SMAs provides, a force needs to be applied orthogonal to the applied field to restore the original orientation of the twin variants creating reversible strains.

The top panel of Figure 1.2 outlines the strain mechanism for the configuration in which the field is applied orthogonal to the sample's axis along which a mechanical load is applied. Because this is the configuration employed in traditional electromagnet devices as that shown in Figure 1.3, it is denoted “conventional configuration.” The stress serves to precondition the material into a single variant state allowing for maximum strain output. When a field is applied orthogonal to the sample's axis a

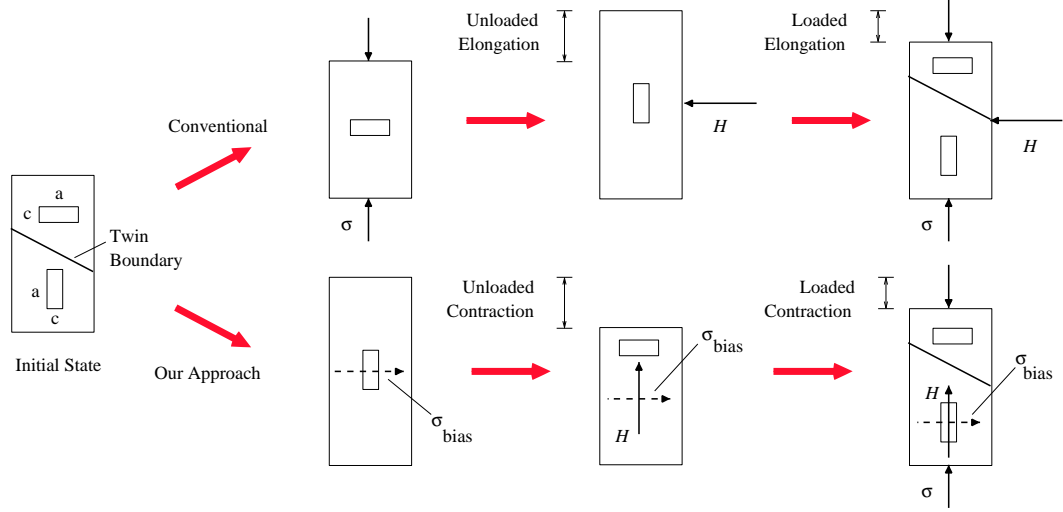


Figure 1.2: Field-stress orientation for conventional and proposed configurations.

bulk elongation of up to 6-9.5% is achieved. Then the sample is restored to its original size through the application of a mechanical stress along the axis of the sample.

The bottom panel of Figure 1.2 illustrates the substantially different strain mechanism that is proposed to describe the reversible strains of -0.41% measured from a  $\text{Ni}_{50}\text{Mn}_{28.7}\text{Ga}_{21.3}$  sample [53] when the input field and stress are collinear along the axis of the rod. In this configuration the applied field and stress favor the same variant and therefore reversible strains are not predicted by conventional variant reorientation models. The unexpected result suggests the presence of pinning sites or residual stresses in the alloy. They act as localized energy potentials opposing twin boundary motion and providing an otherwise nonexistent restoring force when the magnetic field is removed. The existence of unexpected reversible strains in this collinear configuration points to a current lack of understanding of (a) the capabilities of Ni-Mn-Ga in the collinear configuration, (b) the physical mechanisms governing twin boundary

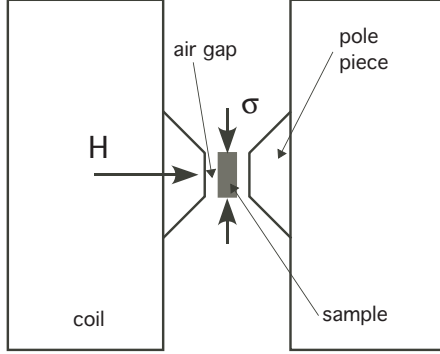


Figure 1.3: Field and stress in an electromagnet.

motion in non-ideal Ni-Mn-Ga alloys featuring pinning sites, and (c) the necessary mathematical models for this material. All of these issues will be addressed in this dissertation as outlined in the following section.

## 1.2 Organization of this Dissertation

Chapter 2 further motivates the need for this work by describing the key aspects of the body of existing literature on Ni-Mn-Ga used in both the conventional and collinear stress-field configurations. Focus is placed on the historical discovery of the physical capabilities of Ni-Mn-Ga and the shift in emphasis towards the conventional configuration because of its large strain capabilities. The generally accepted strain mechanism for Ni-Mn-Ga is described such that the true relevance of the surprising reversible strain with no external stress described in Chapter 3 can be better understood. This strain mechanism also forms a basis for the proposal of a modified strain mechanism that is presented in Chapter 4. Finally, Chapter 2 presents an overview of

modeling techniques that have been applied to Ni-Mn-Ga in order to form the ground work for the modeling work in Chapter 4.

Chapter 3 provides an in depth characterization of the physical capabilities of  $\text{Ni}_{50}\text{Mn}_{28.7}\text{Ga}_{21.3}$  when activated by a collinear field and stress along the sample axis. A review of the quasi-static strain and magnetization measurements presented by Malla et al. [52] provides the experimental backdrop for a discussion of the importance of extending the study of Ni-Mn-Ga into the collinear arena and motivate the continued experimental investigation into other characteristic behavior. The quasi-static data is augmented through this work into the dynamic regime through a series of swept sine tests at various bias magnetic fields and loads. Of particular interest is the investigation of the effect of bias magnetic field and mechanical load on the resonance behavior of the material indicating a dependence of the elastic modulus of the sample on the applied magnetic field.

Chapter 4 describes the proposed modifications of the accepted strain mechanism presented in Chapter 2 that explain the occurrence of reversible strain with no externally applied restoring force. A mechanism is explained which incorporates the effects of pinning sites and residual stresses that impede the motion of twin boundaries through the material providing the necessary restoring force and limiting the strain output. The proposed strain mechanism is then described through an energy functional that results in an idealized hysteresis model for the strain behavior of Ni-Mn-Ga. The development and implementation of a stochastic homogenization method is then discussed leading to an accurate numerically generated simulation of the strain from the  $\text{Ni}_{50}\text{Mn}_{28.7}\text{Ga}_{21.3}$  sample under various loading conditions.



## CHAPTER 2

### BACKGROUND INFORMATION

#### 2.1 Review of Smart Materials

An *active* or *smart* material is defined as a material that undergoes a substantial change in one or more properties in response to a change in external conditions [2]. Such materials are categorized according to the type of response and type of activation; a summary is shown in Table 2.1. All of these materials are transducer materials as they transform one form of energy into another. In addition, most of them are capable of direct and inverse effects leading to applications as both actuators and sensors.

Piezoelectric materials are the most commonly used smart materials. This category of materials produces strains of up to 0.1% (PZT) and 0.07% (PVDF) when exposed to an electric field [95] and also produces a voltage when the material is strained. They have found numerous applications as both actuators and sensors. Piezoelectric devices are also known for their high frequency capability; this technology is often used in ultrasonic applications [40]. Microscopically, piezoelectric materials are characterized by having an off-center charged ion in a tetragonal unit

Input	Property Change					
	Electric	Magnetic	Mechanical	Fluid	Thermal	Optical
Electric			Piezo-electric, Electro-strictive	Electro-rheological	Electro-caloric	Electro-chromic
Magnetic			Magneto-strictive, FSMA	Magneto-rheological	Magneto-caloric	
Mechanical	Piezo-electric, Electro-strictive	Magneto-strictive, FSMA	Compliance	Visco-elastic		Tribochromic
Thermal	Pyro-electric		SMA's			Thermo-chromic
Light	Photo-voltaic					Photochromic

Table 2.1: Summary of active material effects.

cell which can be moved from one axis to another through the application of an electric field or stress [79]. As the ion changes position it causes strain in the material. In order for bulk strain to occur, these materials are generally polarized. Typical piezoelectric materials, PZT and PVDF, are generally employed in stacks, where the strain amplitude is amplified by placing many devices in series and in bimorphs and THUNDER actuators where the strain is amplified through the elastic structure to which the active material is attached. Electrostrictive materials are similar to piezoelectrics but generally have increased strain, are more nonlinear, require higher fields, and have more stringent temperature requirements [57].

Magneto- and electro-rheological fluids are oil or water based liquids that change their viscosity, yield stress, and other rheological properties due to the application of a magnetic or electric field. Micro- or nano- sized particles are suspended in the base fluid and align with the applied field impeding the flow. These fluids have found applications in smart dampers [31], high frequency valves [65], force feedback devices [1], and automotive clutches [64].

Ferromagnetic shape memory alloys, which are the focus of this dissertation, are most closely related to magnetostrictive materials and to standard shape memory alloys. Hence, a more thorough examination of the active mechanism in these two types of active materials is provided in the following sections.

### **2.1.1 Magnetostrictive Materials**

Magnetostrictive materials are similar to Ferromagnetic Shape Memory Alloys (FSMAs) in that they both strain when exposed to a magnetic field and both produce a change in magnetization when a stress is applied. However, the mechanism for these phenomena are distinctly different for the two materials. Giant-magnetostrictive materials like Terfenol-D and Galfenol have strong spin-orbit coupling. Thus, when an applied magnetic field rotates the spins, the orbital moments rotate and considerable distortion of the crystal lattice occurs resulting in large macroscopic strains [15]. A diagram of this strain mechanism is shown in Figure 2.1. Since the magnetostriction of Terfenol-D is dependent on the magnetization vectors turning away from their preferred direction, it can be said that magnetostriction depends on a relatively low value of magnetic anisotropy whereas the opposite is a requirement for ferromagnetic shape memory alloys.

Terfenol-D achieves maximum strains of 0.12% [14] and exhibits interesting high frequency behavior at frequencies up to 10 kHz [23] including a Delta-E effect [36] similar to that discussed for Ni-Mn-Ga in Chapter 3. Some of the disadvantages of Terfenol-D are that it is relatively expensive to produce and is highly brittle. A similar material, Galfenol, which is easier to produce and has higher strength is gaining in popularity. Galfenol can produce 0.03% strain [35] and is machinable with common

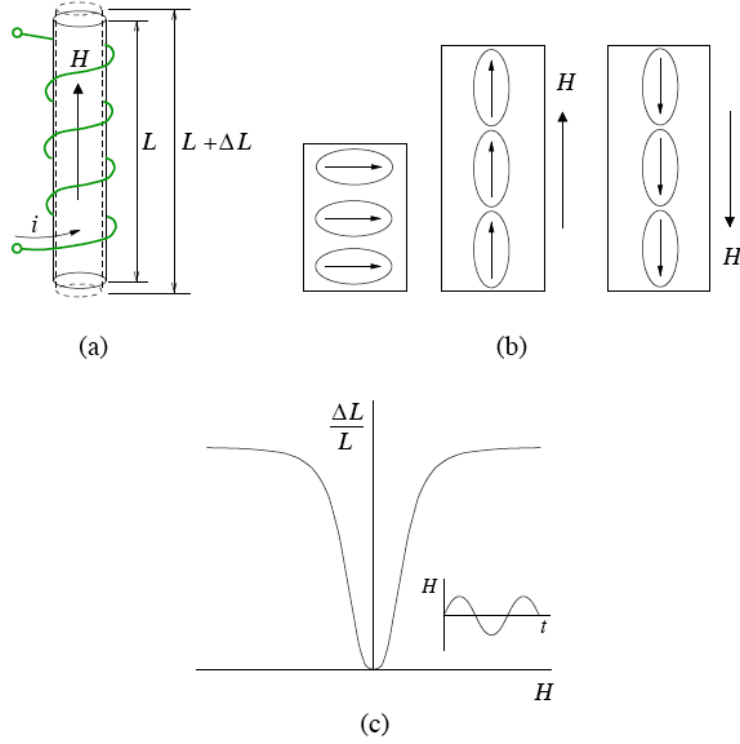


Figure 2.1: Joule magnetostriction produced by a magnetic field  $H$ . (a)  $H$  is approximately proportional to the current  $i$  that passes through the solenoid when a voltage is applied to it, (b) the rotation of magnetic dipoles changes the length of the sample and (c) curve  $\Delta L/L$  vs.  $H$  obtained by varying the field sinusoidally (inset). [15]

techniques [11]. Both of these materials are commonly employed in solenoid based actuators similar to those used in this dissertation for the testing of Ni-Mn-Ga. They have found applications as actuators and sensors in a broad range of fields including industry, bio-medicine, and defense [15].

### 2.1.2 Shape Memory Alloys

Though Shape Memory Alloys (SMAs) are not magnetically activated, the strain mechanism is similar to that found in FSMAs. Thus, an in depth review of these

materials will be useful in understanding the behavior of Ni-Mn-Ga. The most common SMA is NiTiNol, which has been studied since 1962 [6]. A typical strain cycle for an SMA is shown in Figure 2.2. The sample is preset by heating to its high temperature, cubic, austenitic phase. Upon cooling to its tetragonal, martensitic phase the sample's shape remains the same since a self-accommodated twin structure is created. Because of the twin structure, the low temperature phase of NiTiNOL is very soft [96] accommodating a large 8% psuedo-elastic strain when loaded. This strain is completely recoverable by heating the sample back into its austenitic phase in which it returns to its original shape. This transition also the NiTiNol sample to apply large forces to an attached load.

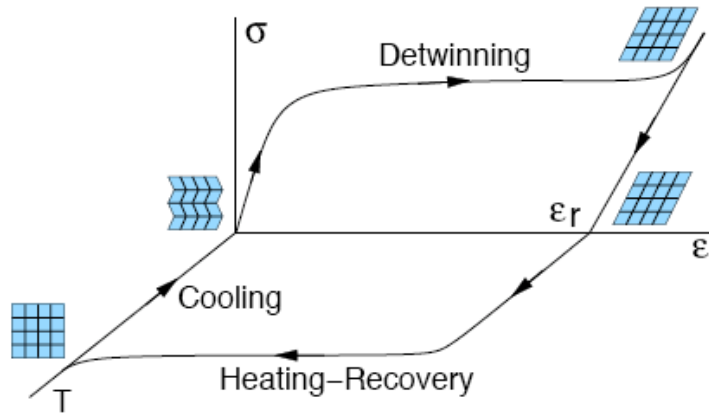


Figure 2.2: Shape memory effect in a uniaxial SMA in which a residual strain  $\epsilon_r$  is recovered through heating. [79]

In addition to the large 8% strains, mechanical stresses have been shown to control the transition temperatures for many compositions of NiTiNOL. Heat and stress

cycles can be applied during the sample’s manufacturing process that augment the strain output and can create samples which have “memorized” a specific complex shape [85]. These possibilities combined with high work output from the sample has enabled SMAs to find applications in many areas including bio-medicine [18], orthodontics [22], aerospace [55], and many others.

## **2.2 Ferromagnetic Shape Memory Alloys**

Ferromagnetic Shape Memory Alloys (FSMAs), which are also called Magnetic Shape Memory Alloys (MSM-Alloys), were first identified by Ullakko at MIT in 1996 [92]. This class of materials, which strain when exposed to a magnetic field, show promise of relatively high strain and high frequency capabilities [92]; they have been the subject of much research over the past 10 years. This section will provide an overview of the work being done by the key contributors to the field and will motivate the importance of the investigations performed for this dissertation.

### **2.2.1 Properties**

The theoretical possibility of materials with a shape memory effect controllable by a magnetic field was first proposed in a series of papers by Ullakko between 1995 and 1996 [89, 90, 91] and by James in 1996 [27]. The first documented experimental results in this area were for the magnetically controlled transformation between austenite and martensite in Fe-Ni at cryogenic temperatures [92]. The first documentation of magnetically controlled twin boundary reorientation, which is of primary interest in the literature today, was also reported in 1996 by Ullakko et al. [93]. The experimental results for unstressed crystals of  $\text{Ni}_2\text{MnGa}$  at 77 K showed strains of 0.2% under a 8 kOe magnetic field. This original data is reproduced in Figure 2.3.

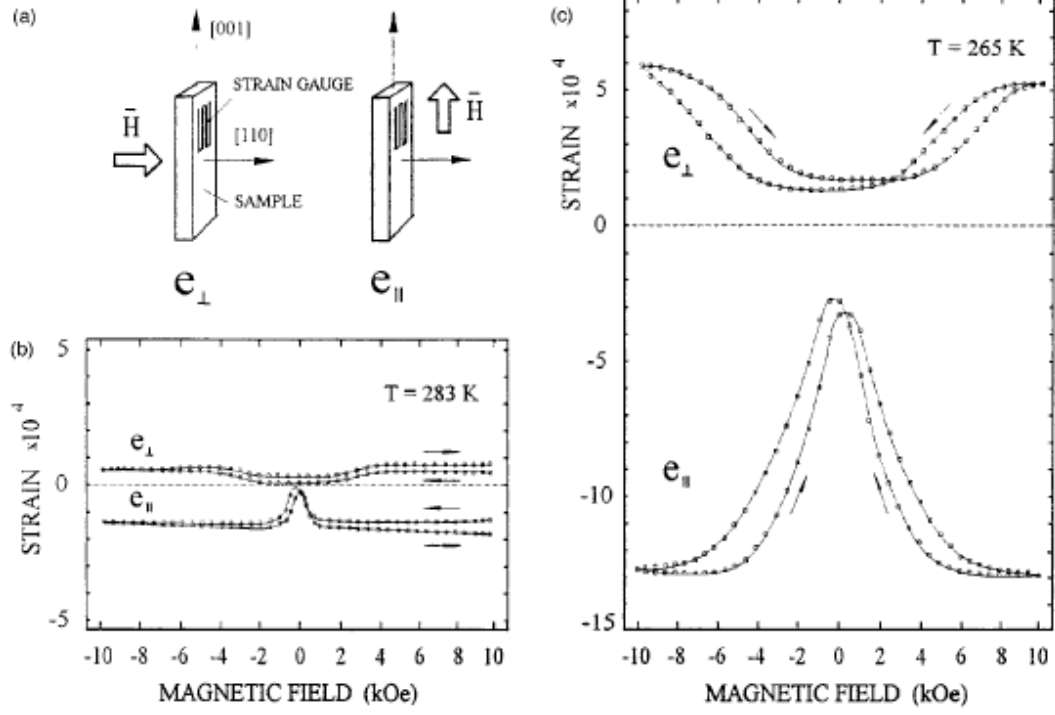


Figure 2.3: (a) Relative orientation of sample, strain gauge, and applied field for measurements shown in (b) and (c). (b) Strain vs applied field in the  $L2_1$  [austenite] phase at 283 K. (c) Same as (b) but data taken at 265 K in the martensitic phase. [93]

Experimental advancement continued with testing of off-stoichiometric Ni-Mn-Ga that demonstrated larger strains at higher temperatures. Tickle et al. studied  $\text{Ni}_{51.3}\text{Mn}_{24.0}\text{Ga}_{24.7}$  at  $-15^\circ\text{C}$  exposed to fields of less than 10 kOe [87]. They observed strains of 0.2% due to cyclic application of an axial magnetic field and strains of 1.3% when fields were applied transverse to the sample that started from a stress biased state. This finding shifted the focus of Ni-Mn-Ga research towards the orthogonal stress-field orientation and left a gap in the understanding of the collinear stress-field configuration that this dissertation seeks to fill.

Work continued on examining compositions and treatments of Ni-Mn-Ga to optimize for large room temperature strains [59] culminating in the empirical mapping of the useful compositional ranges presented by Jin et al. [30]. Based on experimental results from various sources, Jin et al. identified a range between  $\text{Ni}_{52.5}\text{Mn}_{24.0}\text{Ga}_{23.5}$  and  $\text{Ni}_{49.4}\text{Mn}_{29.2}\text{Ga}_{21.4}$  in which the martensitic transformation temperature,  $T_m$ , is higher than room temperature and lower than the Curie temperature,  $T_C$ , and the saturation magnetization is larger than 60 emu/g. These conditions are suggested by Jin as characterizing samples with the best capability for large, room temperature strains.

The literature reports maximum strains for 6% for Ni-Mn-Ga samples with tetragonal martensite structure with a five-layer shuffle-type modulation [67, 61, 43] that is the theoretical maximum for this geometry. A second microstructure sometimes found in Ni-Mn-Ga has orthorhombic martensitic phase with a seven-layered modulation and has been found to exhibit strains of 9.5% [84]. Other techniques have also been investigated with the goal of augmenting the strain output from Ni-Mn-Ga including thermal treatments [66], texturing [72], external application of stress [43], use of polycrystalline samples [73], and variation of operating temperature and sample composition [24, 41, 30]

Though alloys in the Ni-Mn-Ga system have shown the most promise as Ferromagnetic Shape Memory Alloys, other alloys are also being investigated. James and Wuttig measured strains of 0.5% in  $\text{Fe}_{70}\text{Pd}_{30}$  [26] which has also been investigated by Kato et al. [33, 42, 94, 34] and James et al. [28] among others. Work has also been done with alloys in the Ni-Fe-Ga system [58], the Ni-Mn-Fe-Ga system [77], and with Fe-Pt [32], Co-Ni-Al [71, 70], and Co-Ni-Ga, [71, 97] .



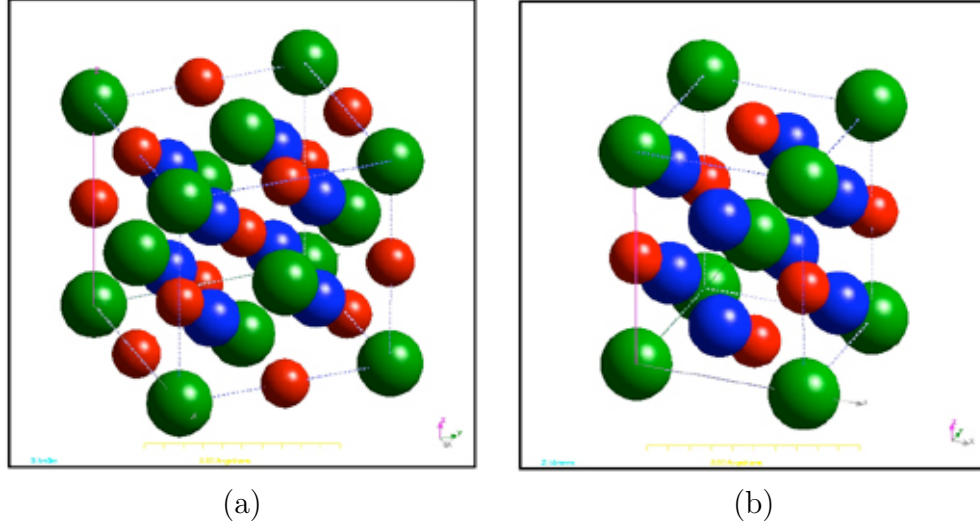


Figure 2.4: Ni-Mn-Ga crystal structure (a) austenite and (b) martensite [76].

### 2.2.2 Active Mechanism

In order to establish a firm understanding of the properties and behavior of Ni-Mn-Ga and other FSMA, it is necessary to understand the physical mechanisms behind this behavior. These mechanisms and the crystallography and micro-structure on which they are based will be described in this section.

In the high temperature austenitic phase Ni-Mn-Ga has a cubic Heusler ( $L_{21}$ ,  $Fm\bar{3}m$ ) structure with the Ga and Mn atoms forming interlocking face-centered cubic lattices offset by half a lattice parameter, and the Ni atoms forming a cubic lattice with atoms at the corners, edge centers, and body center that is offset by  $[\frac{1}{2}, \frac{1}{2}, \frac{1}{2}]$  as is shown in Figure 2.4(a) [76]. As it cools, the material undergoes a phase change to a martensitic, tetragonal ( $I4/mmm$ ) structure as shown in Figure 2.4(b). The unique  $c$ -axis of the tetragonal unit cell is shorter than the  $a$ -axis with a ratio of 1.33 [62].

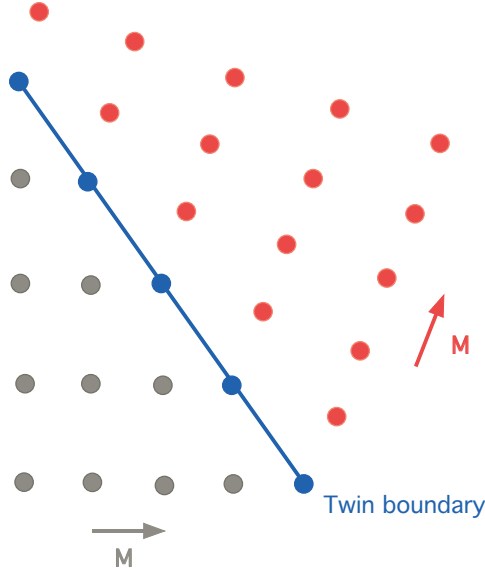


Figure 2.5: Self-accommodating twin structure developed when austenitic Ni-Mn-Ga cools into the martensitic phase.

Key to the activity of Ni-Mn-Ga is the fact that in the transformation between austenite and martensite a self accommodating twin structure is created [44]. This structure, which is shown in Figure 2.5, is caused by the minimization of the internal strain energy generated from the mismatch between the cubic and tetragonal lattices; it is similar to the structure that arises in temperature driven SMAs. Because of the tetragonal nature of the martensitic phase, three twin orientations are possible of which two are identical relative to the axis of the sample [46]. The variants with their c-axis aligned with the sample axis are referred to as the axial variants while those with one of their a-axes aligned with the sample's axis are the transverse variants.

In order for materials to be active as Ferromagnetic Shape Memory Alloys they need to have a large magnetic anisotropy [63]. This property, which differentiates

them from magnetostrictives, assures that the magnetization vector for each unit cell is strongly fixed to the c-axis. The magnetic anisotropy energy for the tetragonal martensite is given by [67]

$$U_a = K_{u0} + K_{u1} \sin^2 \theta + K_{u2} \sin^4 \theta + \dots \quad (2.1)$$

where  $\theta$  is the angle between the unique axis of the crystal and the magnetization vector and  $K_{ui}$  are experimentally determined coefficients. If this energy is large enough, the alignment of magnetization vectors with an applied field will change the physical orientation of the unit cells creating strain from the material. This phenomenon, which is of primary importance to the strain mechanism in FSMAs, is described in more detail in Figure 2.6.

At zero field the material consists of two orthogonal variants, described by the volume fraction  $x$ , that are separated by a twin boundary (panel (a)). Each variant consists of several distinct magnetic domains divided by  $180^\circ$  walls. The magnetic domain volume fraction is denoted  $a$ . At small transverse fields,  $H$ , on the order of  $\sim 8$  kA/m the magnetic domains consolidate to a single domain per twin variant (panel (b)). Since we are interested in the behaviors at medium to large fields,  $a = 1$  is assumed.

As a transverse field is applied, the variants favored by the field will increase in size through twin reorientation. Alloys in the Ni-Mn-Ga system have large magnetic anisotropy energies compared to the energy necessary to reorient the unit cells at the twin boundary. Thus, as the applied magnetic field attracts the unit cell magnetization vectors towards it, the unit cells along the twin boundary will switch orientation such that their c-axis is more closely aligned with the field. This results in the growth

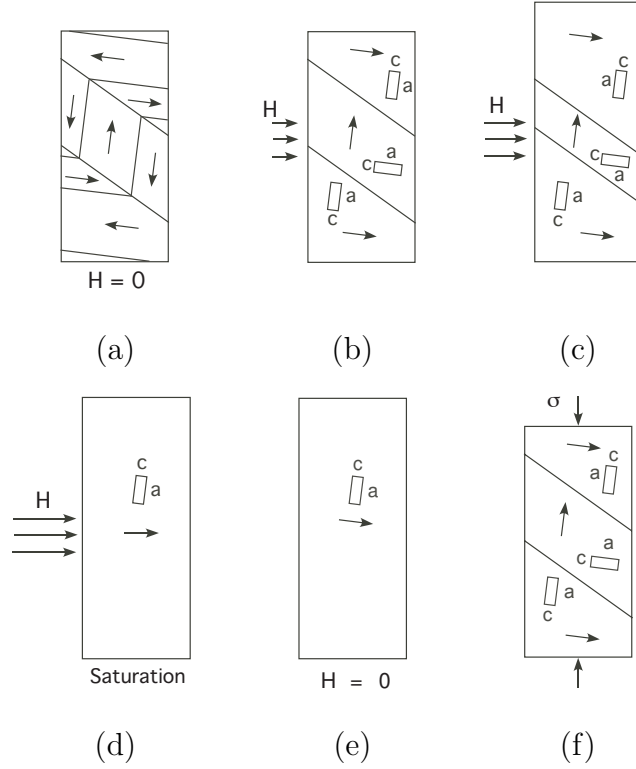


Figure 2.6: Strain mechanism for Ni-Mn-Ga under an orthogonal field-stress pair. (a) No field applied. (b) - (d) Sample elongation due to increasing field. (e) Sample length remains unchanged when field is removed. (f) Sample contraction due to a compressive stress.

of favorable variants at the expense of unfavorable ones through twin boundary motion resulting in the overall axial lengthening of the bulk sample(panel (c)). As the field is increased to the point where no further twin boundary motion is possible and the field energy overcomes the magnetic anisotropy energy, the local magnetization vectors break away from the c-axis and aligns with the field. This results in magnetic saturation as shown in panel (d). When the field is removed (panel (e)) the magnetic anisotropy energy will restore the local magnetization to the c-axis of the unit cells.

Since both variants are equally favorable from an energy standpoint [60], there is no restoring force to drive the unit cell reorientation and the size of the sample will not change upon removal of the field. Twin boundary motion and reversible strain can be induced by applying an axial field, axial compressive stress, or a transverse tensile stress, all of which favor the variant with the short c-axis aligned with the axial direction as shown in panel (f). One common configuration for Ni-Mn-Ga consists of placing a rectangular sample in an electromagnet such that the field is applied transversely and a bias axial compressive stress is always present [88] as depicted in Figure 1.3.

### 2.2.3 Modeling

Having now described the physical strain mechanism postulated to occur in Ni-Mn-Ga it is possible to discuss in more detail the development of various mathematical models for FSMA.

In 1998 James and Wuttig proposed a modeling technique for general ferromagnetic shape memory alloys based on a “constrained theory of magnetostriction” [28]. This theory addresses the challenge of describing the behavior of FSMA from a micro-mechanical approach. Using the conventional expression of the micro-mechanical energy they incorporate the magnetic anisotropy energy, the magnetostatic energy, the elastic energy, the Zeeman energy, and the stress energy, developing an energy landscape that incorporates various energy wells. They use this model to develop criteria to predict whether a given material will be an effective FSMA. Because of the complexity of this model it has only been implemented for specific, highly simplified cases [28, 26, 86].

Early in the study of Ni-Mn-Ga, Likhachev and Ullakko proposed one of the models that has become the basis for much of the subsequent modeling work [44, 46, 45, 48, 47]. This model derives an expression for the driving magnetic and mechanical forces based on energy considerations and then equates them based on universality rules. Thus, the strain output for a given magnetic field input can be predicted through an analytic interpolation of mechanical stress-strain experimental data by replacing the mechanical stress with an effective force due to the field.

Another early model that has been fundamental in recent modeling developments was proposed in 1998 by O’Handley et al. [68, 69]. This model presents the difference in Zeeman energies across the twin boundaries as the driving force for twin rearrangement in those situations in which the anisotropy energy is much larger than the Zeeman energy. For those situations in which the anisotropy energy is small the field aligns the magnetization vectors without rotating the unit cells; the driving energy is the anisotropy energy difference across the twin boundary that produces very little strain. For intermediate anisotropy energies the model outlines how both effects take place leading to the saturation behavior of the strain vs. field curves. The free energy is written as a combination of appropriate driving energies and the elastic energy and is then minimized with respect to volume fraction leading to expressions for both strain and magnetization.

Lagoudas and Kiefer also developed a free energy model [39, 38, 37] based on techniques used by Hiersinger and Lexcellent [25] for the modeling of standard SMAs. In their model the energy equation is written as a mixture equation with each variant having distinct mechanical, magnetic, thermal, and chemical energies. In addition,

mixing terms are introduced due to the interaction energies between the two magnetic domains and the two variants. The free energy is minimized with respect to volume fraction and the strain is predicted. Because of the form of the mixing terms, the predicted strain vs field curves incorporate the hysteresis seen experimentally. This model forms the basis for the model developed in this dissertation and will be discussed in more detail in Chapter 4.

The abundance of literature focussed on various modeling techniques for the strain and magnetization of Ni-Mn-Ga and other FSMA's reflects the importance of developing the ability to accurately predict the behavior of these materials for their use in future applications. Other modeling work that merits mention include Bhattacharya and Kohn's [3] work with linear programming, which yields a lower bound to the field induced strain, and Buchel'nikov's model [5] that incorporates elastic, magnetic anisotropy, and Zeeman energies in a description of the growth of both magnetic and structural domains. In addition, L'vov and Chernenko [49, 8, 50] propose a 3 dimension energy expression that incorporates shear and cross terms into the magneto-elastic and mechanical energies.

### **2.3 Contribution to the Field: Collinear Stress-Field Configuration**

The contribution of the work presented in this dissertation lies in the investigation and modeling of Ni-Mn-Ga in a *collinear* stress-field configuration as is shown in Figure 1.1. As is seen in Figure 2.3 the initial experimental testing of Ni-Mn-Ga for magnetically driven strain from twin variant reorientation [89] tested both the collinear and orthogonal configurations and observed that a larger strain was measured for the collinear stress-field tests. However, as variations in composition allowed

Ni-Mn-Ga to be active at room temperature, it was observed that larger strains were achieved for these samples in the direction orthogonal to the applied field and that this configuration allowed for an external orthogonal stress to be applied resulting in reversible strain. Hence, the vast majority of the subsequent literature focussed primarily on the orthogonal configuration, neglecting the collinear orientation.

In previous work done at The Ohio State University, Malla et al. [52, 51, 53] presented results which will be discussed in more detail in Chapter 3 showing that reversible strains of up to -0.41% in the direction of the applied field are achievable from some Ni-Mn-Ga samples even when the applied stress is collinear with the field. As was discussed in Chapter 1 the existence of these unexpected reversible strains in this collinear configuration points to a current lack of understanding of (a) the capabilities of Ni-Mn-Ga in the collinear configuration, (b) the physical mechanisms governing twin boundary motion in non-ideal Ni-Mn-Ga alloys featuring pinning sites, and (c) the necessary mathematical models of this material. The investigation of these points is discussed in the following chapters of this dissertation. As these issues are addressed Ni-Mn-Ga transducers based on solenoids which force the collinear configuration will become increasingly attractive as was discussed in Chapter 1.



## CHAPTER 3

### CHARACTERIZATION OF NI-MN-GA IN COLLINEAR STRESS-FIELD CONFIGURATION

#### 3.1 Discussion of the Collinear Stress-Field Configuration

The work presented in this dissertation differs from the literature in that it focuses on Ni-Mn-Ga driven with a magnetic field aligned with the stress loading as shown in Figure 1.1. According to the theory of twin variant reorientation presented in the literature and discussed in Chapter 2, a collinear field-stress configuration is not expected to produce reversible strain since both the field and the stress favor the same variant and hence there will be no restoring force when the field is removed. Early testing at The Ohio State University indicated the capability for reversible strain in several samples of Ni-Mn-Ga when tested in the collinear configuration in a solenoid transducer [52]. A  $\text{Ni}_{48.1}\text{Mn}_{30.6}\text{Ga}_{21.3}$  sample showed reversible compressive strain of  $\epsilon = -0.26\%$  while a  $\text{Ni}_{48.99}\text{Mn}_{29.98}\text{Ga}_{21.03}$  sample strained  $-0.07\%$  and a  $\text{Ni}_{50}\text{Mn}_{28.7}\text{Ga}_{21.3}$  sample strained  $-0.41\%$ . These unexpected results motivated further investigation into the behavior of Ni-Mn-Ga samples exposed to collinear field and stress and led to the characterization and modeling results presented in this document.

The capability for reversible strain in Ni-Mn-Ga under a collinear field and stress with no *externally* applied restoring force indicates the presence of *internal* restoring forces that drive the twin boundaries back to an equilibrium configuration when the applied field is removed. These internal forces are hypothesized to be due to inclusions, dislocations, retained austenite, and residual stresses in the samples. Pinning of twin boundaries was first investigated as impediments to the 6% strain possible in the orthogonal field-stress configuration by Marioni [56]. In this work short magnetic field pulses of various magnitudes were applied to samples of Ni-Mn-Ga and a distribution of pinning site energies with a mean of around  $1.06 \times 10^5 \text{ J/m}^3$  were measured. This work has recently been continued by Richard [76] who used transmission electron microscopy to identify inclusions of gallium sulfide, titanium-rich coherent particles, and tantalum plates of various shapes and sizes. He also reports on the strain fields in the material due to these inclusions. It was found that the smaller defects can be overcome by the magnetic field, allowing twin boundary motion, while the larger ones cause the twin boundary to bow around them, limiting the possible twin boundary motion. These imperfections, which cause detrimental effects to the strain of the samples when used in the orthogonal configuration, are precisely what makes it possible for reversible strain to exist in the collinear configuration. Investigations into how the various imperfections can be induced and which types of imperfections enable the best strain performance are currently in progress.

### 3.2 Solenoid Transducer Design

In order to test the Ni-Mn-Ga samples in a configuration where the externally applied field and stress are collinear along the sample axis, a solenoid test transducer

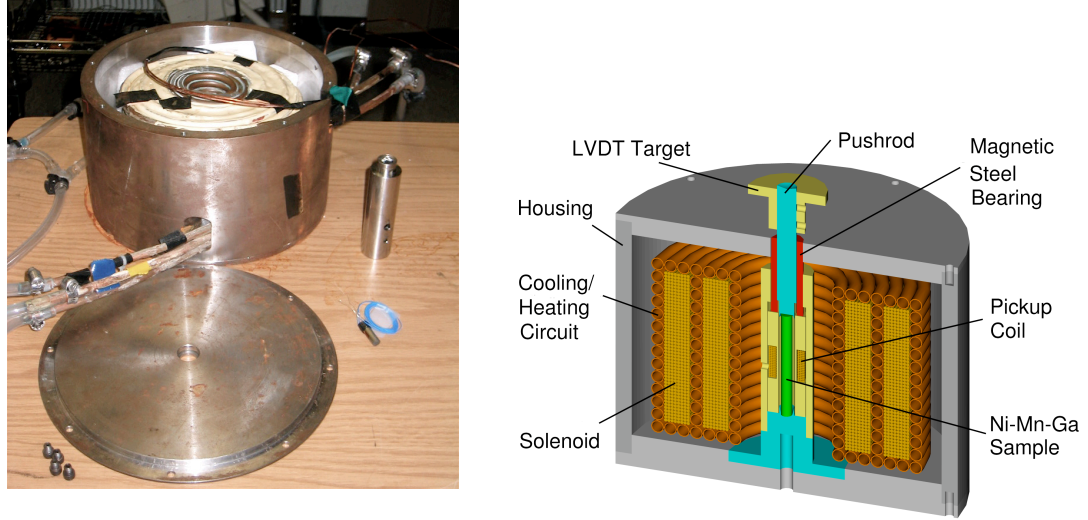


Figure 3.1: Solenoid based test transducer.

was designed and built (Figure 3.1). The transducer, which represents a modification of the water cooled transducer used to test Terfenol-D by Kellogg [36], is described in detail by Malla [51]. The three major components of the transducer are: (1) magnetic circuit, (2) water-cooled driving coil, and (3) sensing elements.

### 3.2.1 Magnetic Circuit

As was discussed in Chapter 1, one of the primary benefits of solenoid transducers over electromagnets is that the inclusion of the sample in a closed magnetic circuit greatly reduces leakage and therefore increases the efficiency and bandwidth of the transducer. Figure 3.2 shows the magnetic circuit; design drawings are included in Appendix A.

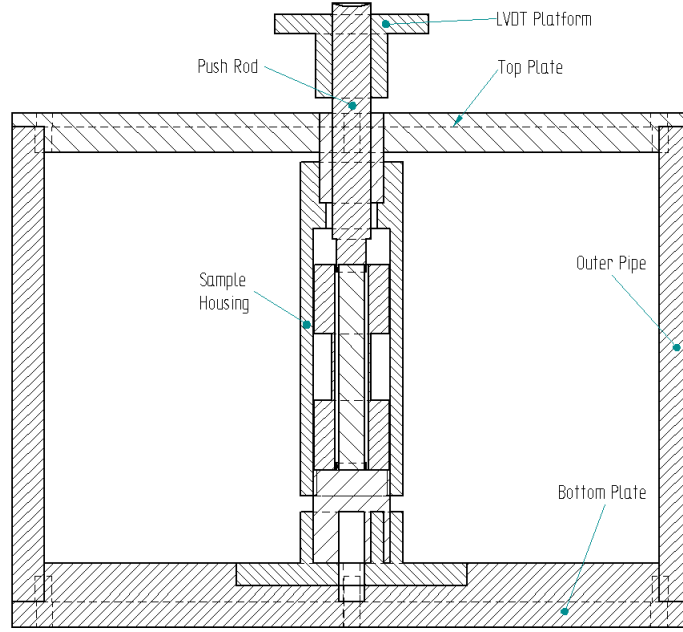


Figure 3.2: Magnetic circuit components for solenoid transducer.

The outer casing of the cylindrical transducer is made of standard 8.6 inch OD AISI 1018 magnetic steel pipe with a 0.3 inch wall thickness. The top and bottom plates of the outer casing are also made of AISI 1018 magnetic steel that ensures that most of the field produced through the center of the coil passes through the transducer casing and does not leak into the environment, improving both efficiency and safety.

The detail view in Figure 3.3 shows the components of the transducer that occupy the center of the driving coil. The central section is an independent sample housing that has an AISI 303 non-magnetic stainless steel outer housing. The bottom of the sample housing is an AISI 1144 stress proof magnetic steel bottom cap. The top is a magnetic steel linear ball bearing which is press fit into both the sample housing

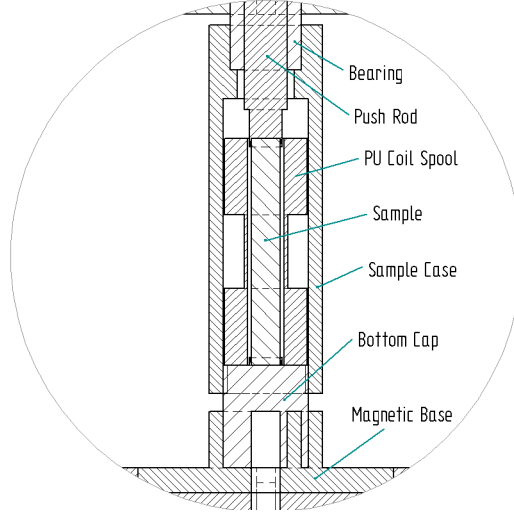


Figure 3.3: Components of the central section of the experimental transducer.

and the top plate of the outer casing. The sample casing is designed to accommodate samples of lengths ranging from 1 to 2 inches. For samples shorter than the full 2 inches magnetic steel end extensions are attached to the Ni-Mn-Ga with wax in order to center the sample in the magnetic field. An AISI 1144 push rod sits on top of the extended sample and passes through the bearing, closing the magnetic circuit into the top plate of the outer housing and allowing for the sample to be loaded and the strain to be measured. The transducer's magnetic circuit is completed at the bottom through an AISI 1018 magnetic steel base which connects the sample housing with the bottom plate of the outer housing. This combination of magnetic and non-magnetic components in the sample housing forces the magnetic flux through the sample.

### 3.2.2 Water Cooled Driving Coil

The test transducer can produce magnetic fields of up to 8.1 kG by way of a water cooled solenoid. The water cooling is provided by running water through three layers of copper tubing that are interspersed through the solenoid. This cooling is necessary to avoid melting the insulation on the copper wires, which occurs at 200 °C, and to avoid transforming the sample into austenite, which occurs at 42 °C for the  $\text{Ni}_{50}\text{Mn}_{28.7}\text{Ga}_{21.3}$  sample.

The solenoid was constructed by hand by winding copper tubing and AWG15 copper wire on an aluminum bobbin. The inner most layer consists of 12 turns of 1/4 inch copper tubing which was filled with casting sand in order to avoid buckling. A cut was made in the inner most turn of copper in order to remove the sand and then the coil was welded back together. The copper tubing spiral was then filled in with silver solder and machined to provide a smooth surface allowing an even coil to be wound to provide a uniform magnetic field inside the coil. Twelve layers of AWG15 copper magnet wire were wound averaging 48 turns per layer. Structural integrity was strengthened and thermal conductivity of the coil was increased through the application of Epotek T7109 epoxy every two layers. The partial coil was cured after 12 layers of wire were wound and then a second layer of 1/4 copper tubing was wrapped and filled in with epoxy containing copper powder to increase its thermal conductivity. Sixteen more layers of wire were then wound and cured as before and a final layer of copper tubing was placed as the outer layer of the coil. The top and bottom of the coil consists of spirals of copper tubing to complete the cooling circuit. A specific schematic of the coil is shown in Figure 3.4. The final product has 3 layers of cooling tubes surrounding a 1350 turn coil with an inner diameter of 1.3

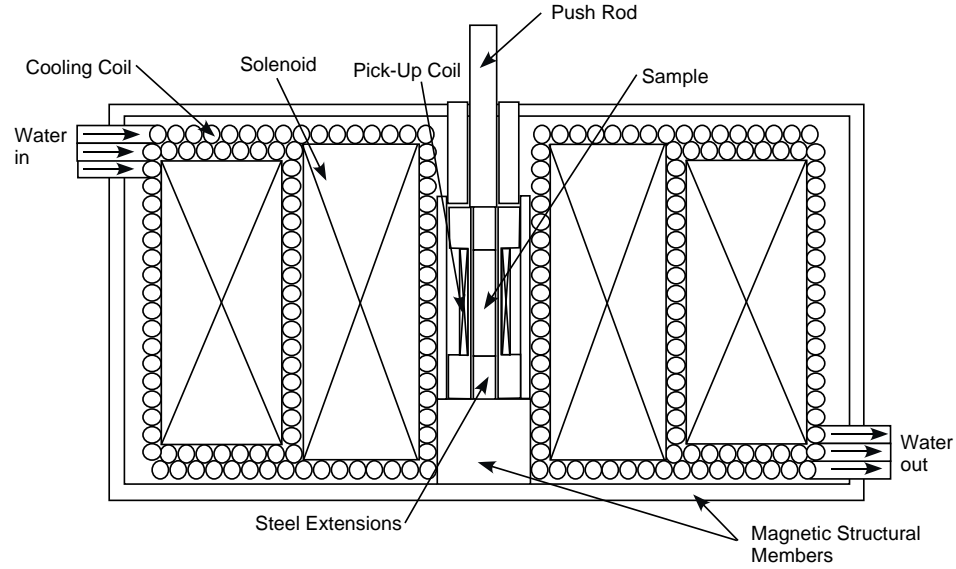


Figure 3.4: Coil schematic showing various components of the water cooled driving coil.

inches and an outer diameter of 6 inches. The resistance is  $3.7 \, \Omega$ ; when driven with a pair of Techron 7790 amplifiers, which are capable of a voltage gain of 60 and 56 A of current, it can create a field of 8.1 kG. This field was mapped using a Walker Scientific MG-4D Gaussmeter and was found to be constant to within 20% over the location of the sample as is shown in Figure 3.5.

### 3.2.3 Sensing Elements

The transducer design described above allows for the measurement of both strain and magnetization. In addition, thermocouples are used to monitor the temperature of the system at four locations including the inlet and outlet of the cooling coils, the inner surface of the solenoid, and the non-magnetic steel sample housing close to the

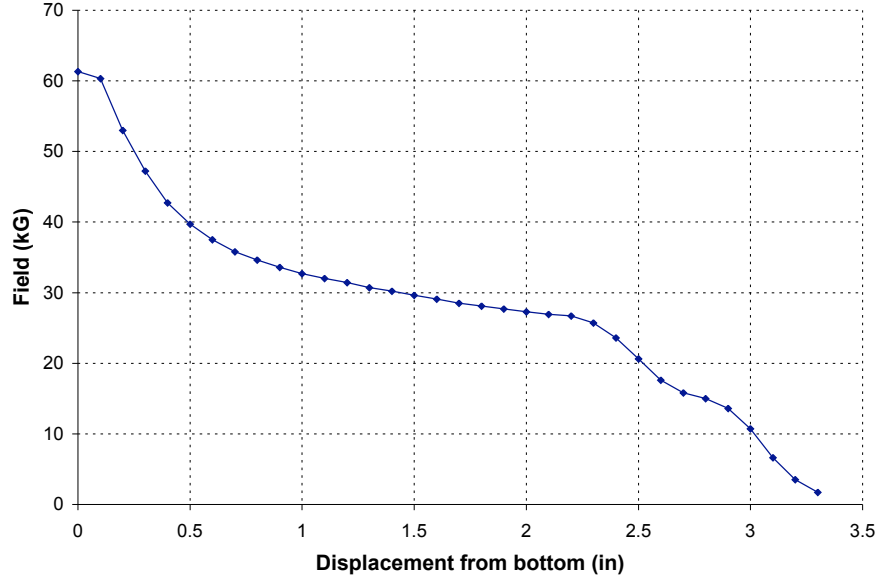


Figure 3.5: Variation of the magnetic induction at different heights from the bottom of the solenoid for 60V applied voltage.

sample. Using the thermocouples it is possible to ensure that all testing is done in the same temperature range and that the temperature variation as testing progressed is never larger than 1 °C. Adequate cooling time was provided between tests such that testing always began with the sample at a temperature of 14 °C.

The strain is measured with a linear variable differential transducer (LVDT) which is mounted to the pushrod in the solenoid transducer shown in Figure 3.1. The Lucas Shaevitz MHR-025 LVDT has a sensitivity of 1.26 V/mil over a range of 5 mils. By comparing strain measurements collected using the LVDT with those measured from a strain gage mounted on the sample it was found that a correction factor of 0.6 needed to be used to account for the magnetostriction and magnetic forces on the steel components of the magnetic circuit.



The magnetization of the Ni-Mn-Ga sample as the field was cycled was determined by way of the voltage induced in a pick-up coil that surrounds the sample. The pick-up coil is wound of AWG 33 copper wire on an aluminum spool and consists of 216 turns in two layers. It is connected to a Walker Scientific MF-5D integrating fluxmeter which calculates the induction in the sample by way of the equation

$$V = N \frac{d\phi}{dt} = \frac{NA}{RC} B \times 10^{-8} V \quad (3.1)$$

where  $B$  is the induction,  $NA$  is the number of turns per length times the coil cross-sectional area and is entered into the meter, and  $RC$  is the input scaling factor. The relation

$$\mathbf{B} = \mu_0(\mathbf{H} + \mathbf{M}) \quad (3.2)$$

is then used to determine the magnetization of the sample,  $\mathbf{M}$ .

### 3.2.4 Transducer Modifications

A second solenoid transducer was also constructed incorporating minor design modifications which makes it more appropriate for high frequency testing. These modifications include:

- The outer casing was cut vertically in order to eliminate eddy currents which contribute to energy losses at high frequencies.
- The inner coil of the cooling tubing was replaced by a copper cooling sleeve which is shown in the appendix in Figure A.22. This eliminated the problems due to the compaction of the filling sand and provided a smooth surface on which to wind the drive coil creating a more uniform field.

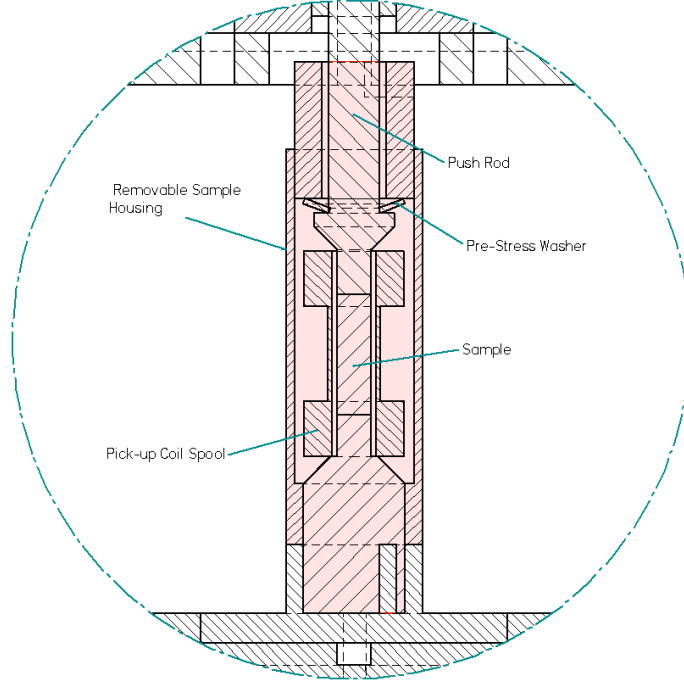


Figure 3.6: Components of the central section of the prestress capable modified transducer.

- The inner casing was replaced by a self-contained sample housing that incorporates a prestress mechanism and is removable. The component parts of this sample house are labeled in Figure 3.6; the machine drawing are included in Appendix A.

### 3.3 Review of Previous Quasi-Static Testing of $\text{Ni}_{50}\text{Mn}_{28.7}\text{Ga}_{21.3}$

The  $\text{Ni}_{50}\text{Mn}_{28.7}\text{Ga}_{21.3}$  sample that is used in this work was also part of a study performed by Malla et al. [51]. In that study Malla et al. investigated the effect of the composition of the Ni-Mn-Ga on the strain and magnetization. The primary

results for the  $\text{Ni}_{50}\text{Mn}_{28.7}\text{Ga}_{21.3}$  sample from Malla’s study are reproduced here for completeness.

### 3.3.1 Sample Manufacture

The  $\text{Ni}_{50}\text{Mn}_{28.7}\text{Ga}_{21.3}$  sample was manufactured by Dr. Thomas Lograsso at the DOE Ames Lab through the Bridgman technique. As described in [52], high purity nickel, manganese, and gallium were arc melted under an argon atmosphere and the alloy was drop cast into a chilled copper mold. This ingot was degassed in a Bridgman style crucible at 1350 °C under a pressure of  $1.3 \times 10^{-4}$  Pa. After degassing the chamber was backfilled with  $2.76 \times 10^5$  Pa of argon and the ingot was held at 1350 °C for 1 hour before being withdrawn from the heat zone at a rate of 5 mm/hr.

A quarter inch diameter, 0.883 inch long cylindrical sample was cut from the grown crystal by electric discharge milling. The exact composition of the sample was found along its longitudinal axis by energy dispersive microanalysis. Testing was also performed that identified the austenitic and martensitic start and finish temperatures and the Curie temperature at the top and bottom of the sample. These are shown in Table 3.1.

	$A_s$	$A_f$	$M_s$	$M_f$	$T_c$ (heating)	$T_c$ (cooling)
top	42.0 °C	65.9 °C	55.3 °C	32.4 °C	101.1 °C	98.0 °C
bottom	43.7 °C	62.5 °C	54.8 °C	33.1 °C	100.6 °C	98.2 °C

Table 3.1: Characteristic temperatures for  $\text{Ni}_{50}\text{Mn}_{28.7}\text{Ga}_{21.3}$ .

### 3.3.2 Strain Measurements

Figure 3.7 shows the strain vs field response of  $\text{Ni}_{50}\text{Mn}_{28.7}\text{Ga}_{21.3}$  at 0.1 Hz under a minimal load of 39g, which is the mass of the pushrod. A key aspect to note from this graph is that despite the lack of an externally applied restoring force the maximum strain of 0.41% is completely reversible as the field is cycled. The strain from Ni-Mn-Ga also exhibits frequency doubling with both positive and negative fields producing equi-magnitude compressive strains. The hysteresis in Figure 3.7 is an indication of losses inherent in Ni-Mn-Ga's transduction process between magnetic and mechanical energy. Because of these losses, the behavior of the material as the field is increased is substantially different from the behavior as the field decreases. Malla et al. found that the piezomagnetic coefficient,  $d_{33}$ , which relates the strain to the field is always smaller for a decreasing field than for an increasing field.

The saturation value of the strain in Figure 3.7 is an important indication of how useful the sample will be for various applications. The 0.41% saturation strain from the  $\text{Ni}_{50}\text{Mn}_{28.7}\text{Ga}_{21.3}$  is the largest reversible strain recorded for Ni-Mn-Ga driven by a collinear field and stress and no externally applied restoring force. The magnitude of this strain has been independently verified in standard electromagnet setups at Ames Lab (DOE) [74] and Naval Surface Warfare Center [75]. Though substantially smaller than the 6% strain achieved from samples with no internal pinning as recorded in the literature [67, 61, 43], this strain is more than three times that of other solenoid materials such as magnetostrictive Terfenol-D [14] and Galfenol [35].

Another important characteristic of the Ni-Mn-Ga sample that can be identified from the data in Figure 3.7 is the crossover point which was measured as 513 ppm for the 0.1 Hz test and increases with frequency. This strain remaining at zero field is due

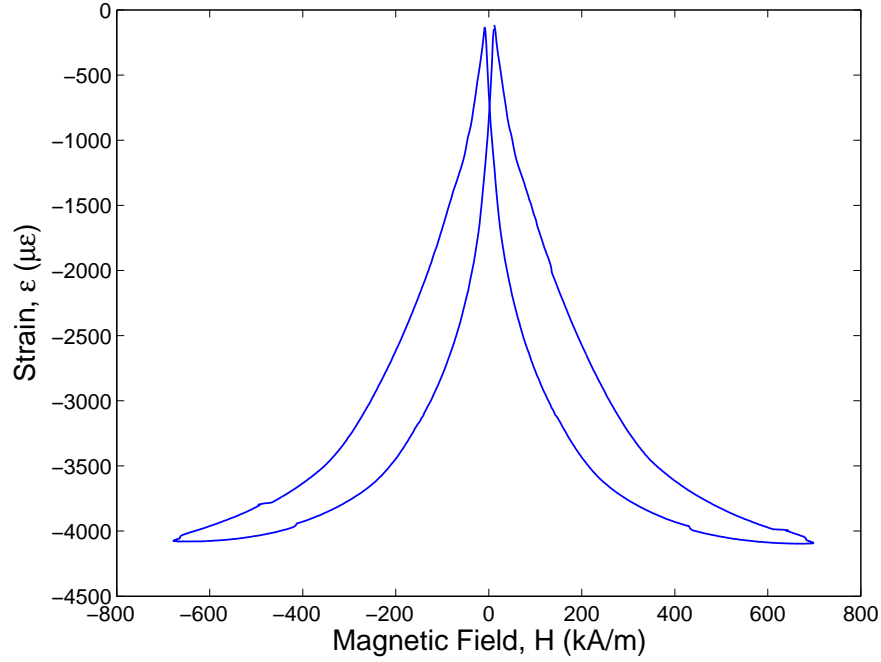


Figure 3.7: Strain vs magnetic field for  $\text{Ni}_{50}\text{Mn}_{28.7}\text{Ga}_{21.3}$  at zero load and 0.1 Hz.

at least in part to the remanence magnetization of the sample but more complicated effects related to twin boundary motion relaxation may also be possible [51].

Malla et al. also performed a series of tests which examined the effect of load on the strain output of the  $\text{Ni}_{50}\text{Mn}_{28.7}\text{Ga}_{21.3}$  sample. The results, in Figure 3.8, show the saturation strain for various applied loads. As can be seen, the strain levels achievable from the sample drops off quickly as the load is increased. This phenomenon suggests a limitation in the amount of useful work that is possible from these materials; this will need to be addressed for future applications. The blocking stress is defined as the stress level at which the strain output is due solely to the magnetostriction of the

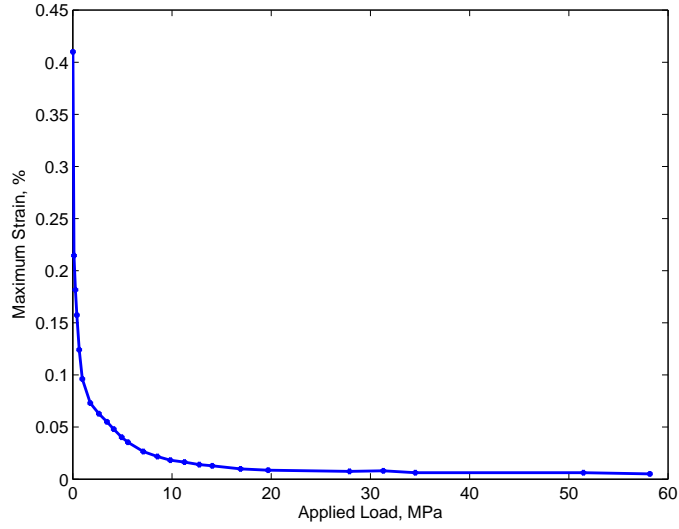


Figure 3.8: Maximum strain from  $\text{Ni}_{50}\text{Mn}_{28.7}\text{Ga}_{21.3}$  under various loads at 0.1 Hz.

Ni-Mn-Ga. This level is reached at a strain of 0.02% which occurs at a stress level of 15 MPa.

### 3.3.3 Magnetization Testing

Figure 3.9 shows the magnetization data collected at the same time as the strain data shown in Figure 3.7. The hysteresis in this data is very small but increases substantially as frequency is increased. Useful quantities measured from this data are included in Table 3.2

## 3.4 Dynamic Testing: Investigation of Modulus Shifts

Since many possible applications of Ni-Mn-Ga solenoid transducers will require operation in the dynamic regime, the testing presented by Malla et al. needed to be extended to higher frequencies. This section will present the results of testing unique

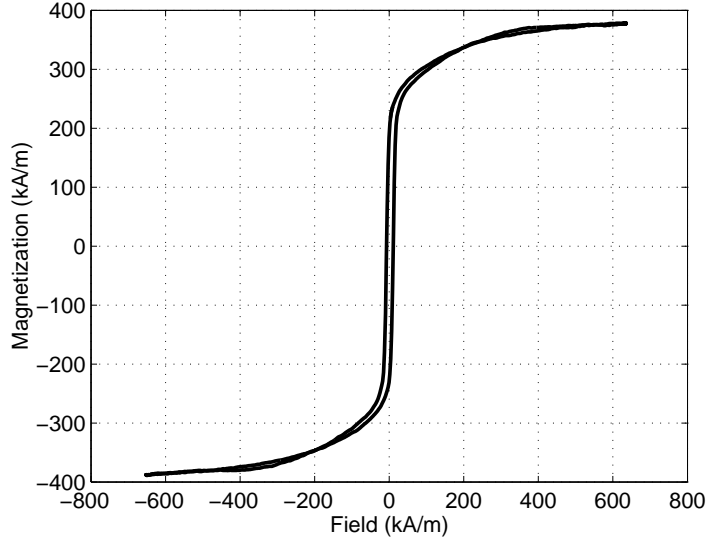


Figure 3.9: Strain vs magnetic field for  $\text{Ni}_{50}\text{Mn}_{28.7}\text{Ga}_{21.3}$  at zero load and 0.1 Hz.

Saturation Magnetization	$M_s$	381 kA/m
Coercive Field	$H_c$	8.83 kA/m
Remanent Magnetization	$M_R$	183.03 kA/m
Maximum Differential Permeability		38.16

Table 3.2: Magnetic properties for  $\text{Ni}_{50}\text{Mn}_{28.7}\text{Ga}_{21.3}$  at 0.1 Hz.

to this work which examined the frequency response of the  $\text{Ni}_{50}\text{Mn}_{28.7}\text{Ga}_{21.3}$  with particular focus on the dependence of the resonance behavior on bias dc magnetic field. Two experimental apparatuses were used: (a) magnetic excitation in which the bias fields are applied using a dc current through the drive coil and (b) mechanical excitation from a shaker with the bias fields provided through permanent magnets.

### 3.4.1 Magnetic Excitation

#### Experimental Apparatus

The broadband research transducer described in Section 3.2 is employed in these tests to measure the elastic modulus of the  $\text{Ni}_{50}\text{Mn}_{28.7}\text{Ga}_{21.3}$  sample under various loads and bias magnetic fields. AC magnetic fields are applied to the sample using swept sine excitation between 100 and 5000 Hz controlled with a SigLab 20-43 data acquisition system. The acceleration of the pushrod and the canister are measured using PCB 352C68 and U352C22 accelerometers mounted as shown in Figure 3.10. The frequency response of the accelerations to the current are collected and used to determine the resonances of the system. The modulus dependence on load and bias field is determined by applying loads ranging from 40 to 750 g and bias fields ranging from 0 to 130 kA/m. The schematic of the experimental setup is shown in Figure 3.11.

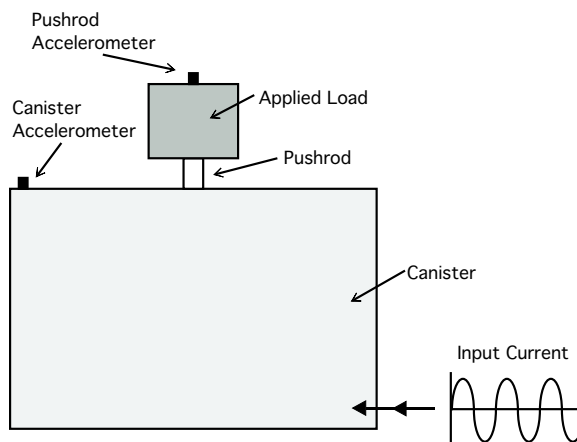


Figure 3.10: Research transducer as used for magnetic excitation modulus tests.



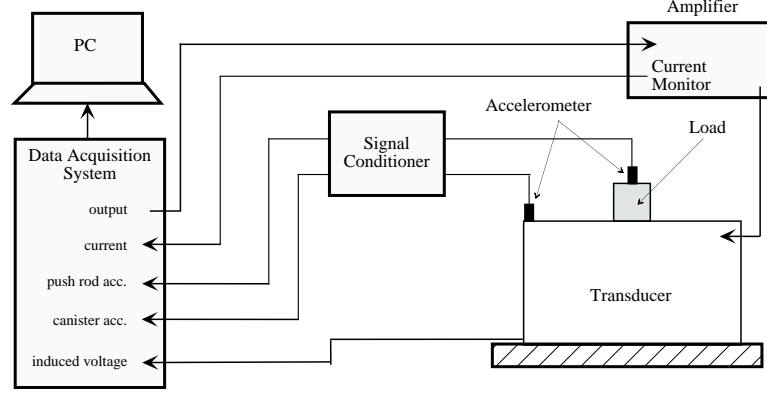


Figure 3.11: Experimental setup used for dynamic testing of Ni-Mn-Ga.

## Results

The frequency response of the research transducer shown in Figure 3.1 exhibits numerous resonance peaks. In order to determine which of these peaks is associated with the Ni-Mn-Ga element, the core material and mechanical load were varied and the frequency response of the acceleration of the canister and pushrod were compared. These comparisons revealed that the resonance peak most closely linked to the excitation of the sample is the peak located in the range of 0.5 to 1.5 kHz [20].

From a systems viewpoint, the transducer in Figure 3.10 can be approximated as a 1 degree of freedom second order system. Mechanically, this system can be described with the governing equation

$$m\ddot{x} + b\dot{x} + kx = F(t) \quad (3.3)$$

where  $m$  is the dynamic mass of the system, which is the sum of the applied mass and one third the mass of the sample, end extensions, and pushrod;  $b$  is the internal damping of the sample;  $k$  is the effective stiffness of the combination of Ni-Mn-Ga

sample, end extensions, and pushrod;  $x(t)$  is the displacement of the top of the sample; and  $F(t)$  is the force on the sample generated from the application of a magnetic field. Observing that Ni-Mn-Ga driven with collinear magnetic fields and stresses responds to applied fields in a manner which is phenomenologically similar to giant magnetostrictive materials, an expression for  $F(t)$  can be derived from the standard linear piezomagnetic equation

$$\epsilon = s^H \sigma + d^T H, \quad (3.4)$$

which states that the strain,  $\epsilon$ , is produced by a combination of the stress  $\sigma$  and the applied magnetic field  $H$ . Parameter  $s^H$  is the compliance at constant field and  $d^T$  is the piezomagnetic coefficient at constant stress. Since  $\sigma$  can be written as  $\frac{F}{A}$  where  $A$  is the cross-sectional area, and  $H = nI$  where  $I$  is the current through a coil of  $n$  turns per length, Equations (3.3) and (3.4) can be combined into an expression for the frequency response

$$\frac{\ddot{X}}{I}(j\omega) = \frac{-K\omega^2}{(k_{eff} - m\omega^2) + jb\omega}, \quad (3.5)$$

which is of the standard second order form with an extra double derivative made necessary by the fact that the acceleration is measured rather than displacement. Hence, the resonance frequency  $f$  of the system can be related to the mass and stiffness by

$$(2\pi f)^2 = \frac{k}{m}. \quad (3.6)$$

Figure 3.12 shows the resonance frequency measured for various mechanical loads under a fixed 1.1 kOe (86.2 kA/m) dc bias field and 82.7 Oe (6.6 kA/m) ac field amplitude. The close correlation between the relationship predicted by Equation (3.6)

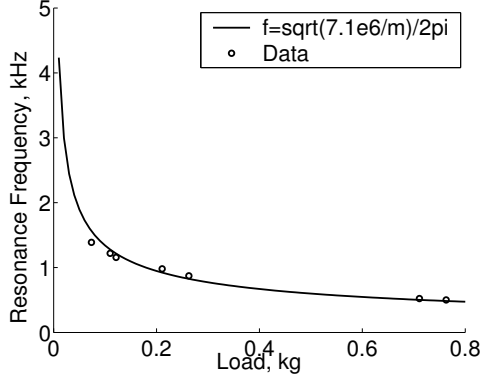


Figure 3.12: Comparison of experimental and 1DOF model results for frequency ( $f$ ) as a function of load ( $m$ ).

and the experimental data shows the validity of the one-degree of freedom model over the region of interest.

Figures 3.13(a) and 3.14(a) show the frequency response functions of the pushrod acceleration to current for loads of 60 and 250 grams respectively under the influence of various dc bias fields ranging from 0 to 1.6 kOe (0 to 129.3 kA/m). The shift in resonance frequency toward higher values indicates a stiffening of the Ni-Mn-Ga sample as bias field is increased, which correlates to a shift in the elastic modulus of the sample. The modulus can be calculated by assuming the standard linear model for rod vibration

$$k = \frac{AE}{l}, \quad (3.7)$$

where  $A$  is the cross-sectional area of the rod,  $l$  is the length of the rod, and  $E$  is the elastic modulus. The modulus shift relative to zero field is defined by  $\frac{E-E_0}{E_0}$  and is shown for different field levels in the top panel of Figure 3.13(b) and 3.14(b). The bottom part of the figures show the relationship between the heights of the resonance

peaks (shown as circles) and the diamonds representing  $C\omega^2\sqrt{km}$  which is the expected magnitude of the frequency response function (3.5) evaluated at resonance, where  $C$  is an appropriately chosen constant. As can be seen, the shift in elastic modulus for the 60g case is monotonically increasing with a magnitude of 82% for a 1.5 kOe increase in bias field while the 250g case has a total modulus shift of 210% with a 1.5 kOe increase in bias field.

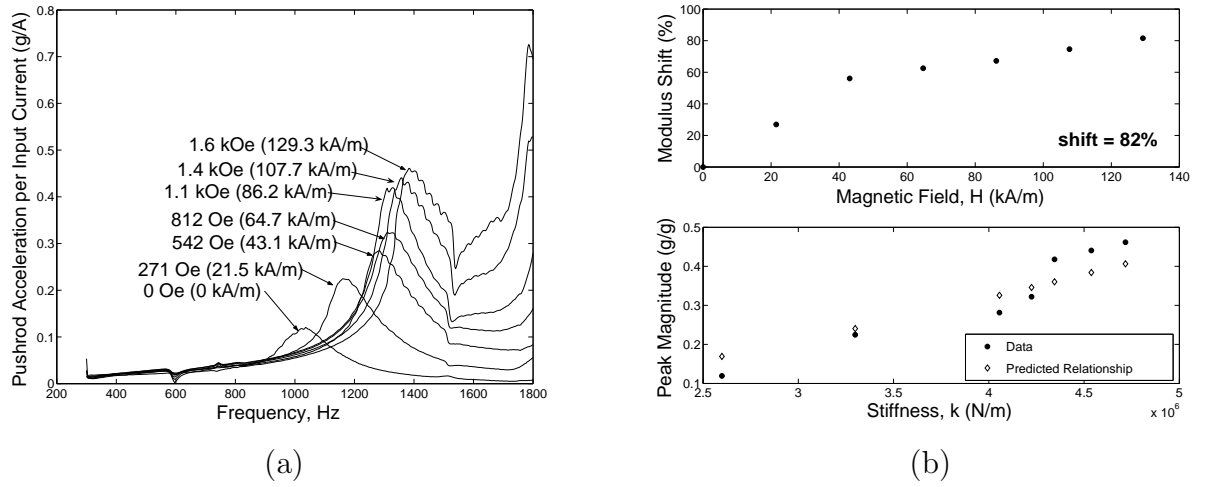


Figure 3.13: Dynamic magnetic excitation of  $\text{Ni}_{50}\text{Mn}_{28.7}\text{Ga}_{21.3}$  for various applied bias fields and 60 gram load.

### 3.4.2 Mechanical Excitation

#### Experimental Apparatus

The reaction of the steel components in the broadband transducer to the large generated magnetic fields might affect the magnitudes of the modulus shifts measured using magnetic excitation. In order to address these challenges and verify this effect,

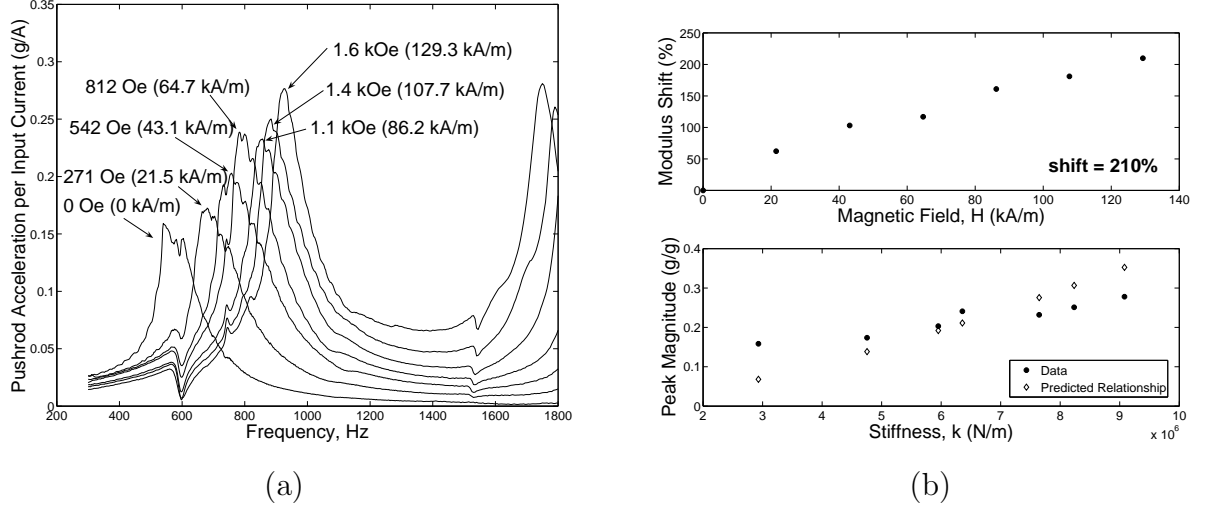


Figure 3.14: Dynamic magnetic excitation of  $\text{Ni}_{50}\text{Mn}_{28.7}\text{Ga}_{21.3}$  for various applied bias fields and 250 gram load.

the Ni-Mn-Ga sample can be isolated from the transducer using the configuration shown in Figure 3.15. In this arrangement, the sample is mounted to the top of a Labworks ET-126 shaker driven by a Labworks PA-138 amplifier. The sample is placed in series with different combinations of Nd-Fe-B permanent magnets in order to create bias magnetic fields of between 6.24 and 379.2 kA/m. Loads ranging from 0 to 250g are mounted on top of the sample. The outputs from the system include the accelerations of the platform ( $\ddot{x}_1$ ) and the load ( $\ddot{x}_2$ ), which are measured using PCB U353B16 and U353C22 accelerometers. The input is the displacement of the platform ( $x_0$ ) which is controlled using a swept-sine excitation from 100 to 10000 kHz provided by a SigLab 20-42 data acquisition system. The frequency response of the acceleration of the load to that of the platform is recorded to determine the resonance frequency and calculate the elastic modulus of the sample.

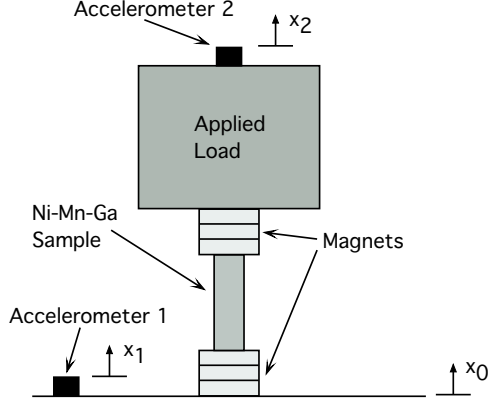


Figure 3.15: Shaker set-up used for dynamic modulus shift verification.

## Results

Results for these tests are shown for the 50 gram external load case in Figure 3.16. It is noted that in this experimental set up, in order to increase the magnetic field in the sample it is necessary to also increase the mass on the sample. This makes it difficult to identify trends in the raw data though these trends can be easily derived through a systems approach. The system described in Figure 3.15 can be approximated as a 1 degree of freedom system with base excitation and the frequency response function can be written as

$$\frac{X_2}{X_0}(j\omega) = \frac{\ddot{X}_2}{\ddot{X}_1}(j\omega) = \frac{j b \omega + k}{-m \omega^2 + j b \omega + k}. \quad (3.8)$$

Thus, the expression for resonance frequency is once again given by Equation (3.6) which can be used in combination with Equation (3.7) to calculate the elastic modulus of the sample taking into account the increase in load due to the addition of magnets on the top of the rod. The shift in elastic modulus relative to its value at zero field is calculated and plotted in Figure 3.17 for various loads. The lower panel of the

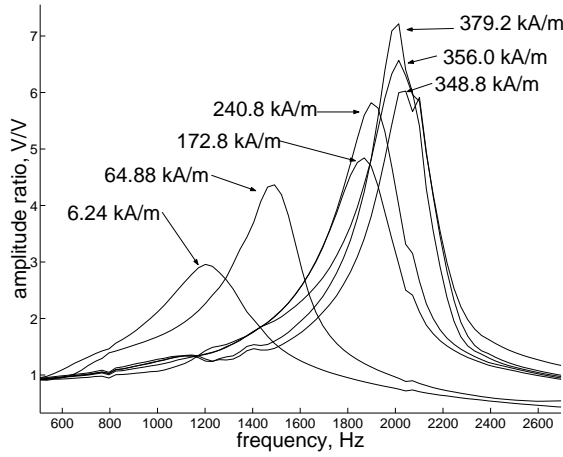
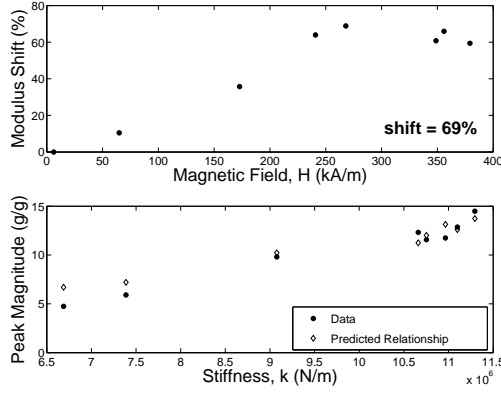


Figure 3.16: Dynamic mechanical excitation of Ni-Mn-Ga for various applied fields and a 50g load.

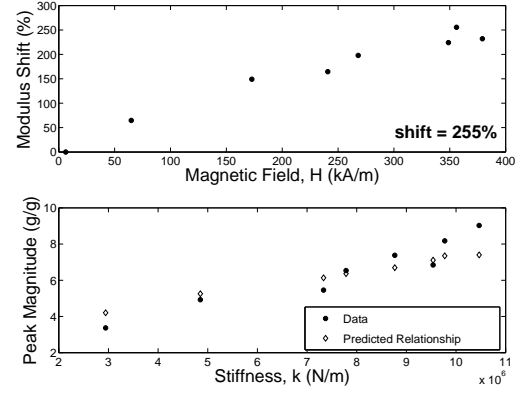
individual plots in this figure once again show the amplitudes of the resonance peaks compared to the expected trend based on the magnitude of the transfer function (3.8) at resonance that is proportional to  $1 + C\sqrt{km}$ . With a 373 kOe increase in bias field the overall increase in modulus varies between 52% and 255%. The dependence of the magnitude of this shift on externally applied loads suggests the existence of an optimal load for maximum modulus shift.

### 3.4.3 Discussion of Results

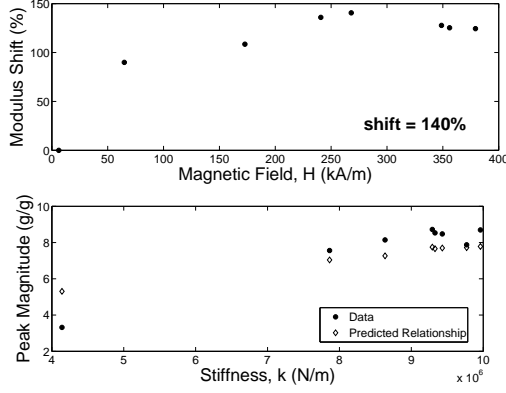
Two important facets of the modulus shift effect can be identified based on the results presented in the previous sections. The first is the large shift in modulus as the bias magnetic field is increased that is quantified as being between 52% and 255% for various load and excitation conditions. These shifts are analogous to shifts seen in connection with the Delta-E effect in Terfenol-D [10, 21] and other magnetic



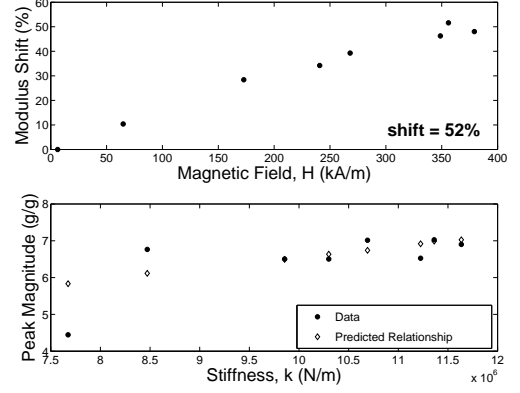
(a) 20 gram load



(b) 50 gram load



(c) 100 gram load



(d) 250 gram load

Figure 3.17: Calculated elastic modulus shift and damping trend for various loads.

materials [4, 9] and are extremely promising for applications in tunable vibration absorbers. A modulus decrease occurs in any material that exhibits strain caused by mechanisms other than elastic strain [13]. This is called a *modulus defect*, of which the elastic modulus shift in magnetic materials caused by the dependence of strain on magnetization is a special case.



In the case of Ni-Mn-Ga, as a bias magnetic field is applied to the sample the variants with their shorter c-axis aligned with the field are favored and grow by way of twin boundary motion. This has two effects: (a) the initial magnetization is biased towards the saturated state since the unit cell's magnetization vector is fixed to the c-axis, and (b) it also decreases the amount of strain that is possible from twin boundary motion. The amount of additional strain possible beyond the elastic strain is directly related to the decrease in elastic modulus from that of the material when only elastic strain is possible [13]. Thus, as the bias field is increased from the zero-field case, the modulus will also increase toward its saturation value as is apparent from the shifts of up to 255% in Figures 3.13, 3.14, and 3.17. The plots in Figure 3.17 also highlight the fact that the modulus changes less as the bias field approaches the level where the sample is saturated.

The second aspect of the modulus shift effect is its nonlinear dependence on the applied load and the existence of an optimal external load for largest percent shift. In the case of the magnetically excited system the modulus shift increased from 82% to 210% as the load was increased from 20 to 250g. For the mechanically excited system there is an optimal load between 20 and 100g where there is a shift of more than 250%. This dependence on load is a consequence of the nonlinear nature of the stress-strain curve seen in Figure 3.18. As a stress is applied to the Ni-Mn-Ga sample the material exhibits an initial purely elastic strain due to the compression of inter-atomic bonds, followed by strain due to twin boundary motion that allows the large overall deformation of the material. The elastic modulus changes substantially through these two regions that translates into a dependence of modulus on load. When a bias magnetic field is applied to the sample it initializes the twin boundary

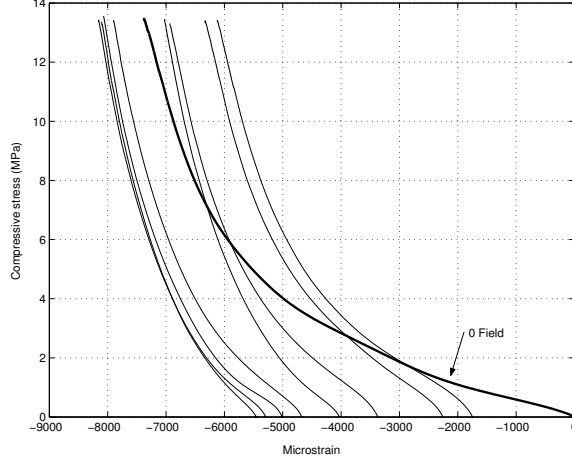


Figure 3.18: Loading stress-strain curves for Ni-Mn-Ga under various bias fields [51].

strain prior to the elastic strain, changing the shape of the stress-strain curve and the relationship between stress and elastic modulus. This change in the stress dependence of the elastic modulus as the bias field is varied implies that the modulus shift with magnetic field will also show a related stress dependence. Similar dependencies are seen in other magnetic materials as discussed by Bozorth [4].

By way of review the modulus shifts for various conditions are shown in Table 3.3. These modulus shifts qualitatively agree with shifts that would be expected due to the additional strain possible because of magnetically induced twin boundary motion in Ni-Mn-Ga. The existence of these shifts and their dependence on the external load agree with results reported in the literature for Terfenol-D and other more mildly magnetostrictive materials although the strain mechanisms are significantly different.

Excitation	Load	Bias Field Variation	Modulus Shift
Magnetic	60g	0 to 130 kA/m	82%
Magnetic	250g	0 to 130 kA/m	210%
Mechanical	20g	0 to 380 kA/m	69%
Mechanical	50g	0 to 380 kA/m	255%
Mechanical	100g	0 to 380 kA/m	140%
Mechanical	250g	0 to 380 kA/m	52%

Table 3.3: Summary of results for modulus shift with varying magnetic field.

### 3.5 Concluding Remarks

This chapter has presented the results of the experimental characterization of a sample of  $\text{Ni}_{50}\text{Mn}_{28.7}\text{Ga}_{21.3}$  excited in a collinear field-stress configuration. A review of previous testing by Malla et al. showed the capability of this sample for reversible strain of up to -0.42% driven by a low frequency sinusoidal current. This data was extended into the dynamic domain, most likely to be seen in applications, through a series of swept-sine excitation tests of the sample under various loads, bias fields, and through both magnetic and mechanical excitations. The data collected for the dependance of stiffness and damping on applied field will be invaluable for the future development of control strategies for Ni-Mn-Ga based solenoid transducers. In addition, these tests show evidence of a shift in modulus with bias field of over 250% that makes this technology extremely promising for variable stiffness applications like vibration control.

## CHAPTER 4

### MODELING OF THE FERROMAGNETIC SHAPE MEMORY EFFECT

The experimental results presented and discussed in the previous chapter indicate the promise of solenoid based transducers employing Ni-Mn-Ga in a collinear magnetic field and stress configuration for applications ranging from positioning to variable stiffness vibration control. In order to fully achieve this promise, a more thorough understanding of the physical mechanism behind this unexpected reversible strain needs to be sought. In addition, modeling needs to be implemented such that the strain can be predicted to facilitate implementation, design, and control of solenoid based Ni-Mn-Ga transducers.

This chapter describes the proposed modification of the strain mechanism presented in Chapter 2 in which pinning sites caused by imperfections in the Ni-Mn-Ga sample provide an internal restoring mechanism that makes reversible strain feasible but also reduces the magnitude of the strain. An energy based mathematical description of this mechanism is then developed following techniques similar to those used by Kiefer and Lagoudas [39, 38] which results in an idealized kernel simulation for the strain vs field curves. Finally, a stochastic homogenization method is employed that results in an accurate simulation of the strain at various mechanical loads. This

method is based on techniques used by Smith et al. [80, 81, 17, 16] for various other smart materials.

## 4.1 Parallel Configuration Strain Mechanism

The strain mechanism proposed to explain the reversible strain in some samples of Ni-Mn-Ga under collinear stress and field is illustrated in Figure 4.1. A modification to the mechanism described in Section 2.2.2 is proposed to include the presence of pinning sites in the martensite that provide an internal restoring force allowing for reversible strain. The pinning sites, which are physically large sulfide inclusions, are presented by black dots in Figure 4.1. Pinning occurs as the twin boundary bends around the inclusions; it will be modeled as simple spring behavior. The pinning sites are assumed to have energies too large to be overcome by the applied field.

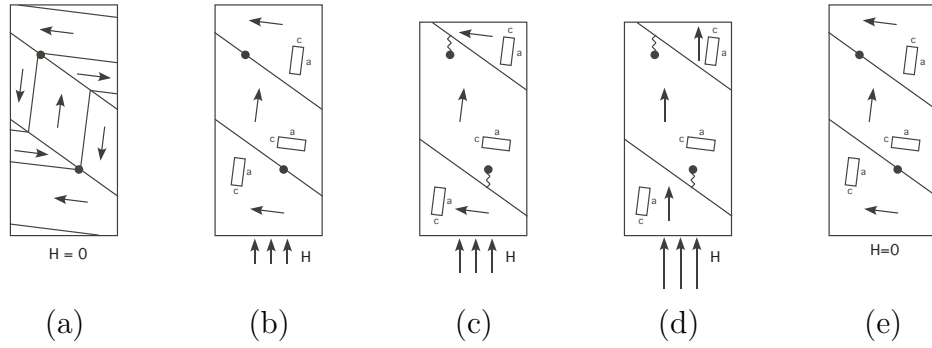


Figure 4.1: Strain mechanism for Ni-Mn-Ga driven by a collinear stress and field pair in the presence of pinning sites. (a) No field applied. (b) - (d) Sample contraction due to increasing field. (e) Return to original length with the field is removed.

When exposed to axial magnetic fields the twin boundaries attempt to displace according to the standard mechanisms for twin variant reorientation, as in panels (b)-(c), but the field does not provide enough energy to overcome the energy barrier provided by the pinning sites. Instead, the twin boundaries displace as much as possible; as they do work against the pinning sites, energy is dissipated. Saturation is achieved when the field energy is large enough to overcome the anisotropy energy and the magnetic moments align with the field without changing the orientation of the crystal (panel (d)). When the field is removed (panel (e)) the anisotropy energy returns the magnetic moments to the easy c-axis of the crystal and the elastic pinning site energy provides a restoring mechanism for the twin boundary, returning the sample to its original length and magnetization. This theory provides an explanation for the smaller magnitude of strain possible from this sample and for the fact that the strain measured in the absence of an external restoring force is reversible.

## 4.2 Gibbs Free Energy Formulation

To model the strain produced by Ni-Mn-Ga driven by collinear magnetic fields and stresses, a thermodynamics approach similar to that presented by Kiefer and Lagoudas [39] is considered. An additional term due to internal orthogonal stresses has been included in the Gibbs energy function which quantifies the restoring force found in experiments [19]. For simplicity, we assume that the structure comprises two variant orientations described by the two-dimensional representation shown in Fig. 4.2. Variant 2 is favored by an axially applied field in the y-direction and has a volume fraction of  $x$ . Variant 1 is the transverse variant with magnetization vectors oriented orthogonal to the applied field and a volume fraction of  $(1 - x)$ .

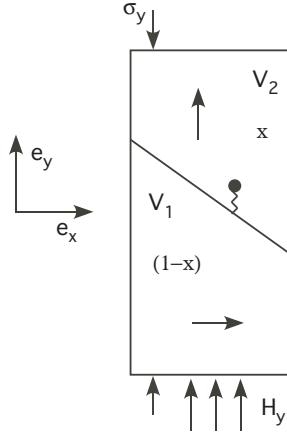


Figure 4.2: Two-dimensional variants: notation and orientation.

The material described in Fig. 4.2 can thus be treated as a mixture of variants. The energy for this system is given by

$$G(\boldsymbol{\sigma}, \mathbf{H}, T, x, a) = (1 - x)G_1(\boldsymbol{\sigma}, \mathbf{H}, T, a) + xG_2(\boldsymbol{\sigma}, \mathbf{H}, T, a) + G_b \quad (4.1)$$

where  $G_i$  is the energy of the  $i$ -th variant and  $G_b$  is the energy of the boundary between the two variants. The independent variables in the Gibbs free energy expressions are the applied stress,  $\boldsymbol{\sigma}$ , applied field,  $\mathbf{H}$ , and temperature,  $T$ , of the system, which can be controlled experimentally. In addition, internal variables are included representing the variant volume fraction,  $x$ , and magnetic domain volume fraction,  $a$ . The general form of the Gibbs free energy of each variant can be written as

$$G_i(\boldsymbol{\sigma}, \mathbf{H}, T) = \psi_i - G_{mech,i} - G_{mag,i} + G_{them,i} \quad (4.2)$$

where  $\psi_i$  is the Helmholtz energy for the variant that is defined as

$$\psi_i = u_i - s_i T \quad (4.3)$$

where  $u$  is the internal energy and  $s$  is the entropy of the system.

The mechanical energy,  $G_{mech,i}$ , includes contributions due to compliance and thermal expansion of the sample. In general vector form this energy is written as

$$G_{mech,i} = \frac{1}{2\rho} \boldsymbol{\sigma} \cdot \mathbf{S}_i \boldsymbol{\sigma} + \frac{1}{\rho} \boldsymbol{\sigma} \cdot \boldsymbol{\alpha}_i (T - T_0) \quad (4.4)$$

where  $\rho$  is the density of the Ni-Mn-Ga sample,  $\mathbf{S}_i$  is the tensor compliance of the  $i$ -th variant, and  $\boldsymbol{\alpha}_i$  is the coefficient of expansion. Under the assumption that the experiments are isothermal, the second term in Equation (4.4) can be ignored. Additionally, the fact that the stress is applied unidirectionally along the  $y$ -axis of the rod allows for the reduction of the first term such that

$$G_{mech,i} = \frac{1}{2\rho} S_{yy,i} \sigma_y^2. \quad (4.5)$$

The magnetic energy, or Zeeman energy, is given as

$$G_{mag,i} = \frac{\mu_0}{\rho} [(1 - a) \mathbf{M}_{i,d1} + a \mathbf{M}_{i,d2}] \cdot \mathbf{H} \quad (4.6)$$

where  $\mathbf{M}_{i,dj}$  is the magnetization of the  $j$ -th domain in the  $i$ -th variant and  $\mu_0 = 1.256 \times 10^{-6} \text{ N/A}^2$  is the permeability of free space. Since the applied fields are much larger than the field necessary for all domains in a single variant to align,  $a$  is assumed to be 1 and

$$G_{mag,i} = \frac{\mu_0}{\rho} \mathbf{M}_i \cdot \mathbf{H} \quad (4.7)$$

where  $\mathbf{M}_i$  is the magnetization of the single magnetic domain present in the  $i$ -th variant is used as the simplified expression for the magnetic energy.

Finally, the thermal energy is given by

$$G_{th,i} = c \left[ (T - T_0) - T \ln \left( \frac{T}{T_0} \right) \right] \quad (4.8)$$



where  $c$  is the specific heat capacity. Under the isothermal assumption this entire energy contribution can be ignored.

Substitution of Equations (4.3), (4.5) and (4.7) into (4.2) and (4.1) yeilds

$$\begin{aligned}
G &= (1-x)G_1 + xG_2 + G_b \\
&= G_1 + x(G_2 - G_1) + G_b \\
&= \left( u_1 - s_1T - \frac{1}{2\rho}S_{yy,1}\sigma_y^2 - \frac{\mu_0}{\rho}\mathbf{M}_1 \cdot \mathbf{H} \right) \\
&\quad + x \left( u_2 - u_1 - s_2T + s_1T - \frac{1}{2\rho}S_{yy,2}\sigma_y^2 + \frac{1}{2\rho}S_{yy,1}\sigma_y^2 \right. \\
&\quad \left. - \frac{\mu_0}{\rho}\mathbf{M}_2 \cdot \mathbf{H} + \frac{\mu_0}{\rho}\mathbf{M}_1 \cdot \mathbf{H} \right) + G_b \\
&= \left( u_1 - s_1T - \frac{1}{2\rho}S_{yy,1}\sigma_y^2 - \frac{\mu_0}{\rho}\mathbf{M}_1 \cdot \mathbf{H} \right) \\
&\quad + x \left( \Delta u - \Delta sT - \frac{1}{2\rho}\Delta S_{yy}\sigma_y^2 - \frac{\mu_0}{\rho}\mathbf{M}_2 \cdot \mathbf{H} + \frac{\mu_0}{\rho}\mathbf{M}_1 \cdot \mathbf{H} \right) + G_b \quad (4.9)
\end{aligned}$$

where the  $\Delta$  operator refers to the difference between the two variants and  $\Delta u$  and  $\Delta s$  are zero since the internal energy and entropy of all variants are the same. Additionally, for the solenoid transducer shown in Fig. 1.1, both the applied stress and applied field are in the axial direction. Using the geometry specified in Fig. 4.2, the Zeeman energy terms can be written as

$$\mathbf{M}_1 \cdot \mathbf{H} = M_s \hat{\mathbf{e}}_x \cdot H_y \hat{\mathbf{e}}_y = 0 \quad (4.10)$$

$$\mathbf{M}_2 \cdot \mathbf{H} = M_s \hat{\mathbf{e}}_y \cdot H_y \hat{\mathbf{e}}_y = M_s H_y \quad (4.11)$$

which allows for the simplification of Equation (4.9) to

$$G = \left( u_1 - s_1T - \frac{1}{2\rho}S_{yy,1}\sigma_y^2 \right) + x \left( -\frac{1}{2\rho}\Delta S_{yy}\sigma_y^2 - \frac{\mu_0}{\rho}M_s H_y \right) + G_b. \quad (4.12)$$

The energy of the twin boundary stems from two sources. The first is the energy necessary to rotate a unit cell, which can be expressed as work done to overcome a

force. The second is the energy of the pinning sites, which can be modeled as that of a mechanical spring. Thus the boundary energy term has the form

$$G_b = \begin{cases} c_1x + k_1x^2 & \dot{x} > 0 \\ c_2x + k_2x^2 & \dot{x} < 0 \end{cases} \quad (4.13)$$

where  $k$  is the effective spring constant of the pinning sites,  $c$  is the energy associated with cell reorientation and the two branches of the function occur because the behavior of the material is not the same when the field is increasing and variant 1 is growing as it is when the field is decreasing and variant 1 is shrinking. It is noted that this expression has the same form as the *hardening function* employed by Keifer and Lagoudas [39] on the basis of shape memory arguments. This results in the final expression for the Gibbs free energy

$$\begin{aligned} G(\boldsymbol{\sigma}, \mathbf{H}, T = T_0) = & u_1 - s_1T - \frac{1}{2\rho}S_{yy,1}\sigma_y^2 + x \left[ -\frac{1}{2\rho}\Delta S_{yy}\sigma_y^2 - \frac{\mu_0 M_s}{\rho}H_y \right] + \\ & \begin{cases} c_1x + k_1x^2 & \dot{x} > 0 \\ c_2x + k_2x^2 & \dot{x} < 0 \end{cases} . \end{aligned} \quad (4.14)$$

The strain output from a Ni-Mn-Ga sample has two primary components: the thermoelastic strain,  $\boldsymbol{\epsilon}^{te}$  and the reorientation strain,  $\boldsymbol{\epsilon}^r$ . The thermoelastic strain is a reversible component contributed by the mechanical compliance of the sample. The reorientation strain is that portion of the strain that occurs when favorable variants grow when exposed to a magnetic field. In addition, the literature sometimes includes a detwinning strain,  $\boldsymbol{\epsilon}^d$ , that is the strain generated if a single variant is created from the self accommodated twin structure that results from the transformation from austenite to martensite. This quantity is generally a constant for a given sample and is not relevant in the situation presented here since the focus is on perturbations around an initial state and there is no initial biasing of the sample.

### 4.3 Complementary Driving Force

Having now derived an expression for the free energy, expressions for various thermodynamic quantities can be developed by employing the first and second laws of thermodynamics.

The first law of thermodynamics relates the work done on the system and the heat transferred into the system to the energy change of the system. It is expressed as [54]

$$\rho \dot{u} = \boldsymbol{\sigma} \cdot \dot{\boldsymbol{\epsilon}} + \mu_0 \mathbf{H} \cdot \dot{\mathbf{M}} - \nabla \cdot \mathbf{q} + \rho r^h \quad (4.15)$$

where  $u$  is the internal energy,  $\mathbf{q}$  is the heat flux vector, and  $r^h$  is a distributed internal heat source.

The second law of thermodynamics which places constraints on the direction of thermal processes can be expressed as [54]

$$\dot{s} - \frac{r^h}{T} + \frac{1}{\rho T} \nabla \cdot \mathbf{q} - \frac{1}{\rho T^2} \mathbf{q} \cdot \nabla T \geq 0 \quad (4.16)$$

where  $s$  is entropy and  $T$  is temperature.

Since both the first and second law are rate dependent the time rate of change of the Gibbs free energy given is found as

$$\frac{\partial G}{\partial t} = \dot{u} - \dot{s}T - s\dot{T} - \frac{1}{\rho} \left( \dot{\boldsymbol{\sigma}} \cdot \boldsymbol{\epsilon}^{te} + \boldsymbol{\sigma} \cdot \dot{\boldsymbol{\epsilon}}^{te} \right) - \frac{\mu_0}{\rho} \left( \dot{\mathbf{H}} \cdot \mathbf{M} + \mathbf{H} \cdot \dot{\mathbf{M}} \right) \quad (4.17)$$

where substitution of Equation (4.15) allows for the solution for  $\dot{s}$  as

$$\dot{s} = \frac{1}{T} \left( -\frac{\partial G}{\partial t} - s\dot{T} - \frac{1}{\rho} \nabla \cdot \mathbf{q} + r^h - \frac{1}{\rho} \left( \dot{\boldsymbol{\sigma}} \cdot \boldsymbol{\epsilon}^{te} \right) - \frac{\mu_0}{\rho} \left( \dot{\mathbf{H}} \cdot \mathbf{M} \right) + \frac{1}{\rho} \left( \dot{\boldsymbol{\sigma}} \cdot \boldsymbol{\epsilon}^r \right) \right). \quad (4.18)$$

Application of the chain rule with respect to the independent variables in the Gibbs free energy yields

$$\frac{\partial G}{\partial t}(T, \boldsymbol{\sigma}, \mathbf{H}, \boldsymbol{\epsilon}^r, x, a) = \frac{\partial G}{\partial T} \dot{T} + \frac{\partial G}{\partial \boldsymbol{\sigma}} \dot{\boldsymbol{\sigma}} + \frac{\partial G}{\partial \mathbf{H}} \dot{\mathbf{H}} + \frac{\partial G}{\partial \boldsymbol{\epsilon}^r} \dot{\boldsymbol{\epsilon}}^r + \frac{\partial G}{\partial x} \dot{x} + \frac{\partial G}{\partial a} \dot{a}. \quad (4.19)$$

which can be substituted into (4.16) to give

$$\begin{aligned}
& -\rho \left( \frac{\partial G}{\partial T} + s \right) \dot{T} - \left( \rho \frac{\partial G}{\partial \boldsymbol{\sigma}} + \boldsymbol{\epsilon}^{te} \right) \cdot \dot{\boldsymbol{\sigma}} - \left( \rho \frac{\partial G}{\partial \mathbf{H}} + \mu_0 \mathbf{M} \right) \cdot \dot{\mathbf{H}} - \\
& \left( \rho \frac{\partial G}{\partial \boldsymbol{\epsilon}^r} - \boldsymbol{\sigma} \right) \cdot \dot{\boldsymbol{\epsilon}}^r - \rho \frac{\partial G}{\partial x} \dot{x} - \rho \frac{\partial G}{\partial a} \dot{a} - \frac{1}{T} \mathbf{q} \cdot \nabla T \geq 0 \quad (4.20)
\end{aligned}$$

which is known as the Claussius Duhem relation. Since the rate terms in (4.20) are not constrained in the Gibbs equation and hence are unbounded, in order for the the Claussius Duhem inequality to hold for the general case the coefficients of  $\dot{T}$ ,  $\dot{\boldsymbol{\sigma}}$ , and  $\dot{\mathbf{H}}$  must be set to zero. Thus,

$$s = -\frac{\partial G}{\partial T} \quad \boldsymbol{\epsilon}^{te} = -\rho \frac{\partial G}{\partial \boldsymbol{\sigma}} \quad \mu_0 \mathbf{M} = -\rho \frac{\partial G}{\partial \mathbf{H}}. \quad (4.21)$$

In addition, accepting the isothermal assumption eliminates the terms dependent on the gradient of temperature and since the magnetic field is large those dependent on the volume fraction of magnetic domains can also be ignored. Thus, Equation (4.20) reduces to

$$\boldsymbol{\sigma}_{eff} \cdot \dot{\boldsymbol{\epsilon}}^r - \rho \frac{\partial G}{\partial x} \dot{x} \geq 0 \quad (4.22)$$

where  $\boldsymbol{\sigma}_{eff} = \boldsymbol{\sigma} - \rho \frac{\partial G}{\partial \boldsymbol{\epsilon}^r}$ . The reorientation strain rate  $\dot{\boldsymbol{\epsilon}}^r$  is geometrically related to the rate of volume fraction change by way of a transformation matrix,  $\Lambda^r$ , such that

$$\dot{\boldsymbol{\epsilon}}^r = \Lambda^r \dot{x}. \quad (4.23)$$

Thus,

$$\left( \boldsymbol{\sigma}_{eff} \cdot \Lambda^r - \rho \frac{\partial G}{\partial x} \right) \dot{x} \geq 0 \quad (4.24)$$

from which it is evident that  $Y^x$ , the driving stress complementary to the twin variant volume fraction, is given by

$$Y^x = \boldsymbol{\sigma}_{eff} \cdot \Lambda^r - \rho \frac{\partial G}{\partial x}. \quad (4.25)$$

## 4.4 Volume Fraction Model Development

An examination of the form of Equation (4.14) indicates that the Gibbs energy is not dependent on the reorientation strain explicitly. Thus, the effective stress in Equation (4.25) is identical to the applied stress  $\sigma_y$  which is purely in the  $\hat{e}_y$  direction. In addition, the geometry of the system dictates that the component of  $\Lambda^r$  that is also in the  $\hat{e}_y$  direction is the saturation strain  $\epsilon_s$ . Thus,

$$\pi^x = \epsilon_s \sigma_y - \rho \frac{\partial G}{\partial x} \quad (4.26)$$

where  $\pi^x = \pm Y^x$  is the condition for the onset of twin variant motion. Differentiation of (4.14) and substitution into (4.26) yields the force balance

$$\pm Y^x = \epsilon_s \sigma_y - \frac{1}{2} \Delta S_{yy} \sigma_y^2 - \mu_0 M_s H_y - \rho \begin{cases} c_1 + 2k_1 x \\ c_2 + 2k_2 x \end{cases} \quad (4.27)$$

for the respective cases  $\{\dot{x} > 0\}$  and  $\{\dot{x} < 0\}$ . Expression (4.27) can then be solved for the volume fraction,

$$x = \begin{cases} A_1(\epsilon_s \sigma_y + \frac{1}{2} \Delta S_{yy} \sigma_y^2 + \mu_0 M_s H_y - \rho c_1 - Y^x) & \dot{x} > 0 \\ A_2(\epsilon_s \sigma_y + \frac{1}{2} \Delta S_{yy} \sigma_y^2 + \mu_0 M_s H_y - \rho c_2 + Y^x) & \dot{x} < 0 \end{cases} \quad (4.28)$$

which is dependent on the applied field  $H_y$  and axial stress  $\sigma_y$ . Here,  $A_1 = 1/(2\rho k_1)$  and  $A_2 = 1/(2\rho k_2)$ . To facilitate the implementation, expression (4.28) is rewritten as

$$x = \begin{cases} A_1(\epsilon_s \sigma_y + \frac{\Delta S_{yy} \sigma_y^2}{2} + \mu_0 M_s H_y - \rho c_1 - Y^x) \\ x_s \\ A_2(\epsilon_s \sigma_y + \frac{\Delta S_{yy} \sigma_y^2}{2} + \mu_0 M_s H_y - \rho c_2 + Y^x) \end{cases} \quad (4.29)$$

for the respective cases  $\{\dot{H} > 0 \text{ and } x < x_s\}$ ,  $\{x > x_s\}$  and  $\{\dot{H} < 0 \text{ and } x < x_s\}$ .

The strain is related to the volume fraction by

$$\epsilon = x \epsilon_{th}, \quad (4.30)$$

with  $\epsilon_{th}$  the maximum theoretical strain which would occur if a single boundary swept through the entire material, thus producing a change in  $x$  from 0 to 1. Parameters that need to be identified in this model include  $k_1$ ,  $k_2$ ,  $\epsilon_s$ ,  $\Delta S_{yy}$ ,  $M_s$ ,  $c_1$ ,  $c_2$ , and  $Y^x$ .

## 4.5 Hysteresis Kernel Model

As is detailed in [19] the model (4.29)-(4.30) yields an idealized hysteresis kernel. The necessary parameters can be identified as characteristic physical properties of the material or phenomenologically by superimposing a theoretical kernel on experimental data. Parameters  $\Delta S_{yy}$ ,  $M_s$ , and  $Y^x$  can be measured directly from experiments. For example,  $M_s$  is found from the magnetization vs field curve shown in Figure 3.9 which is reproduced in Figure 4.3 for ease of reference. Figure 4.4 which reproduces Figure 3.8 shows the maximum reversible strain possible from the  $\text{Ni}_{50}\text{Mn}_{28.7}\text{Ga}_{21.3}$  sample under various applied loads. This data was originally fit with the expression

$$\epsilon_s = \epsilon_{s,0} \left( \left( \frac{\sigma_y}{\sigma_b} \right)^2 - 2 \left( \frac{\sigma_y}{\sigma_b} \right) + 1 \right) \quad (4.31)$$

where  $\sigma_b$  is the blocking stress above which very little change occurs in the strain, and  $\epsilon_{s,0}$  is the strain possible from an unloaded sample. However, because of the sharp decay seen in Figure 4.4 it was found that better accuracy was achieved through the use of a cubic spline fit to the data.

The remaining parameters can be found phenomenologically by fitting the desired shape of the hysteresis loop to data for a particular applied stress ( $\sigma_p$ ) as shown in Figure 4.5. The three points indicated in the figure yield the following data points (1) field  $H_1$  at the strain turn around point, (2) strain  $\epsilon_2$  at the cross over point, (3) field  $H_3$  at the onset of saturation, and (4) saturation strain  $\epsilon_s$ . Using these

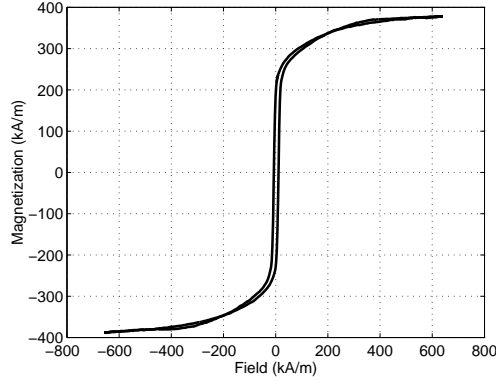


Figure 4.3: Magnetization vs field curve for  $\text{Ni}_{50}\text{Mn}_{28.7}\text{Ga}_{21.3}$ . [51]

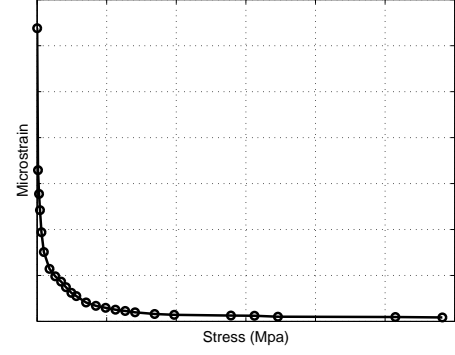


Figure 4.4: Maximum strain per input axial stress for  $\text{Ni}_{50}\text{Mn}_{28.7}\text{Ga}_{21.3}$ . [51]

measurements the expressions in Table 4.1 can be used to calculate the parameters needed to implement Equation (4.28).

$$\begin{aligned}
 \epsilon &= x\epsilon_{th} \\
 k_1 &= nk_2 \\
 k_2 &= \frac{\mu_0 M_s H_3(\sigma_p)\epsilon_{th}}{2(\epsilon_s(\sigma_p) - \epsilon_2(\sigma_p))} \\
 c_1 &= \epsilon_s(\sigma_p)\sigma_p + \frac{1}{2}\Delta S_{yy}\sigma_p^2 + \mu_0 M_s H_1(\sigma_p) - Y^x(\sigma_p) \\
 c_2 &= \epsilon_s(\sigma_p)\sigma_p + \frac{1}{2}\Delta S_{yy}\sigma_p^2 + Y^x(\sigma_p) - 2k_2 \frac{\epsilon_2(\sigma_p)}{\epsilon_{th}} \\
 \epsilon_{s,0} &= \frac{\epsilon_s(\sigma_p)\sigma_b^2}{(\sigma_p - \sigma_b)^2}
 \end{aligned} \tag{4.32}$$

Table 4.1: Parameters in terms of measured data.

Note that strain  $\epsilon$  is related to the volume fraction change  $x$  through the first equation in Table 4.1. The maximum theoretical strain for the sample,  $\epsilon_{th} = 6\%$ , occurs if a single twin boundary sweeps through the entire sample thus producing a

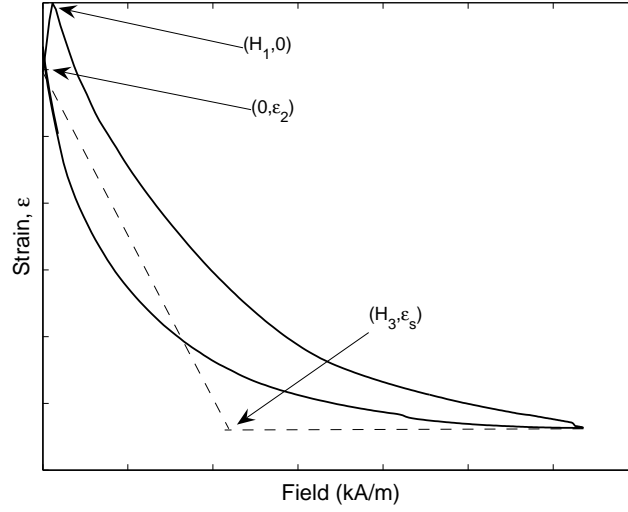


Figure 4.5: Data points for parameter identification.

change in  $x$  from 0 to 1. Hence, for the case where the boundary is pinned in place,  $x$  will be limited to a much smaller range.

Since this is a phenomenological model and the parameters in these equations are fit to data, we now study the accuracy of the model predictions for a given stress level  $\sigma_y$  if the coefficients are calculated based on various stress levels  $\sigma_p$ . To that end, data points were collected for four stress levels as is shown in Table 4.2. Each of these sets of data were used to find the coefficients for Equation (4.29) and predictions were made for the strain output at the other three stress levels.

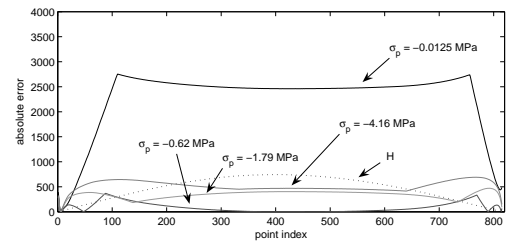
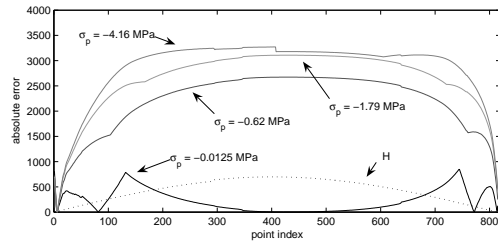
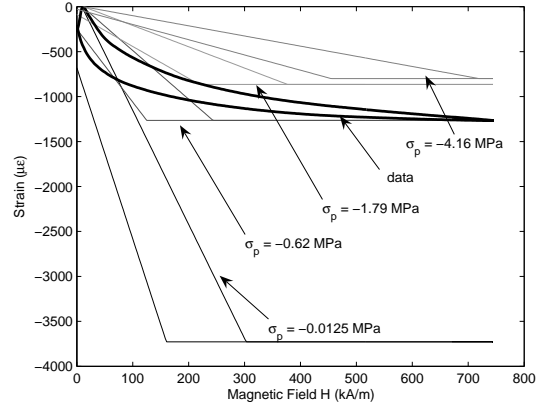
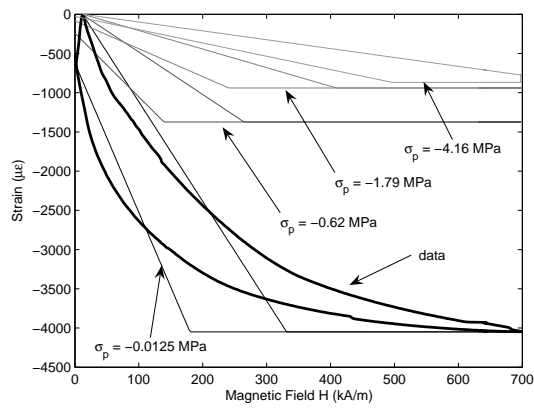
The results are shown in Figure 4.6, where each graph shows the data and four predictions of the strain for a sinusoidal input field at a particular applied stress  $\sigma_y$ . The four predictions are generated based on the the data for various  $\sigma_p$ . Also plotted is the absolute value of the error  $e$  between the predicted and the measured data



	$\sigma_p = -0.0125$ MPa	$\sigma_p = -0.62$ MPa	$\sigma_p = -1.79$ MPa	$\sigma_p = -4.16$ MPa
$\epsilon_s$ ( $\mu\epsilon$ )	-4050	-1265	-730	-455
$H_1$ (kA/m)	12	10	11	10
$\epsilon_2$ ( $\mu\epsilon$ )	-625	-250	-180	-250
$H_3$ (kA/m)	180	125	180	250

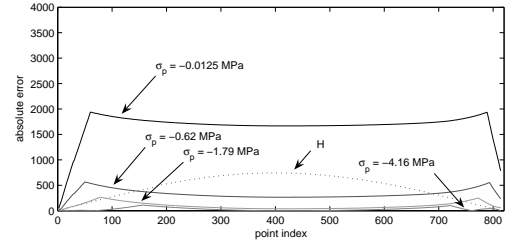
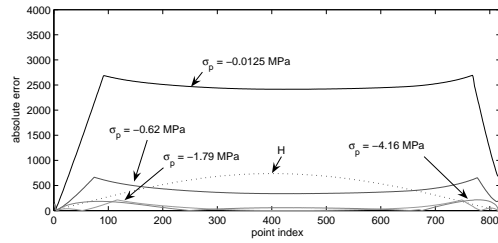
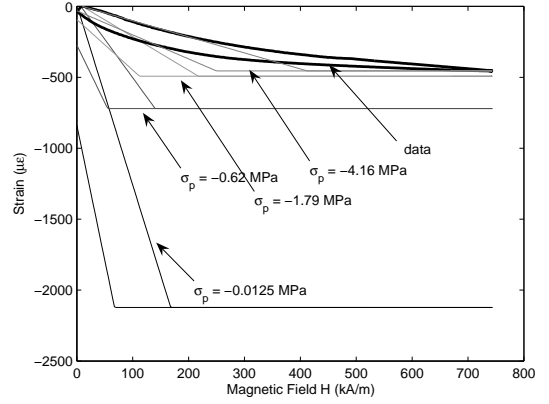
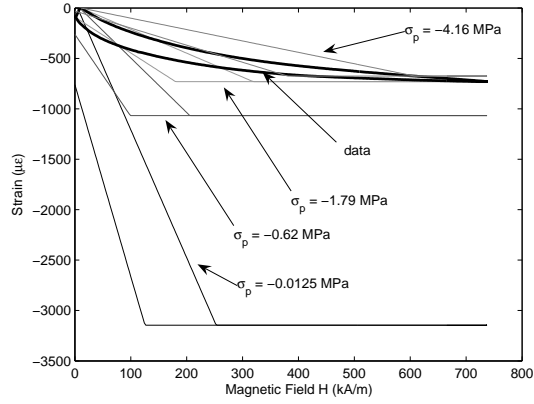
Table 4.2: Model parameters obtained from measurements collected at various stress values.

for each of the cases. The plot in (a) shows the predictions for an applied stress of  $\sigma_y = -0.0125$  MPa which was the smallest possible load experimentally [52]. As is expected, the predicted strain based on coefficients determined from  $\sigma_p = -0.0125$  MPa matches both magnitude and slope. For the coefficients determined from the  $\sigma_p = -0.62$ ,  $\sigma_p = -1.79$ , and  $\sigma_p = -4.16$  MPa data the strain magnitude and slope of the hysteresis kernel are underestimated with a maximum error for the  $\sigma_p = -4.16$  case of about 3100 which corresponds to about a 75% error with respect to the maximum strain output. Panel (b) shows similar plots for the prediction of the strain at  $\sigma_y = -0.62$  MPa. As before, the prediction based on coefficients calculated from the data collected for the same applied load case matches the data closely in both magnitude and slope and predictions based on data for higher loads underestimate both slope and magnitude of the hysteresis kernels. The maximum error for this load is found for the prediction based on the  $\sigma_p = -0.0125$  MPa case and is calculated to be 2800 or about a 220% overestimation with respect to the maximum strain output. The predictions for the  $\sigma_y = -1.79$  and  $\sigma_y = -4.16$  MPa cases are shown respectively in panels (c) and (d). The trends established in (a) and (b) are continued with the  $\sigma_p = \sigma_y$  case matching closely and  $\sigma_p < \sigma_y$  cases underestimating the slopes and



(a)  $\sigma_y = -0.0125$  MPa

(b)  $\sigma_y = -0.62$  MPa



(c)  $\sigma_y = -1.79$  MPa

(d)  $\sigma_y = -4.16$  MPa

Figure 4.6: Predicted strain compared with actual strain for parameters calculated from various data sets.

magnitudes of the kernel while the  $\sigma_p > \sigma_y$  cases overestimate these values. In each case the maximum absolute value of the error was found for the  $\sigma_p = -0.0125$  MPa case and it increases as the difference in stress levels increase being about 380% for  $\sigma_y = -1.79$  MPa and about 440% for  $\sigma_y = -4.16$  MPa.

	Parameter Source Data			
	$\sigma_p = -0.0125 MPa$	$\sigma_p = -0.62 MPa$	$\sigma_p = -1.79 MPa$	$\sigma_p = -4.16 MPa$
$\sigma_y = -0.0125$ MPa	$\Sigma e = 186 \times 10^3$ $\langle e \rangle = 288$ $\max(e) = 849$ $e(H_{max}) = 3$	$\Sigma e = 1779 \times 10^3$ $\langle e \rangle = 2182$ $\max(e) = 2674$ $e(H_{max}) = 2673$	$\Sigma e = 2147 \times 10^3$ $\langle e \rangle = 2634$ $\max(e) = 3109$ $e(H_{max}) = 3107$	$\Sigma e = 2328 \times 10^3$ $\langle e \rangle = 2857$ $\max(e) = 3272$ $e(H_{max}) = 3179$
$\sigma_y = -0.62$ MPa	$\Sigma e = 1849 \times 10^3$ $\langle e \rangle = 2269$ $\max(e) = 2754$ $e(H_{max}) = 2461$	$\Sigma e = 72 \times 10^3$ $\langle e \rangle = 88$ $\max(e) = 369$ $e(H_{max}) = 2$	$\Sigma e = 278 \times 10^3$ $\langle e \rangle = 341$ $\max(e) = 470$ $e(H_{max}) = 402$	$\Sigma e = 418 \times 10^3$ $\langle e \rangle = 513$ $\max(e) = 691$ $e(H_{max}) = 468$
$\sigma_y = -1.79$ MPa	$\Sigma e = 1873 \times 10^3$ $\langle e \rangle = 2298$ $\max(e) = 2694$ $e(H_{max}) = 2416$	$\Sigma e = 325 \times 10^3$ $\langle e \rangle = 399$ $\max(e) = 664$ $e(H_{max}) = 337$	$\Sigma e = 46 \times 10^3$ $\langle e \rangle = 57$ $\max(e) = 212$ $e(H_{max}) = 0$	$\Sigma e = 64 \times 10^3$ $\langle e \rangle = 78$ $\max(e) = 215$ $e(H_{max}) = 56$
$\sigma_y = -4.16$ MPa	$\Sigma e = 1354 \times 10^3$ $\langle e \rangle = 1664$ $\max(e) = 1938$ $e(H_{max}) = 1667$	$\Sigma e = 269 \times 10^3$ $\langle e \rangle = 331$ $\max(e) = 565$ $e(H_{max}) = 265$	$\Sigma e = 79 \times 10^3$ $\langle e \rangle = 97$ $\max(e) = 264$ $e(H_{max}) = 37$	$\Sigma e = 25 \times 10^3$ $\langle e \rangle = 31$ $\max(e) = 111$ $e(H_{max}) = 0$

Table 4.3: Error comparison for various choices of parameter source data.

The error between the predicted and experimental outputs is quantified by various means in Table 4.3 where  $e$  is the absolute value of the difference between the data and the simulation for each of the 174 data points,  $\Sigma e$  is the sum of these errors,  $\langle e \rangle$  is the average value of the error,  $\max(e)$  is the maximum of the error, and  $e(H_{max})$  is the error at the maximum value of the field. It is observed that the two situations of largest error are (a) predictions based on parameters generated from the 0.0125 MPa data and (b) predictions for the output for the sample under 0.0125 MPa load

based on parameters calculated from other data sets. As the stress levels increase, the difference in achievable strains decreases and the error correspondingly decreases. This suggests that stress ranges may need to be defined within which a specific set of parameters are appropriate and that these ranges would be smaller for lower applied stress. It is noted that, as in the model by Kiefer and Lagoudas [39], this model accurately describes the overall trend of strain output decrease with increased load.

## 4.6 Stochastic Homogenization

Relation (4.29) provides a model for the strain generated by single crystal Ni-Mn-Ga with its twin boundaries partially restrained by pinning sites, exposed to collinear magnetic fields and external stresses. A review of the limitations of the model and a sensitivity analysis relating model accuracy with parameter selection that were discussed by Faidley et al [19] were presented in the previous section. The most critical sources of error in this model include:

- (i) The sample is assumed to consist of only two variants with a single boundary. In reality, however, Ni-Mn-Ga has many twin variants though only two distinct orientations. This implies that a sample will have numerous twin boundaries and thus numerous pinning sites.
- (ii) The pinning sites are assumed to be homogeneously distributed throughout the material and every pinning site has the same energy. As discussed by Marioni [56], in a physical material the pinning energies vary over a large range which translates into a variation of the slopes  $k_1$  and  $k_2$ . The energy of each site depends on the size of the imperfection and whether the site originates from dislocations, microstructural defects, retained austenite or other factors.

Furthermore, the strength of each site may depend on the direction of motion of the twin boundary, effectively providing a source of anisotropy.

(iii) The field is assumed to be uniform throughout the sample. However, due to short-range interactions the magnetic field in Ni-Mn-Ga can be considered to behave locally in a fashion similar to the Weiss mean field [29]. Thus, the magnitude of the field at a given point in the material is not equal to the applied field but rather, is given by an effective field which is dependent on the applied field and the magnetization,  $H_e = H + H_i = H + \alpha M$ . The mean field constant  $\alpha$  varies from point to point in the material due to differences in the lattice structure.

Limiting factors (i)-(iii) are addressed in this dissertation by considering stochastic homogenization in the sense of Smith [79]. By way of introduction to this technique, Section 4.6.1 presents a review of Smith's derivation for magnetostrictive Terfenol-D [78, 16]. Section 4.6.2 then presents the application of this method to the kernel model in (4.29)-(4.30).

#### **4.6.1 Stochastic Homogenization Method for Magnetostrictive Materials**

This approach has proven effective in the modeling of polarization hysteresis in the presence of thermal activation and stresses in ferroelectric materials, ferromagnetic materials, and shape memory alloys. Special features of the model include its ability to address reversible and irreversible behaviors, biased and unbiased minor loop regimes including accommodation effects, and relaxation phenomena [82, 83]. The effects of polycrystallinity, material nonhomogeneities, inclusions, textures and variable

interaction fields are incorporated in the Smith model for ferromagnetic materials by assuming that the local coercive field  $H_c$  and interaction field  $H_i$  are stochastically distributed with respective densities  $\nu_1$  and  $\nu_2$  that are chosen to satisfy specific decay criteria. The resulting macroscopic magnetization model is given by

$$M(H) = \int_0^\infty \int_{-\infty}^\infty \nu_1(H_c) \nu_2(H_i) [\overline{M}(H + H_i; H_c, x)](t) dH_i dH_c, \quad (4.33)$$

where the local average magnetization or kernel  $\overline{M}$  quantifies the hysteresis at the lattice level and yields macroscopic models only for homogeneous materials with negligible interaction fields. In the absence of thermal activation,  $\overline{M}$  has the form (employing Preisach notation)

$$[\overline{M}(H; H_c, x)](t) = \begin{cases} [\overline{M}(H; H_c, x)](0) & \\ \frac{\mu_0}{\eta} H - M_R & \\ \frac{\mu_0}{\eta} H + M_R & \end{cases} \quad (4.34)$$

for the respective cases  $\{\tau(t) = \emptyset\}$ ,  $\{\tau(t) \neq \emptyset \text{ and } H(\max \tau(t)) = -H_c\}$ ,  $\{\tau(t) \neq \emptyset \text{ and } H(\max \tau(t)) = H_c\}$ . In this expression,

$$H_c = \frac{\eta}{\mu_0} (M_R - M_I) \quad (4.35)$$

denotes the coercive field and

$$\tau(t) = \{t \in (0, t_f] | H(t) = -H_c \text{ or } H(t) = H_c\} \quad (4.36)$$

denotes transition points. The initial moment orientation has the form

$$[\overline{M}(H; H_c, x)](0) = \begin{cases} \frac{\mu_0}{\eta} - M_R & H(0) \leq -H_c \\ x & -H_c \leq H(0) \leq H_c \\ \frac{\mu_0}{\eta} H + M_R & H(0) \geq H_c \end{cases} . \quad (4.37)$$

The local magnetization,  $\overline{M}$ , given by (4.34) is shown versus magnetic field in Figure 4.7; comparison between macroscopic magnetization results given by (4.33) and experimental data is shown in Figure 4.8.

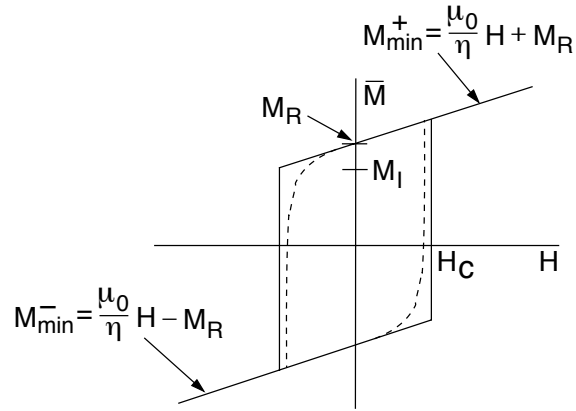


Figure 4.7: Local magnetization  $\bar{M}$  given by expression (4.34). [79]

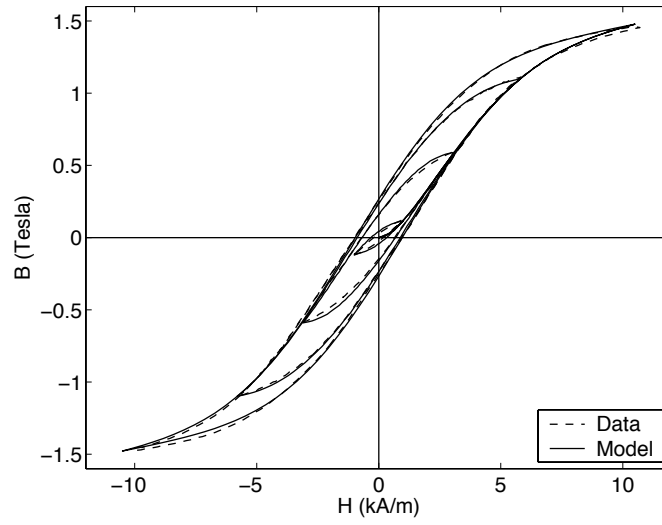


Figure 4.8: Comparison of steel data with model results obtained from Equation (4.33). [79]

As detailed in [79], model Equations (4.33)-(4.34) can be interpreted as providing an energy basis for certain extended Preisach models, with the kernel,  $\overline{M}$ , derived through thermodynamic considerations providing the Preisach hysterons and the stochastic densities providing the Preisach weights. However, the similarities between the Smith model and the Preisach model are formal rather than conceptual, for several crucial differences between the two formulations can be established. First, the Smith model is posed through thermodynamic arguments constructed at the lattice level involving parameters that can be physically correlated with properties of the experimental measurements. Due to its thermodynamic origin, in the Smith model stress and temperature dependencies are incorporated in the kernel rather than the weights as is the case with the Preisach model. The model automatically incorporates these effects without the need for vector-valued weights. This implies that only one set of parameters needs to be identified and no switching between parameter sets is required during real-time operation of the model, thus significantly improving the computational speed relative to the Preisach model.

#### **4.6.2 Stochastic Homogenization Method Applied to Ni-Mn-Ga in the Collinear Stress-Field Configuration**

The strain model for ferromagnetic shape memory materials presented in this dissertation builds on the Smith model for hysteresis of ferroic materials but differs from it in the following aspects:

- Kernel (4.29), which characterizes the martensitic volume fraction, was developed by considering the reorientation of twin variants in martensitic structures and therefore reflects energy functionals which are different from those found in polarization models. While certain commonality can be established between



the proposed model and previous polarization models - e.g., in regard to double-well energy potentials - the difference between kernels is rooted in the physical differences between ferromagnetic shape memory and magnetostriction, which were outlined by O’Handley [69].

- In this paper the stochastic homogenization is performed relative to the interaction field  $H_i$  and the pinning energy  $k_2$ . This implies that suitable distributions to accommodate these effects can potentially be different than those employed for interaction and coercive fields in [82]. Notwithstanding, for the sake of simplicity, in this paper we attempt to exploit certain commonalities between the phenomenological behaviors observed in both models. Namely, for the interaction field we consider a normal distribution centered at  $H_i = 0$ , as in the Smith model, and for the pinning sites we consider a log-normal distribution similar to that employed by Smith for coercive fields.

The model thus has the form

$$[x(H, \sigma)](t) = \int_0^\infty \int_{-\infty}^\infty \nu_1(H_i) \nu_2(k_2) [\bar{x}(H + H_i; \sigma, k_2)](t) dH_i dk_2 \quad (4.38)$$

where  $\nu_1$  and  $\nu_2$  are appropriately chosen distributions and  $\bar{x}$  is given by expression (4.29). Since the Weiss interaction field is known to have both positive and negative values, one possible distribution is

$$\nu_1(H_i) = c_1 e^{-H_i^2/(2b^2)} \quad (4.39)$$

which is a normal distribution centered at  $H_i = 0$ , as shown in Figure 4.9(a). The pinning site energies were incorporated into the energy equations as effective mechanical springs. Thus, the values for  $k_2$  will never be negative. To meet this criterion

the distribution over  $k_2$  is chosen to be log-normal, as shown in Figure 4.9(b), and is given by

$$\nu_2(k_2) = c_2 e^{-\left(\ln(k_2/\bar{k}_2)/2c\right)^2}. \quad (4.40)$$

The effect of this distribution on the slopes of the hysteresis kernels is shown in Figure 4.9(c).

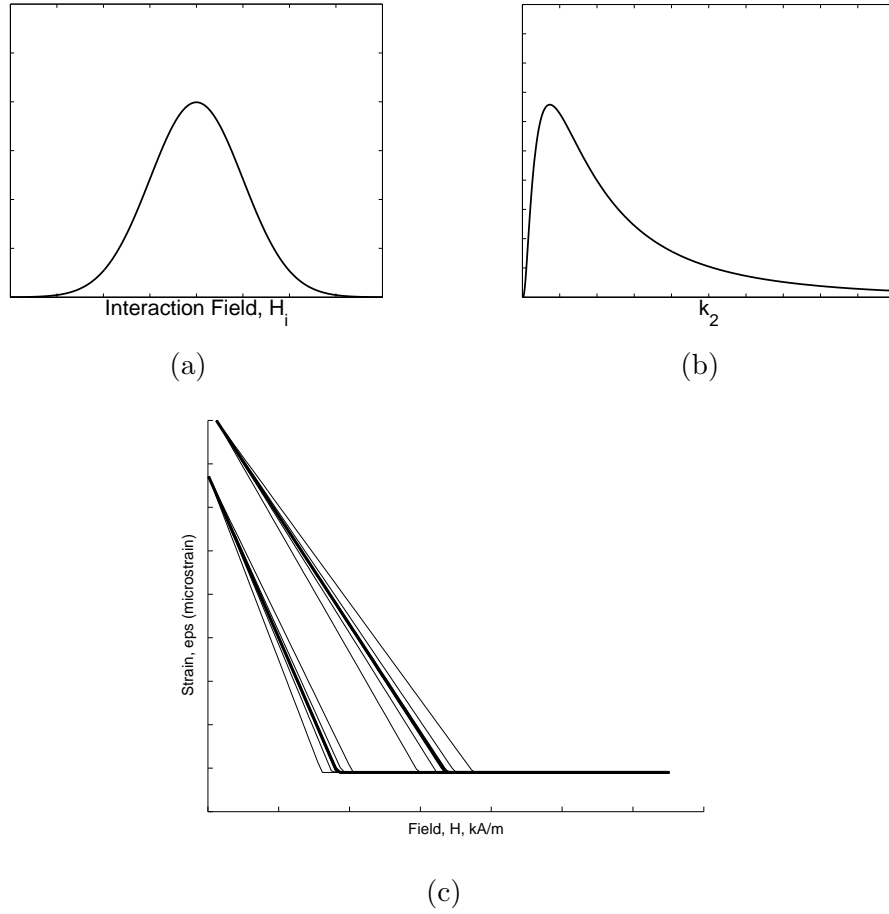


Figure 4.9: Distributions for (a) interaction field  $H_i$ , (b) pinning site strength  $k_2$ . (c) effect of the  $k_2$  distribution on the hysteresis kernels.

## 4.7 Model Implementation

The homogenized strain model given by relation (4.38) was implemented using MATLAB. The integration was performed using a composite Gaussian quadrature routine and the distribution parameters were found using a constrained optimization routine. Simulations indicated that the model needed to be modified to avoid inclusion of kernels in a non-physical range. The details of this implementation are discussed in the following sections.

### 4.7.1 Coding

The code necessary to implement the stochastic homogenization model for Ni-Mn-Ga is included in Appendix B. The initial section of the code is concerned with identifying the necessary parameters. Section 4.7.2 presents this in great detail so any mention of it will be postponed till that section. In the second section of the code, the Gaussian Quadrature routine that is used to calculate integral (4.38) is set up. Gaussian quadrature approximates an integral with a summation of the form

$$\int_{-1}^1 f(x)dx = \sum_{i=0}^n w_i f(z_i) \quad (4.41)$$

where  $w_i$  and  $z_i$  are appropriate weights and evaluation points which are tabulated in the literature [7, 12]. The power of this numerical integration method is that through the use of non-evenly spaced points and appropriate weights accurate approximations can be made with very few calculations. For example, the value of  $\sin(t)$  can be approximated to within  $1 \times 10^{-16}$  with the use of only 4 points. Several modifications to the standard Gaussian quadrature method are made in the implementation of this model. Firstly, a composite approach is taken in which the overall interval is divided

into twenty six smaller intervals in which the 4-point quadrature is applied. Secondly, since the intervals do not range from 0 to 1 as in Equation (4.41) the expression needs to be scaled appropriately as in [7]

$$\int_a^b f(x)dx = \frac{(b-a)}{2} \sum_{i=0}^n w_i f\left(\frac{z_i(b-a) + (b+a)}{2}\right). \quad (4.42)$$

Finally, since Equation (4.38) is a double integral the gaussian quadrature definition needs to be extended to incorporate both variables resulting in

$$\begin{aligned} [x(H, \sigma)](t) &= \int_0^\infty \int_{-\infty}^\infty \nu_1(H_i) \nu_2(k_2) [\bar{x}(H + H_i; \sigma, k_2)](t) dH_i dk_2 \\ &= \int_{k_{2,min}}^{k_{2,max}} \int_{-H_{i,max}}^{H_{i,max}} \nu_1(H_i) \nu_2(k_2) [\bar{x}(H + H_i; \sigma, k_2)](t) dH_i dk_2 \\ &= \sum_{i=1}^{26 \times 4} \sum_{j=1}^{26 \times 4} W_1(h_i) W_2(k_j) [\bar{x}(H + h_i; \sigma, k_j)](t) \end{aligned} \quad (4.43)$$

where  $h_i$  are the evaluation points for the distribution on  $H_i$ ,  $k_j$  are the evaluation points for the distribution on  $k_2$  and  $W_1$  and  $W_2$  are the respective weighted distributions at each point. By making use of the matrix operations that are MatLab's primary strength, the evaluation points can be written as a 2 dimensional matrix with  $k_2$  intervals in the x direction and  $H_i$  intervals in the y direction. Using this technique the double integral in (4.43) can be written as a single line of code as:

$$\text{Int}(s5) = W1 * (\text{xi\_bar\_v}(H(s5-1), H(s5), x2, x1, \text{sigma}, \text{eps\_s}, n, K) . * \text{gk}) * W2,$$

which limits the need for any loops other than the time loop and substantially decreases the runtime of the code.

The function *xi\_bar\_v.m* which is called in the code exert above refers to a function which evaluates Equation (4.29). Using boolean arithmetic this can be done very simply as

```

xi1 = (slope>=0).*(1./(2.*rho.*k1_m).*(eps_s*sigma+.5*S*sigma^2+mu_0.*Ms.*Hy_m-rho*c1-Y + K.*Hy_m)) ...
      + (slope<0).*(1./(2.*rho.*k2_m).*(eps_s*sigma+.5*S*sigma^2+mu_0.*Ms.*Hy_m-rho.*c2_m+Y + K.*Hy_m));

xi = (xi1<xi_s).*xi1 + (xi1>xi_s).*xi_s;

```

The final step of the code is the output stage. The simulated values of strain are plotted and output to other routines including *errors.m* and *con\_opt.m* where they are used to calculate error and to update the parameter optimization routine.

## 4.7.2 Parameter Determination

The various parameters necessary in the Matlab implementation discussed in the previous section can be divided into three categories: (a) kernel parameters, (b) material properties, and (c) distribution parameters. The identification of the kernel parameters according to Figure 4.5 and the expressions in Table 4.1 was discussed in Section 4.5. Quantities  $H_1$  and  $\epsilon_s$  are identified from the strain-field data for various loading conditions and splines are used to fit the data. Then  $c_1$  and  $c_2$  can be calculated.

Material properties can generally be measured directly from experiments. The saturation magnetization ( $M_s$ ) can be measured using the pick-up coil as described in Section 3.2.3. This was done by Malla and identified as 622 kA/m. As discussed in section 3.3.2, Malla also measured the saturation strain ( $\epsilon_s$ ) under various loading conditions. This data is fit using cubic splines to increase the accuracy of the output simulations especially at low stress levels where there are large changes in output strain with small increase in loads. Following assumptions made by Kiefer [39] the difference between the compliance of the two variants ( $\Delta S_{yy}$ ) is minimal and can be ignored, the density is incorporated into unknown coefficients and is thus set to 1, and the force density necessary to provided the onset of variant reorientation ( $Y^x$ )

Permeability of free space	$\mu_0 = 1.256 \times 10^{-6} \text{ N/A}^2$
Saturation magnetization	$M_s = 622000 \text{ A/m}$
Theoretical maximum strain	$\epsilon_{th} = -60000 \times 10^{-6}$
Change in mechanical compliance	$\Delta S_{yy} = 0$
Density	$\rho = 1$
Onset of variant reorientation[39]	$Y^x = 209570 \text{ Nm/m}^3$
Saturation strain	$\epsilon_s(\sigma_p) = \text{polynomial fit to data}$
Cell reorientation energy, variant 1	$c_1 = \epsilon_s(\sigma_p)\sigma_p + \frac{1}{2}\Delta S_{yy}\sigma_p^2 + \mu_0 M_s H_1 - Y^x \text{ Nm/m}^3$
Cell reorientation energy, variant 2	$c_2 = \epsilon_s(\sigma_p)\sigma_p + \frac{1}{2}\Delta S_{yy}\sigma_p^2 + Y^x - 2k_2 \frac{\epsilon_2(\sigma_p)}{\epsilon_{th}} \text{ Nm/m}^3$
	$\epsilon_2(\sigma_p) = \text{polynomial fit to data}$
	$H_1 = 10750 \text{ A/m}$

Table 4.4: Values for model coefficients.

is measured as  $209570 \text{ Nm/m}^3$  [39]. Finally, the theoretical maximum strain of 6% is calculated based on the sample's crystallography [76]. Table 4.4 shows the values determined for the various parameters.

The remaining four key parameters are distribution parameters  $\bar{k}_2$ ,  $\bar{b}$ , and  $c$  and kernel parameter  $n$  that are determined through constrained optimization to minimize the total difference between the time trace strain data and the output of the model for each of the loading conditions using MatLab's constrained optimization routine.

### 4.7.3 Distribution Truncation

The simulated field-strain curve is compared to data for the  $\sigma = -0.0125 \text{ MPa}$  loading condition in Figure 4.10 (a). The infinite integrals were originally approximated as truncated integrals over the range in which the magnitude of the distributions was within 99% of its maximum. The simulated curve shows a non-physical blocky tip due to the inclusion of kernels that fall into non-physical ranges of  $k_1$  and  $H_i$ . Figure 4.11 shows an example of a standard kernel given by relation (4.29). In the range of parameters where a large  $k_1$  is combined with a large  $H_i$  non-physical

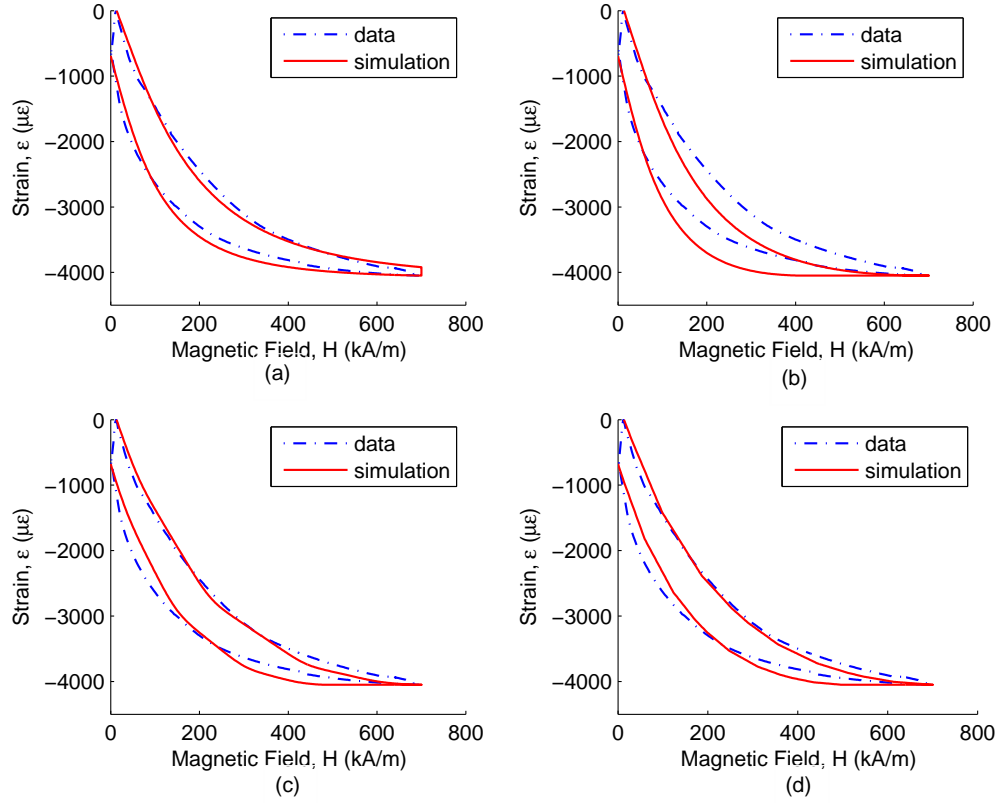


Figure 4.10: Comparison of model results and experimental data for the  $\sigma = -0.0125$  MPa loading condition using various implementation methods: (a) using full distribution, (b) using method (i), (c) using method (ii), and (d) using method (iii).

kernels with a discontinuity at the maximum field will result. The inclusion of these kernels in the integral (4.29) will result in the non-physical result shown in Figure 4.10 (a). Three methods are proposed to address this problem:

1. Use the parameters already found through constrained optimization using the full distributions but ignore all the non-physical kernels.

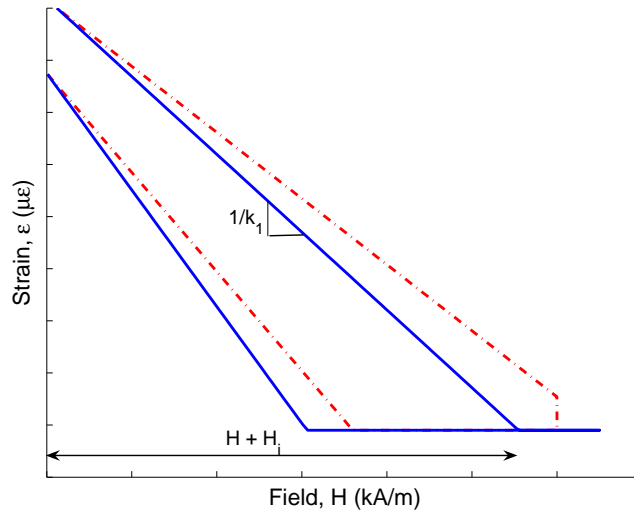


Figure 4.11: Hysteresis kernels produced by relation (4.29) showing both physical and non-physical behaviors.

2. Find new parameters using constrained optimization while truncating the distributions to ignore all the non-physical kernels.
3. Find new parameters using constrained optimization in which the shape of the distributions is controlled such that  $p\%$  of the kernels are required to be physical.

The results of these three methods for the  $\sigma = -0.0125$  MPa loading condition are shown in Figure 4.10 (b) - (d) and the errors are quantified in Table 4.5. All three successfully eliminated the non-physical discontinuity at maximum field. As was expected the error is greatest for the first method where the non-physical kernels are ignored without recalculating the parameters. The lowest error is achieved using



method (3) in which the constrained optimization routine includes the inequality

$$\frac{1}{2\rho k_{1,max}} \left( \epsilon_s \sigma_y + \frac{1}{2} \Delta S_{yy} \sigma_y^2 + \mu_0 M_s (H_{max} - H_{i,max}) - \rho c_1 - Y^x \right) \geq p \frac{\epsilon_s}{\epsilon_{th}} \quad (4.44)$$

that is derived from expression (4.29) and places limits on the distribution coefficients and therefore the shape of the distributions. Parameter  $p$  is introduced to control the percentage of the kernels that are allowed to be non-physical and thus controls the range of allowable distribution shapes and how much of each distribution is truncated. The maximum values for  $k_1$  and  $H_i$  are found from expression (4.39) and (4.40),

$$H_{i,max} = \sqrt{-2(\bar{b})^2 \ln(.01)} \quad (4.45)$$

$$k_{1,max} = n \bar{k}_2 e^{2c \sqrt{-\ln(.01)}}. \quad (4.46)$$

Testing shows that  $p = 0.1$  achieves a suitable balance between allowable shape of the distributions and the truncation of those distributions that best minimizes the error. An example of the truncated distributions that result from this kernel reduction scheme are shown in Figure 4.12. Method (3) with  $p = 0.1$  is used in the following section to study the error for all four loading conditions.

	Original	Method (i)	Method (ii)	Method (iii) w/ p = 0.1
$\Sigma e$	42,382	130,000	71,818	69,960
$\langle e \rangle$	52.324	160.64	88.665	86.371
$\langle e \rangle / \epsilon_s (\%)$	1.3	3.9	2.2	2.1
max(e)	334.15	447.56	361.75	379.94

Table 4.5: Error associated with each of the methods used to eliminate the discontinuity at maximum field.

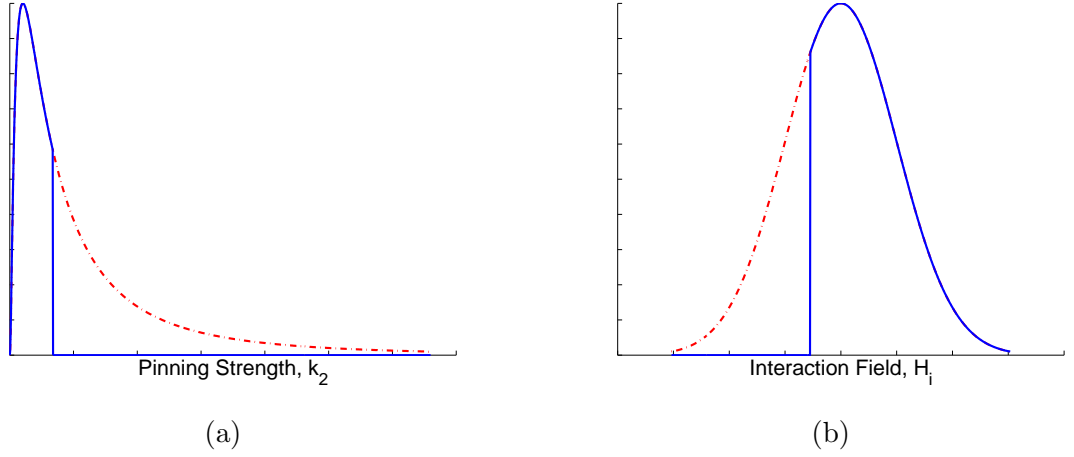


Figure 4.12: Truncated distributions for (a) pinning site strength  $k_2$  and (b) interaction field  $H_i$ .

## 4.8 Model Results and Error Analysis

Constrained optimization was used to determine the parameters for each of the four loading cases based on the minimization of the total sum of the error between the modeled and measured time traces of the strain. These parameters, shown in Table 4.6, were found to be within 10% of those necessary to minimize the mean error in all but two cases. A comparison of the data and the model for each of these loading cases is shown in Figure 4.13 where it is observed that the simulation closely predicts the data in all cases.

The last column in Table 4.6 represents the set of parameters found by minimization of the sum of the error across all four loading cases. The comparison between the data and the model results generated with these parameters is shown in Figure 4.14. Even though these simulations are generated from parameters optimized for overall

	$\sigma = -0.0125 \text{ MPa}$	$\sigma = -0.13 \text{ MPa}$	$\sigma = -0.27 \text{ MPa}$	$\sigma = -0.41 \text{ MPa}$	Overall Optimal
$n$	1.165	1.1417	1.0894	1.0287	1.1207
$\bar{k}$	$1.0306 \times 10^6$	$0.70091 \times 10^6$	$0.87182 \times 10^6$	$1.3363 \times 10^6$	$0.75325 \times 10^6$
$c$	0.80761	1	1	0.99856	0.99901
$\bar{b}$	$0.010001 \times 10^4$	$0.012166 \times 10^4$	$0.01 \times 10^4$	$0.01 \times 10^4$	$0.010304 \times 10^4$

Table 4.6: Constrained optimization results for parameters under various loads.

reduction of error, the predictions are remarkably similar to those obtained using parameters optimized for individual cases as in Figure 4.13. This is an indication that there are multiple minima in the four parameter optimization problem; various sets of parameters may produce similarly low values of the error. Figure 4.14 shows that the optimized parameters allow good correlation with data for the lower three load conditions but the model loses accuracy at the higher load case. This is because the error increase is much steeper for overestimation than for underestimation.

A quantitative look at the error calculations for the constrained optimization for various loading conditions is provided in Table 4.7. The error measurements calculated include the sum of the error that was the basis for the constrained optimization, the mean of the error, the percent error of the mean with respect to the maximum strain, and the maximum error. The error was calculated as the absolute value of the difference between the data and model at each point. The diagonal of Table 4.7 indicates the smallest error for all cases and represents the situation in which the parameters were optimized for the same loading case as was simulated by the model. These situations are those plotted in Figure 4.13. The off diagonal error measurements indicate the error for those situations in which the model parameters were optimized for a load other than the one used in the model. The error is larger below

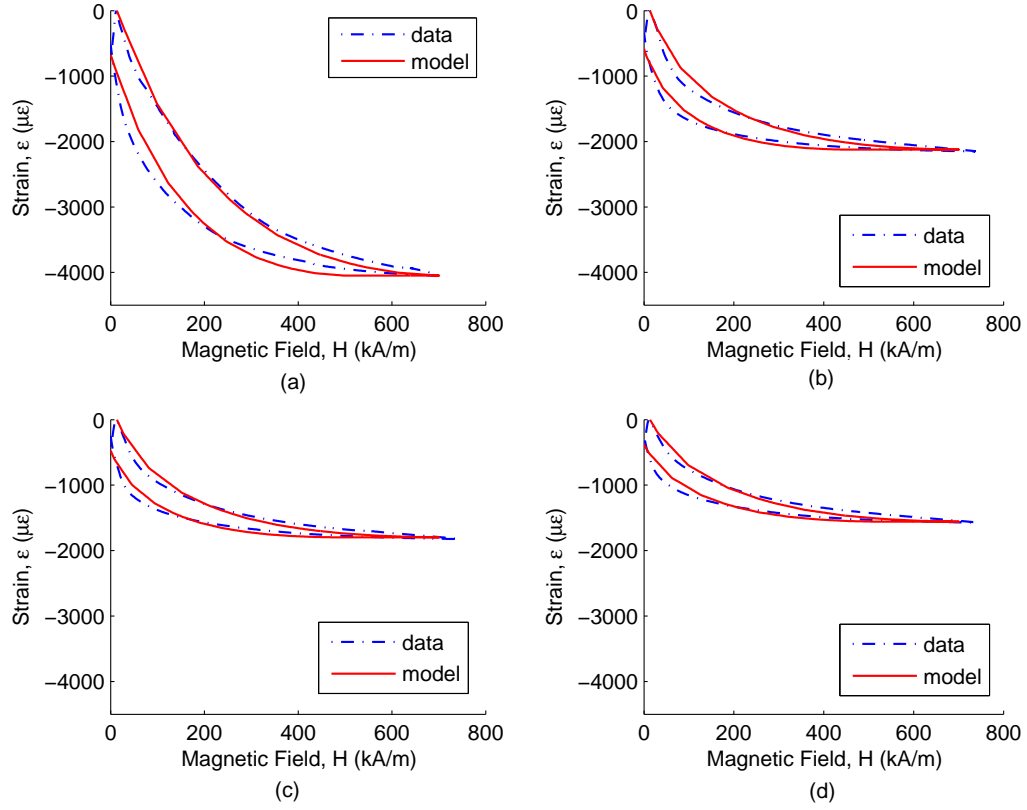


Figure 4.13: Constrained optimization fits to data for various loads: (a)  $\sigma_y = -0.0125$  MPa, (b)  $\sigma_y = -0.13$  MPa, (c)  $\sigma_y = -0.27$  MPa, (d)  $\sigma_y = -0.41$  MPa.

the diagonal where parameters for a higher load are used to simulate a lower load than above the diagonal where the reverse is true.

The rightmost column of Table 4.7 presents the summation of the errors for all four loading conditions for each set of parameters. For all four individually optimized cases the sums of the errors show only an 8% deviation. The bottom row of the table shows the model error when the set of parameters which minimizes the overall error is used. This total is 12.5% lower than the average sum for the individually optimized

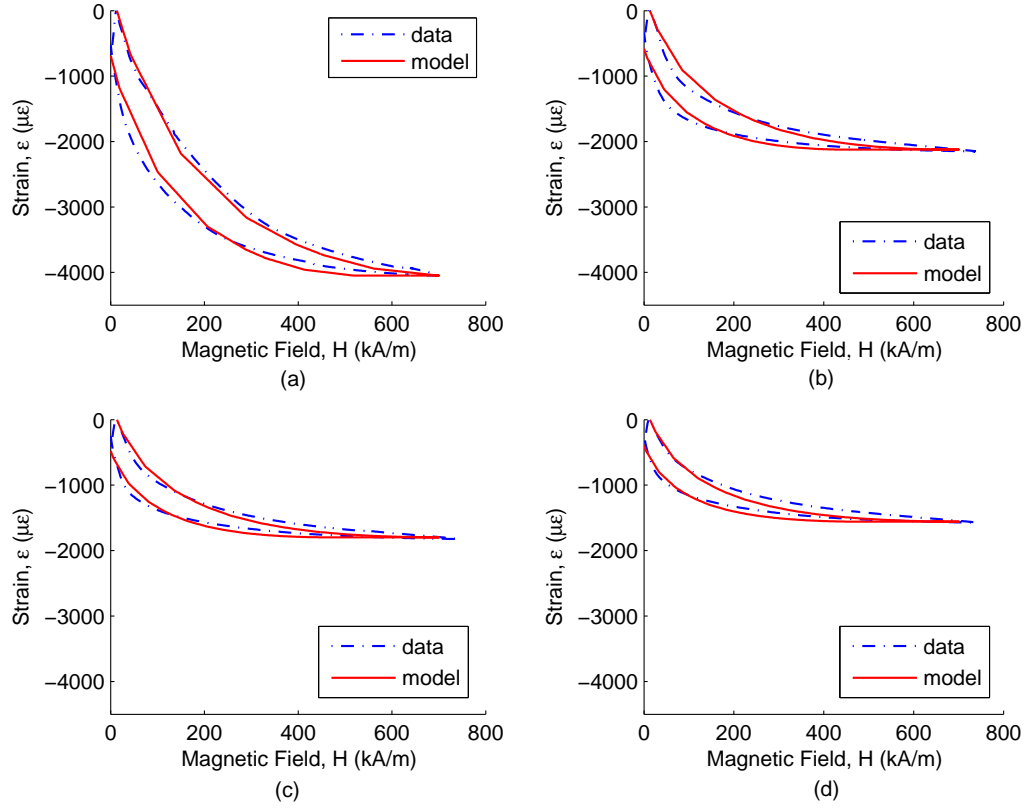


Figure 4.14: Overall optimized simulation of strain compared to data for various loads: (a)  $\sigma_y = -0.0125$  MPa, (b)  $\sigma_y = -0.13$  MPa, (c)  $\sigma_y = -0.27$  MPa, (d)  $\sigma_y = -0.41$  MPa.

cases. In addition, the sum of the error for each loading condition using these overall optimized parameters is within 20% of the minimum sum of the error found for the individually optimized parameters. The maximum is 18% for the  $\sigma_y = -0.41$  MPa loading condition which corresponds to the observation made earlier with regard to the decrease in accuracy of the simulations shown in Figure 4.14 for the higher loading condition. The small differences between the simulations using the four-case-optimization parameters and those using the individually optimized parameters

Parameter Set $\sigma_p$	Loading Conditions, $\sigma_y$				Total
	-0.0125 MPa	-0.13 MPa	-0.27 MPa	-0.41 MPa	
-0.0125 MPa					
$\Sigma e$	69,960	40,393	35,767	37,644	183,764
$\langle e \rangle$	86.371	49.868	44.157	46.474	
$\langle e \rangle / \epsilon_s (\%)$	2.1315	2.3049	2.4111	2.9475	
$\max(e)$	379.94	320.68	222.52	164.08	
-0.13 MPa					
$\Sigma e$	81,910	35,180	31,667	36,508	185,265
$\langle e \rangle$	101.12	43.432	39.095	45.072	
$\langle e \rangle / \epsilon_s (\%)$	2.4957	2.0035	2.1312	2.8564	
$\max(e)$	272.85	319.42	233.88	175.12	
-0.27 MPa					
$\Sigma e$	81,136	39,571	29,586	31,938	182,231
$\langle e \rangle$	101.17	48.853	36.526	39.430	
$\langle e \rangle / \epsilon_s (\%)$	2.4724	2.2569	1.9908	2.4976	
$\max(e)$	344.17	312.7	225.73	225.73	
-0.41 MPa					
$\Sigma e$	83,168	51,065	37,442	26,615	198,290
$\langle e \rangle$	102.68	63.043	46.224	32.858	
$\langle e \rangle / \epsilon_s (\%)$	2.5351	2.9196	2.5252	2.0802	
$\max(e)$	455.00	406.91	251.42	189.65	
Optimized					
$\Sigma e$	64,106	37,297	30,965	31,454	163,822
$\langle e \rangle$	79.143	46.045	38.228	38.832	
$\langle e \rangle / \epsilon_s (\%)$	1.9516	2.1255	2.0838	2.4590	
$\max(e)$	324.36	317.76	231.11	171.67	

Table 4.7: Error comparison for parameters determined for various loading conditions.

highlights the ability of the homogenized model to simulate the strain output of Ni-Mn-Ga for various loading conditions using a single set of parameters. With mean errors of under 3%, this modeling technique shows promise in the design and control of Ni-Mn-Ga solenoid actuators for various applications.

## 4.9 Concluding Remarks

This chapter has presented contributions to the theoretical understanding of the strain mechanism in Ni-Mn-Ga applied in a collinear configuration and to the development and implementation of a model predicting the output strain from Ni-Mn-Ga samples in this configuration. Modifications of the generally accepted strain mechanism have been presented which take into account the inclusions and residual strains present in the material and the effect they have on pinning the twin boundaries. These pinning sites provide an internal restoring force making reversible strain possible and also limiting the maximum strain output possible from the sample. The modified strain mechanism was then described through an energy formulation based on Kiefer and Lagoudas which described an idealized hysteresis kernel for a given loading condition. The physical variation of internal field and pinning site strength was accounted for through the use of stochastic homogenization techniques similar to those used by Smith for other smart materials. The stochastic homogenization model was implemented using MatLab and the accuracy of the resulting predictions were compared for various loading cases and parameter identification methods. It was found that a single set of parameters optimized to minimize the total error across 4 loading conditions can predict the strain output from the sample for each individual loading case to within 3%. This highlights the power of this modeling technique in the future design and control of Ni-Mn-Ga solenoid transducers.

## CHAPTER 5

### CONCLUSIONS

#### 5.1 Contributions to the Field

This dissertation has presented an array of work on the characterization and modeling of Ferromagnetic Shape Memory Ni-Mn-Ga in a collinear stress-field configuration. Since early testing of Ni-Mn-Ga concluded that the orthogonal stress-field configuration was capable of a larger strain of up to 10% the focus of most of the literature has been on the perpendicular configuration. Though the reversible strains achievable by the sample of  $\text{Ni}_{50}\text{Mn}_{28.7}\text{Ga}_{21.3}$  studied in this work are substantially smaller at -0.41% they are still more than three times the strain possible from magnetostrictive materials which are employed in transducers similar to those used in this study.

The major attraction to the collinear stress-field configuration is that this allows Ni-Mn-Ga to be employed in solenoid transducers like that show in Figure 1.1. These transducers enclose the sample in a closed magnetic circuit eliminating flux leakage and demagnetization effects. The solenoid transducer technology, which involves a driving coil wrapped around the Ni-Mn-Ga sample, also promises smaller volume and lighter weight transducers than the electromagnet transducers that are necessary for



the orthogonal stress-field configuration. Solenoid transducers are also generally more efficient and can achieve higher frequencies than their electromagnet counterparts because of lowered eddy current losses.

Prior to work begun at OSU in 2001 the collinear stress-field configuration had been largely ignored. Not only were strains from this configurations substantially smaller than those possible in the orthogonal configuration; the reversibility of strains possible from the collinear configuration were not predicted by existing descriptions of the strain mechanism since both the stress and the field favor the same variants and there is no restoring force.

This work has presented a modified version of the strain mechanism in which pinning sites created by large inclusions in the sample act as internal springs. Twin boundaries attach themselves to the pinning sites; as they are driven by the field and stress they deflect the springs. The presence of these pinning sites, which is substantiated by work done at MIT [76], produces an internal restoring force that explains the reversible strain while also limiting the maximum strain possible from the material. This new understanding of the strain mechanism was used in the development of a mathematical prediction of the output strain that is based on an idealized kernel model developed by Kiefer [39] and expanded by way of a stochastic homogenization method in the sense of Smith [79].

In addition, the experimental work done by Malla [51] was expanded into the dynamic regime through a series of swept-sine high frequency tests that investigated the modulus shift with bias field exhibited by the  $\text{Ni}_{50}\text{Mn}_{28.7}\text{Ga}_{21.3}$ . These tests represent a valuable contribution to the field not only because they help to develop the understanding of Ni-Mn-Ga as exposed to the collinear combination of stress and

field but also because they represent some of the first higher frequency data collected for Ni-Mn-Ga in either configuration. These tests also connect the Ni-Mn-Ga testing to similar testing performed on Terfenol-D and numerous other magnetic materials: both active and inactive. Data on the stiffness and damping dependence on field will also be invaluable to future work on the development of control strategies for the Ni-Mn-Ga solenoid transducers.

## 5.2 Summary of Findings

Of primary importance in the findings presented in this dissertation is the demonstration that it is feasible to employ Ni-Mn-Ga in a solenoid transducer which utilizes a collinear field-stress configuration. Experimental results reported by Malla [51] showed that the  $\text{Ni}_{50}\text{Mn}_{28.7}\text{Ga}_{21.3}$  sample is capable of -0.41% strain at quasi static frequencies. This dissertation extended the testing of this sample into the dynamic range in which it will most likely be used. Swept-sine testing demonstrated the capability of high frequency strain up to 1800 Hz. The resonance point for the test transducer set up was found to shift between 450 and 1000 Hz based on the amount of dc bias field applied to the sample while the resonance point for the independent loaded rod was found to vary between 1200 and 2200 Hz. This shift in resonance is indicative of a shift in the effective elastic modulus of the sample with bias field. This shift, which is sometimes referred to as a Delta-E effect in the literature, is common in many magnetic materials. For example, the Delta-E effect in Terfenol-D has been reported as 160% [36]. Modulus shifts in  $\text{Ni}_{50}\text{Mn}_{28.7}\text{Ga}_{21.3}$  were found to vary based on testing conditions and load. The largest shift of 255% is by far the largest modulus shift reported for a magnetic material. This result shows the promise of Ni-Mn-Ga

for applications involving tunable stiffness elements including vibration control and wave guides. In addition, data from these swept-sine tests can be used to determine the dependence on stiffness and damping on field that will be valuable for control and design of Ni-Mn-Ga actuator applications.

Also key to the future applications of Ni-Mn-Ga solenoid based transducers is the development of a mathematical model to simulate the strain for a given field and stress. Such a model was developed, implemented, and tested in this dissertation. It was found that though the simulation's accuracy is best when the parameters are chosen based on data for the specific loading conditions needed, a single set of parameters optimized to reduce the total error over all loading conditions also provided for accurate results. In fact, errors were measured as less than 2.5% for the set of parameters optimized over all loading conditions which is extremely promising for future design of Ni-Mn-Ga solenoid transducers for specific applications.

### **5.3 Future Work**

As is often the case in research, the investigations presented in this dissertation have led to a more thorough understanding of some questions which have yet to be investigated. These are enumerated here to aid in future research efforts in this area.

- It has been suggested that a more accurate physical description of the pinning mechanism is a bowing of the twin boundary as it is driven past a pinning site. An expression for the bowing energy could more accurately replace the spring energy in the modeling equations.

- The Gibbs free energy expression could be revisited with a focus on the development of an energy well approach similar to that used by Smith for other smart materials [79]
- Experimentally, useful information could be generated through a study of strain vs field curves through a range of frequencies.
- Further microscopic investigations along the lines of those performed by Richard [76] would provide valuable insight into the pinning mechanism and the physical nature of the pinning sites themselves.
- Optimization of the model code may need to be performed if this model is to be used as part of a real time implementation of a control strategy.

## APPENDIX A

### TRANSDUCER MACHINE DRAWINGS

## A.1 Transducer Design

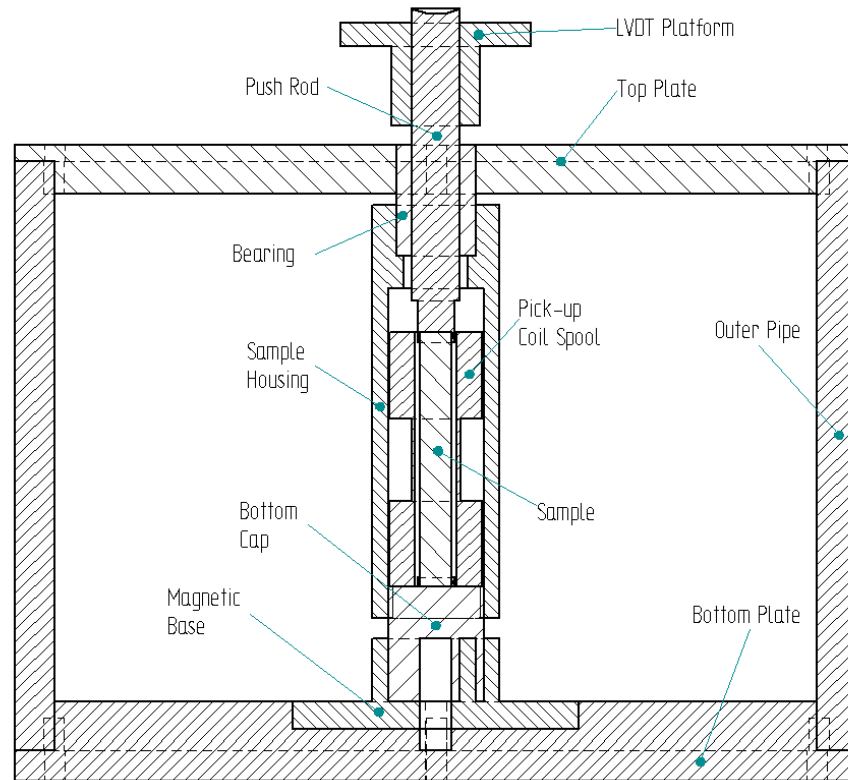


Figure A.1: Cross-section of transducer assembly showing all relevant parts.

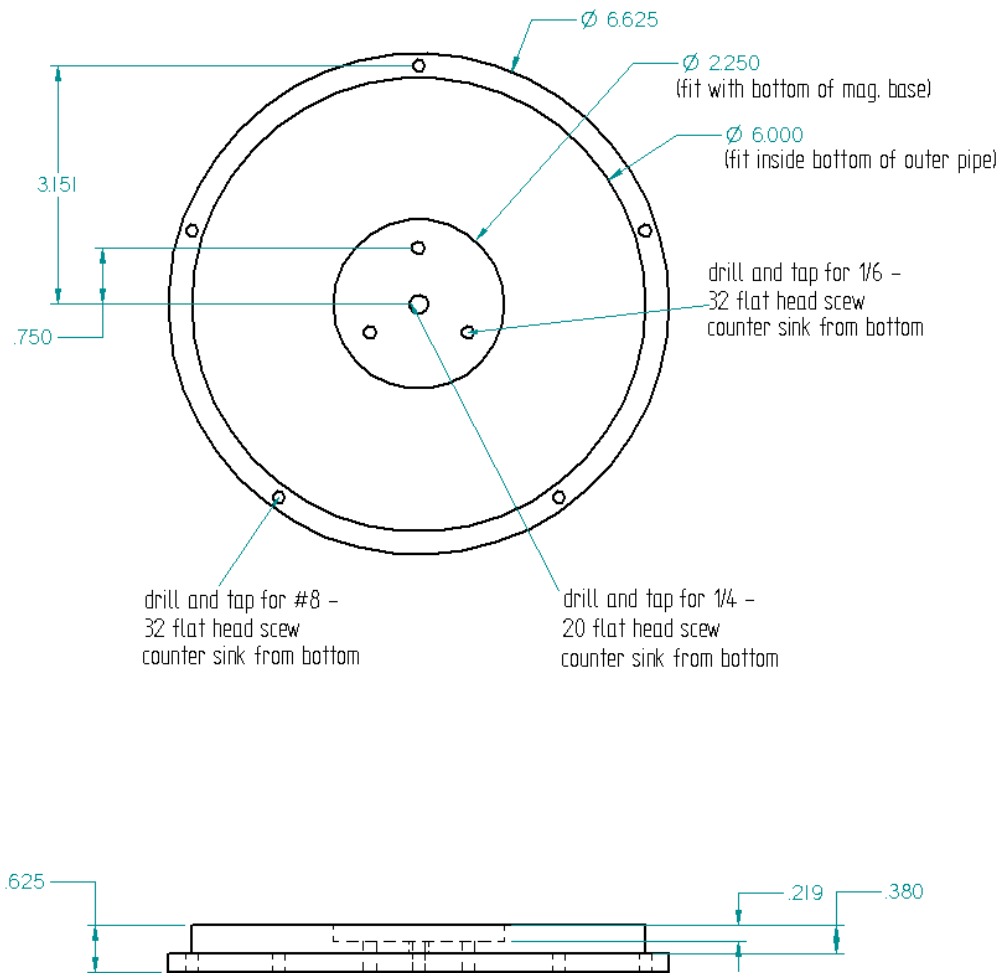


Figure A.2: Bottom plate made from AISI 1018 magnetic steel.

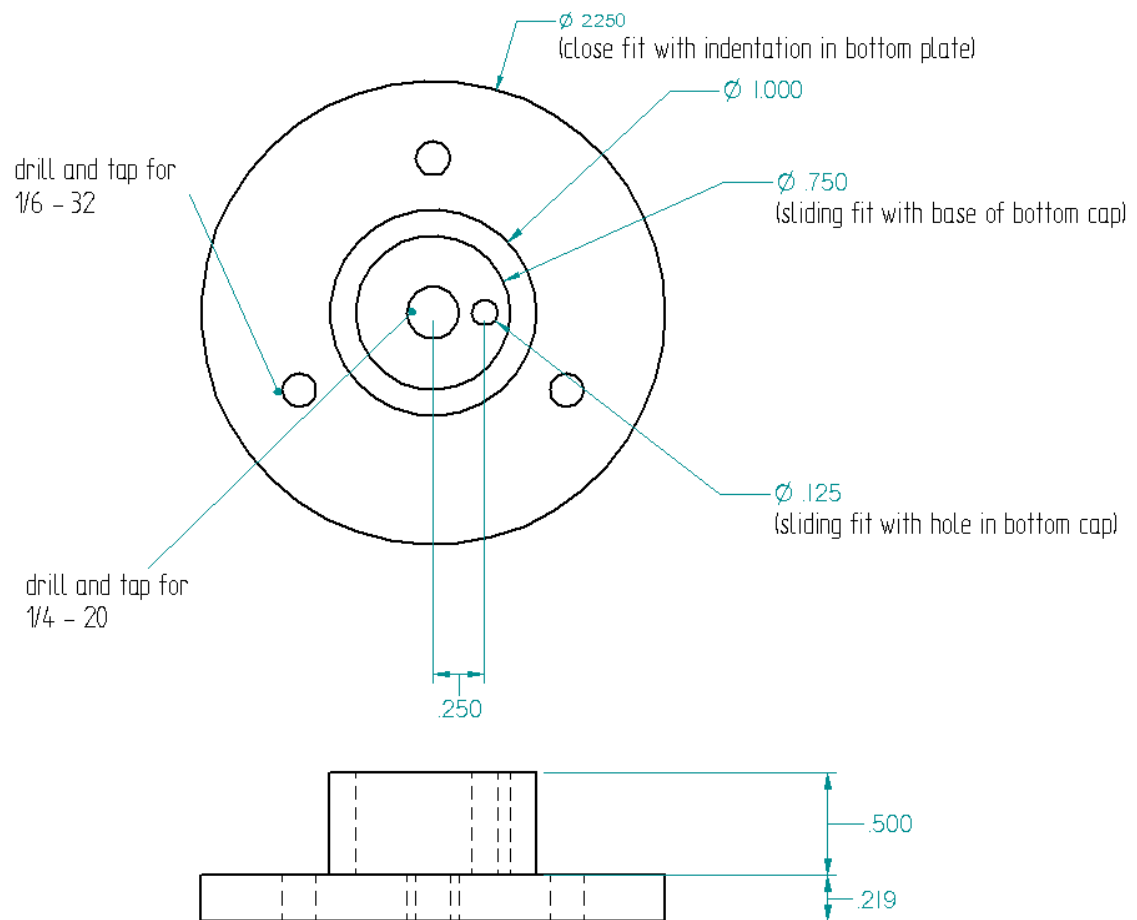


Figure A.3: Magnetic base made from AISI 1018 magnetic steel.



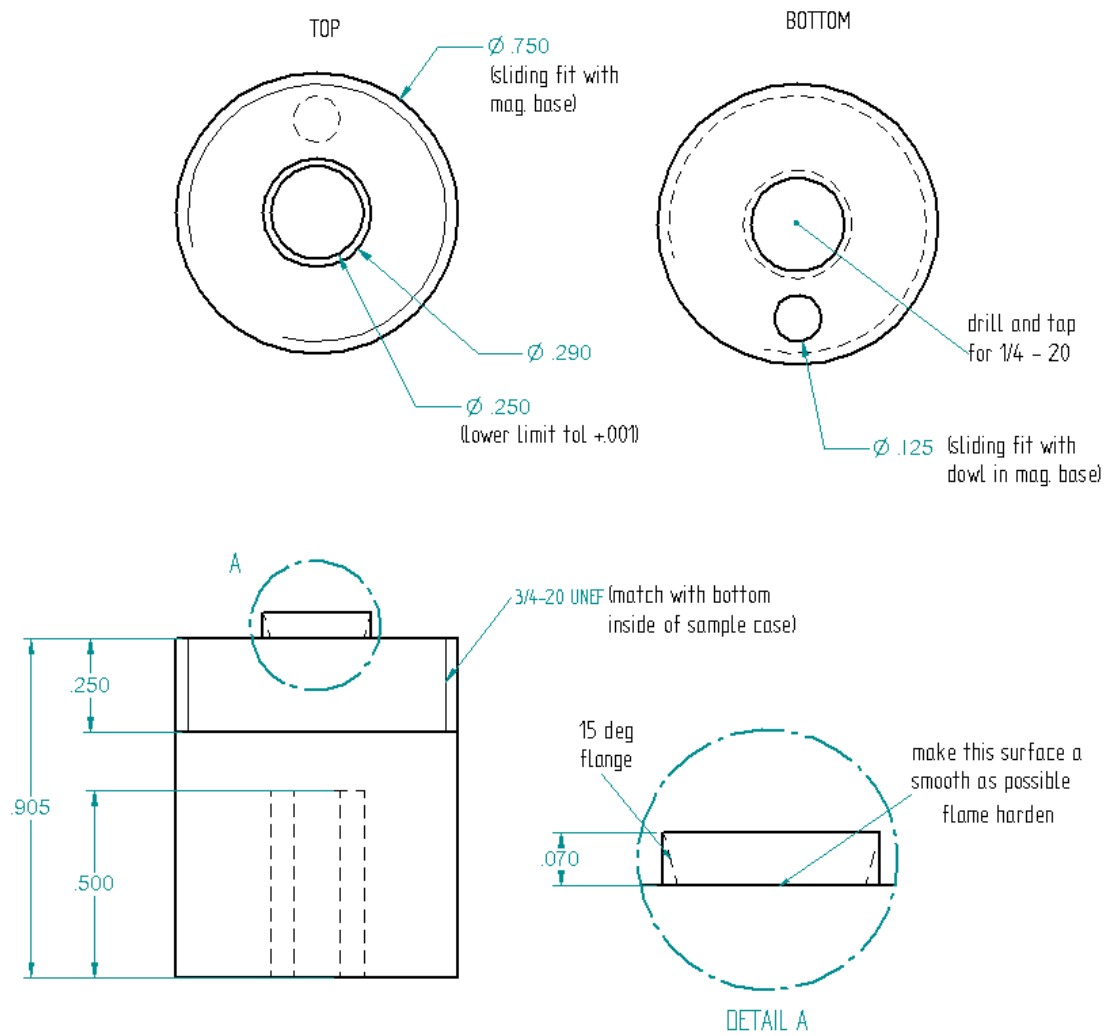


Figure A.4: Bottom cap of sample housing made from AISI 1144 stress proof magnetic steel.

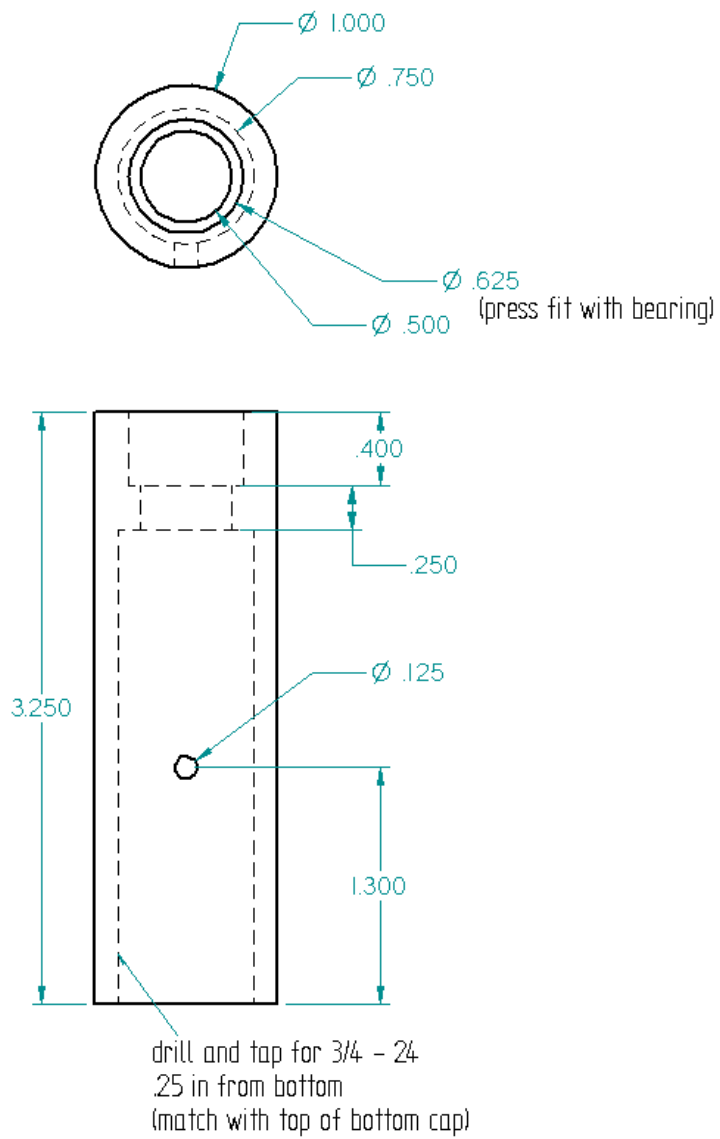


Figure A.5: Sample housing made from AISI 303 stainless (non-magnetic) steel.

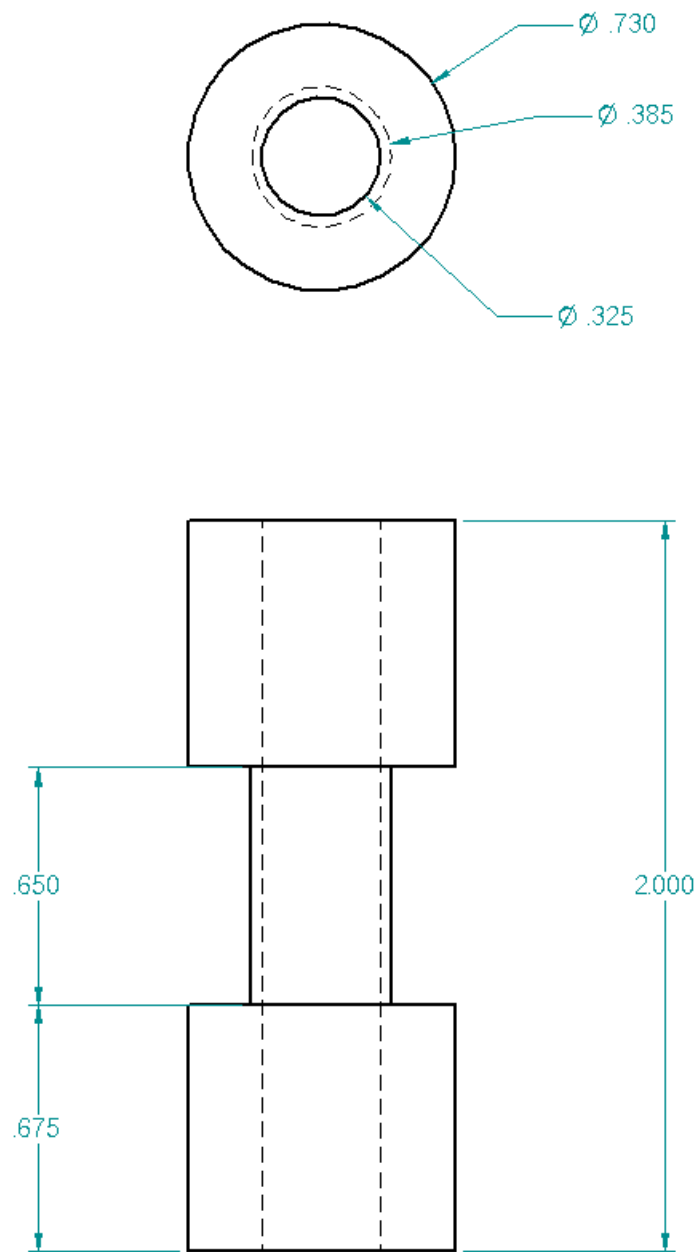


Figure A.6: Pick-up coil spool made of Aluminum 6061-T6.

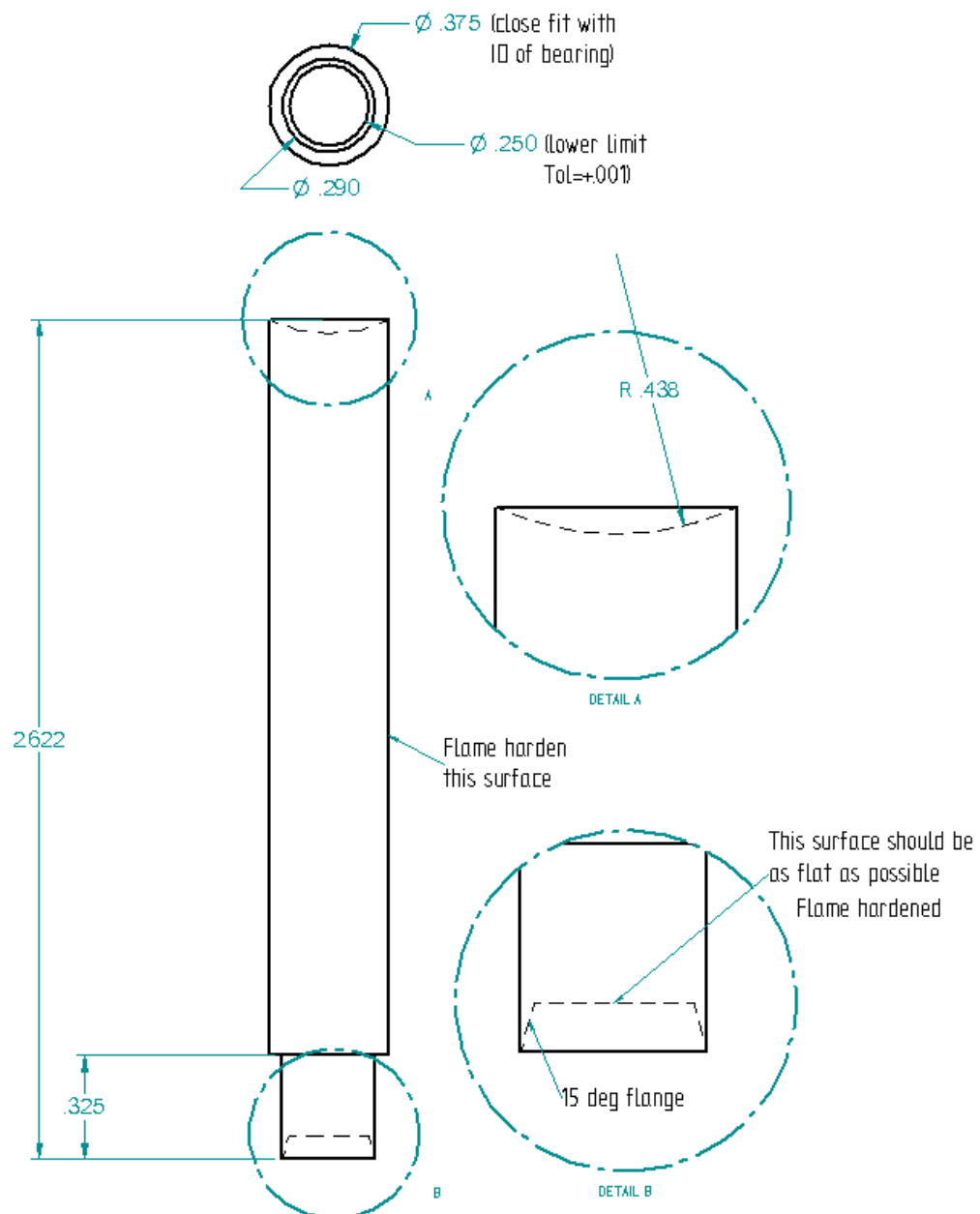


Figure A.7: Push rod made of AISI 1144 stress proof magnetic steel.

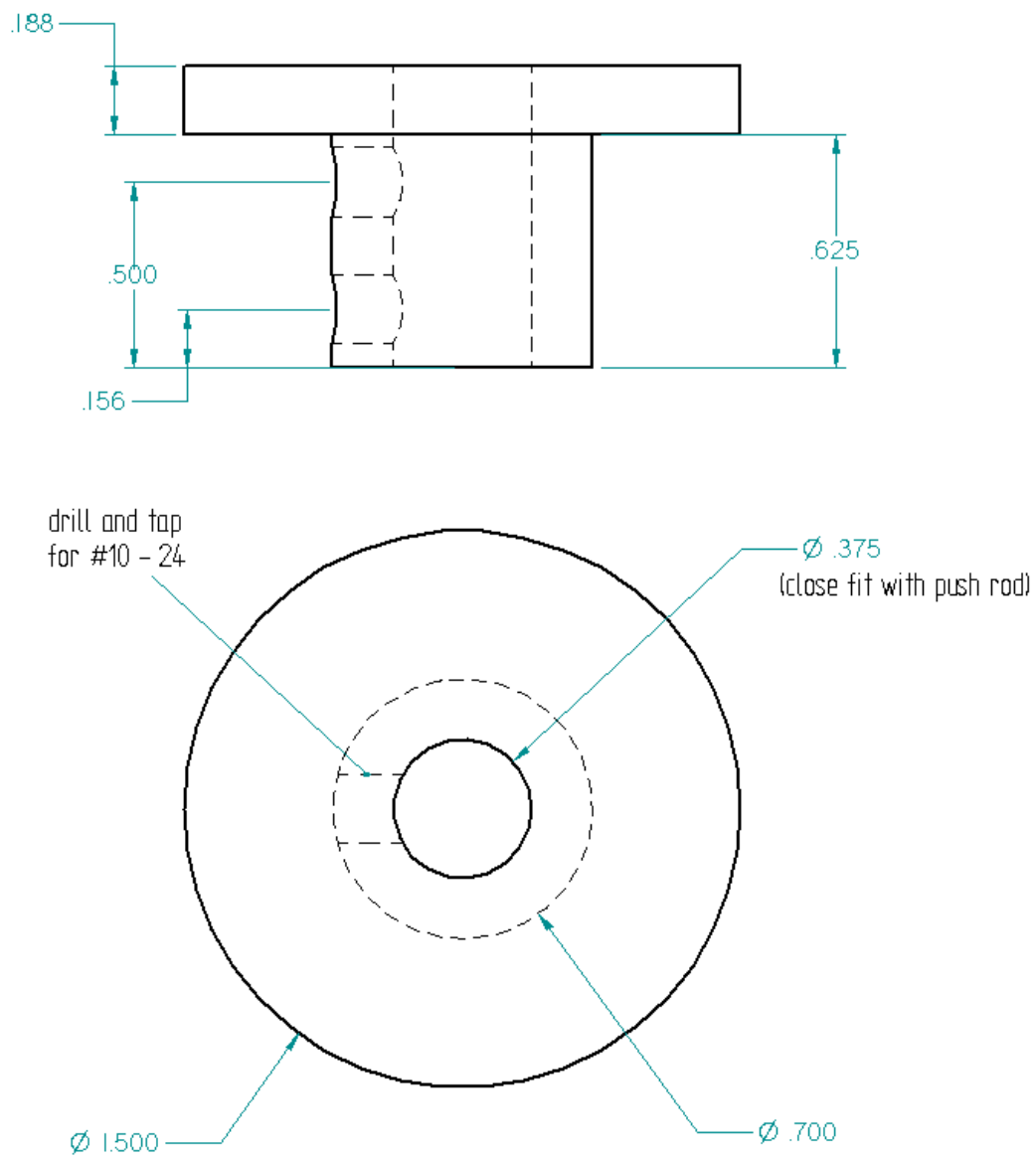


Figure A.8: LVDT platform made of AISI 303 stainless (non-magnetic) steel.

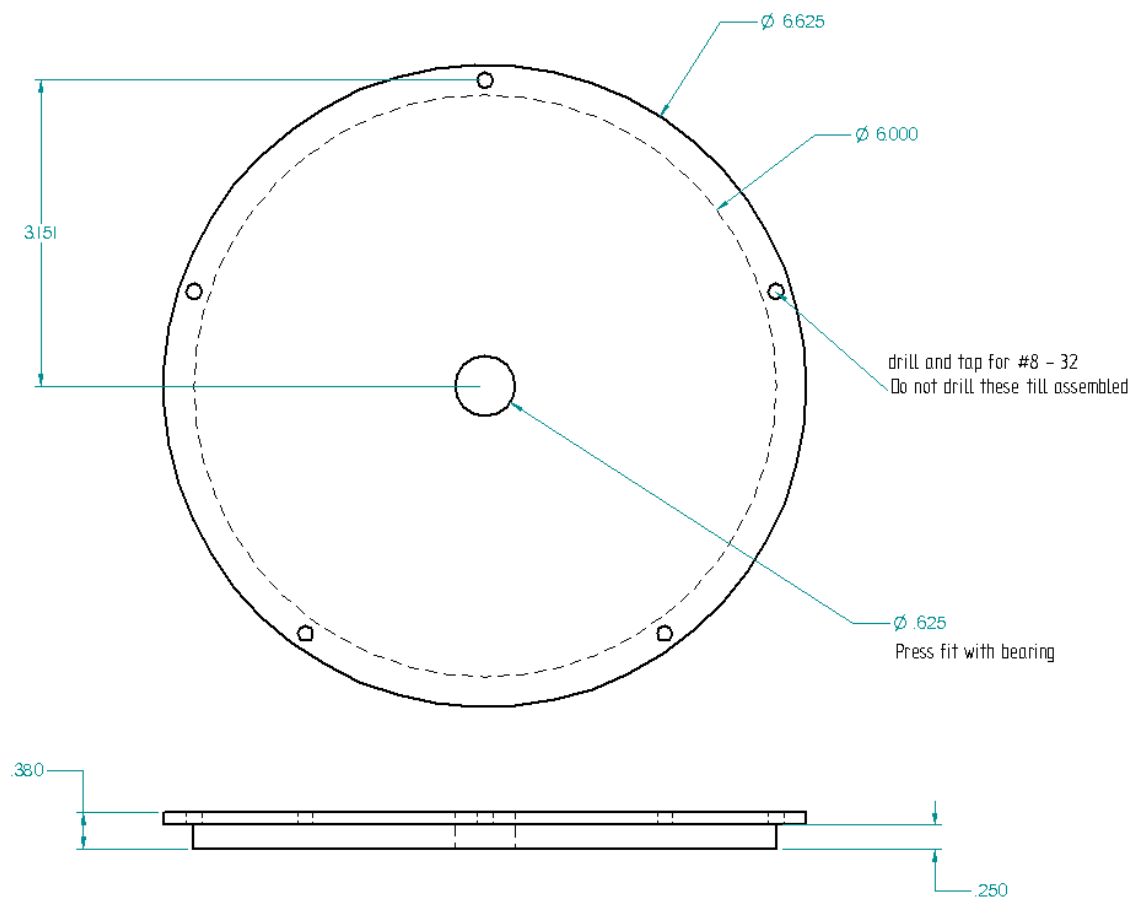


Figure A.9: Top plate made from AISI 1018 magnetic steel.

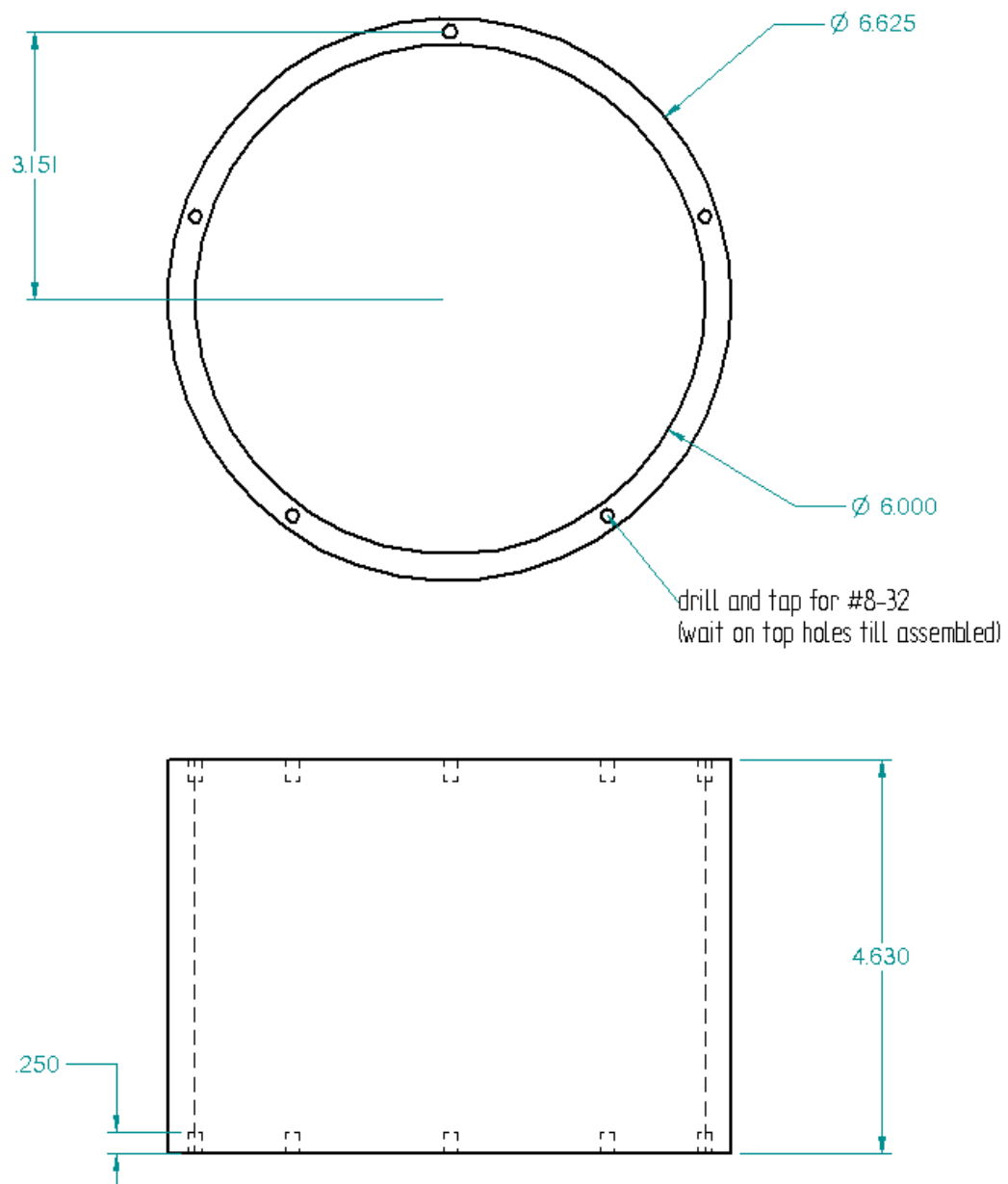


Figure A.10: Outer casing made from AISI 1018 magnetic steel pipe.

## A.2 Modified Transducer Design

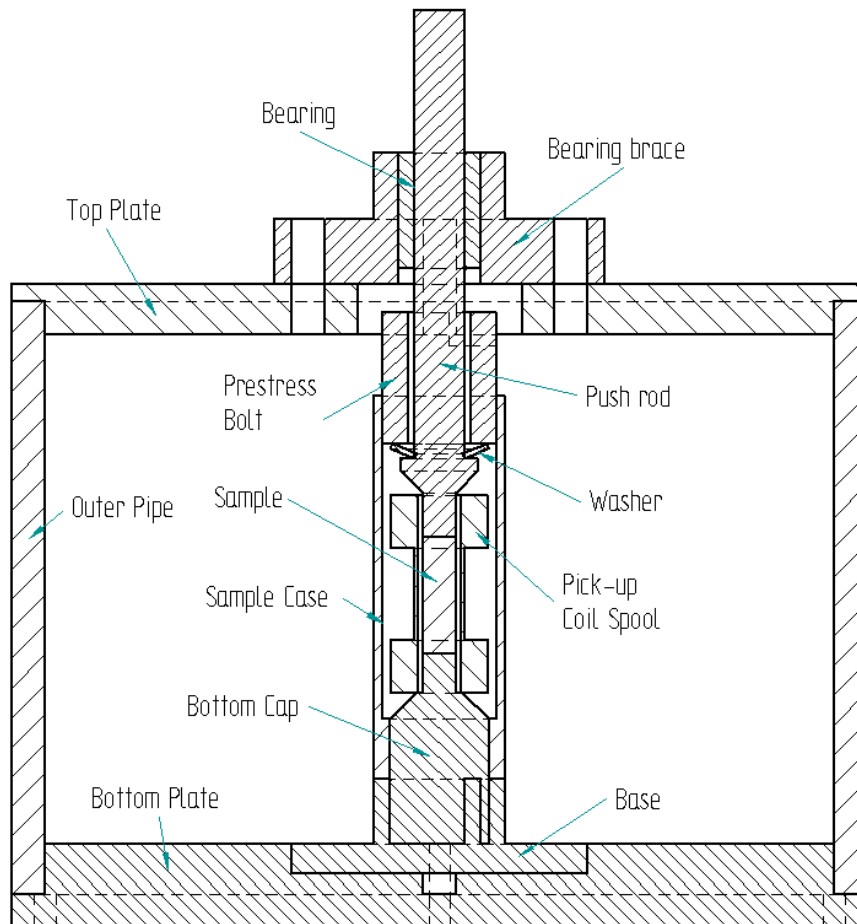


Figure A.11: Cross-section of modified transducer assembly showing all relevant parts.



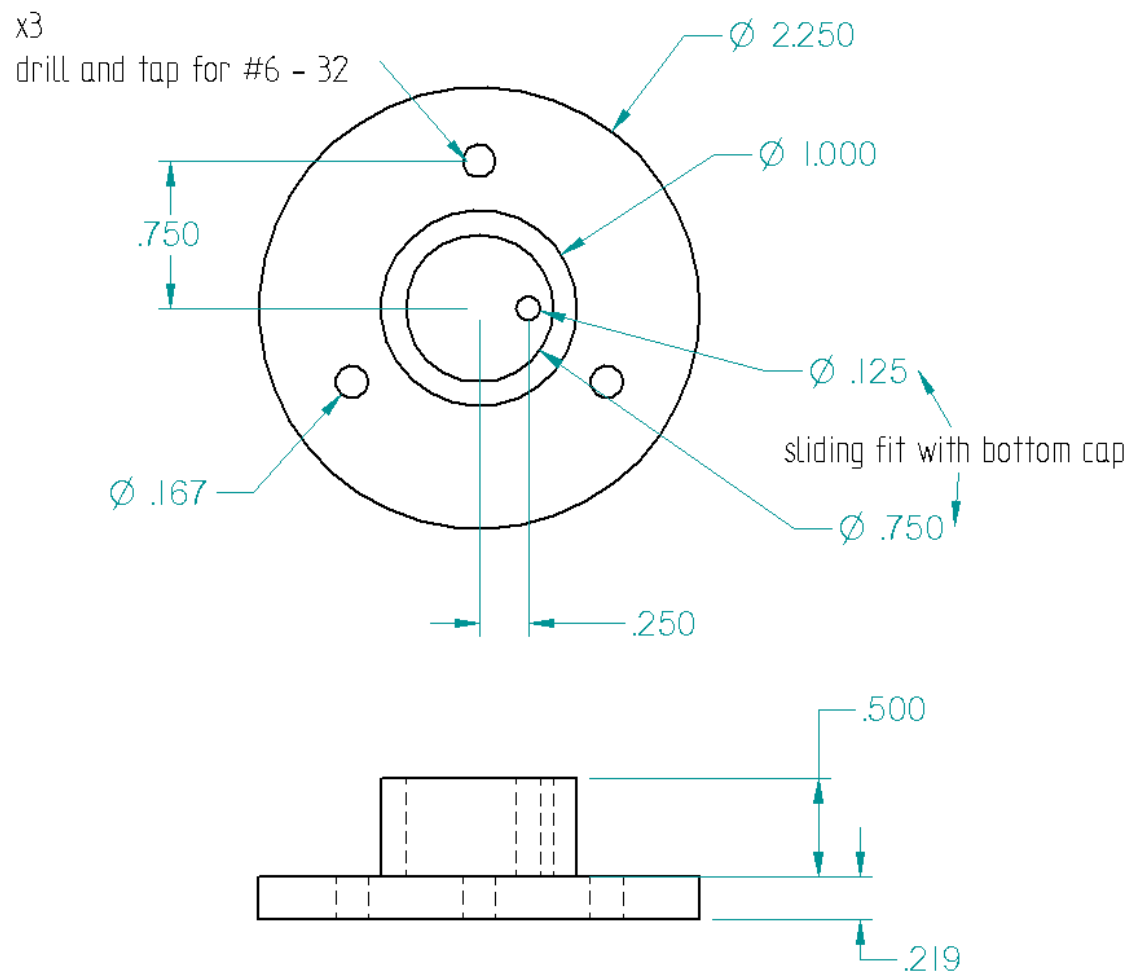


Figure A.12: Base of modified transducer made of AISI 1018 magnetic steel.

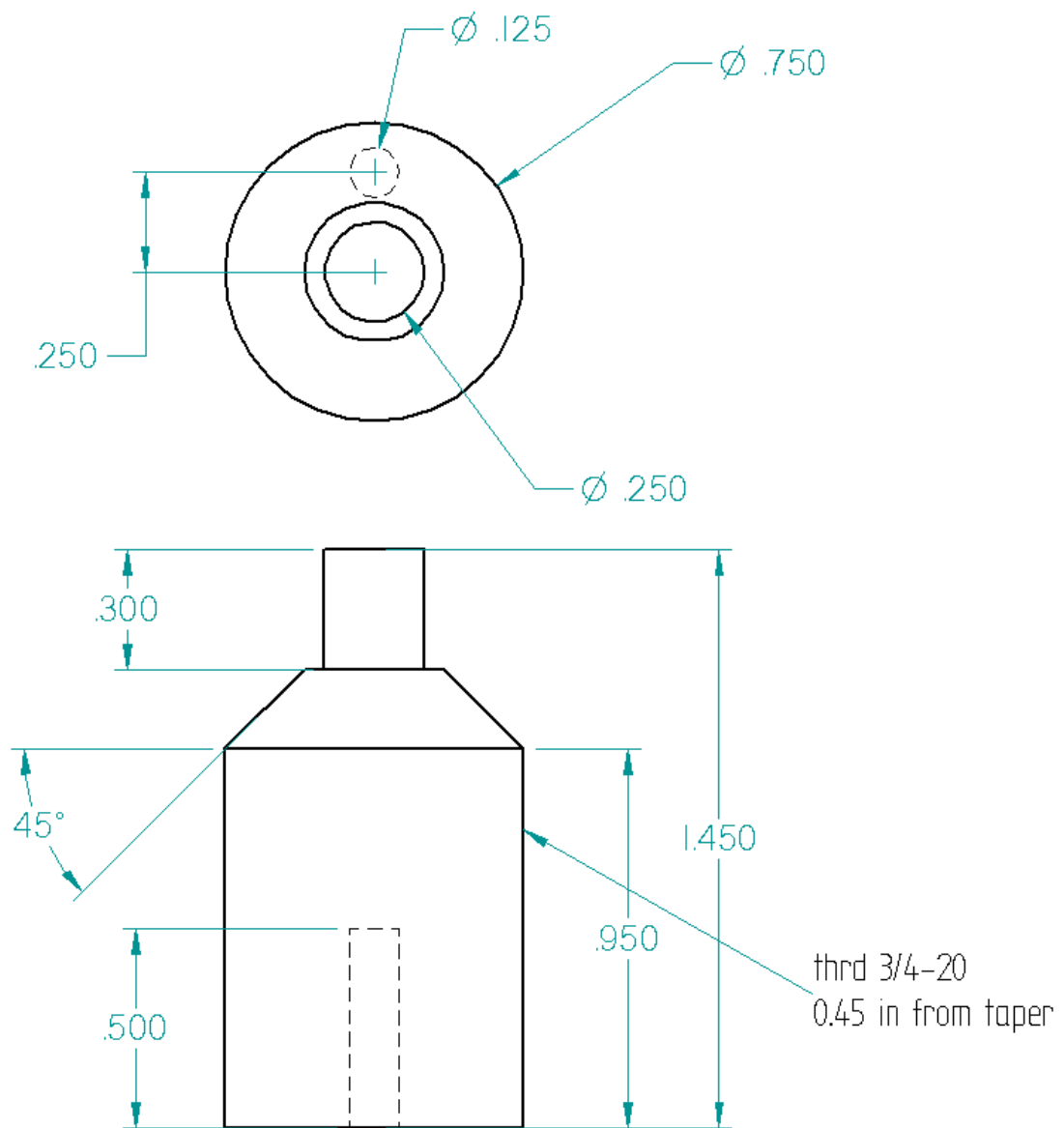


Figure A.13: Bottom cap of sample casing for modified transducer made of AISI 1018 magnetic steel.

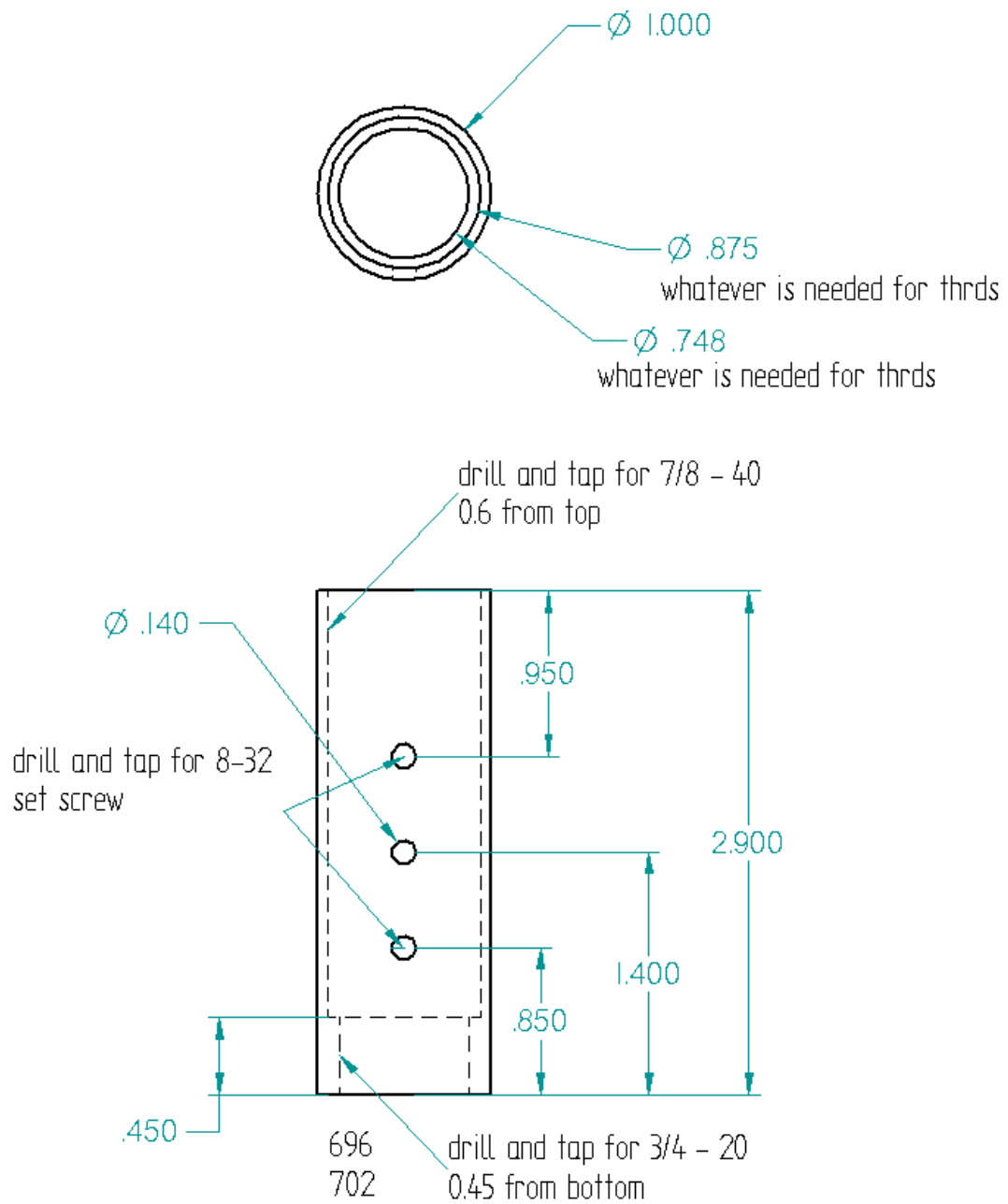


Figure A.14: Outer shell of sample casing for modified transducer made of AISI 1144 non-magnetic steel.

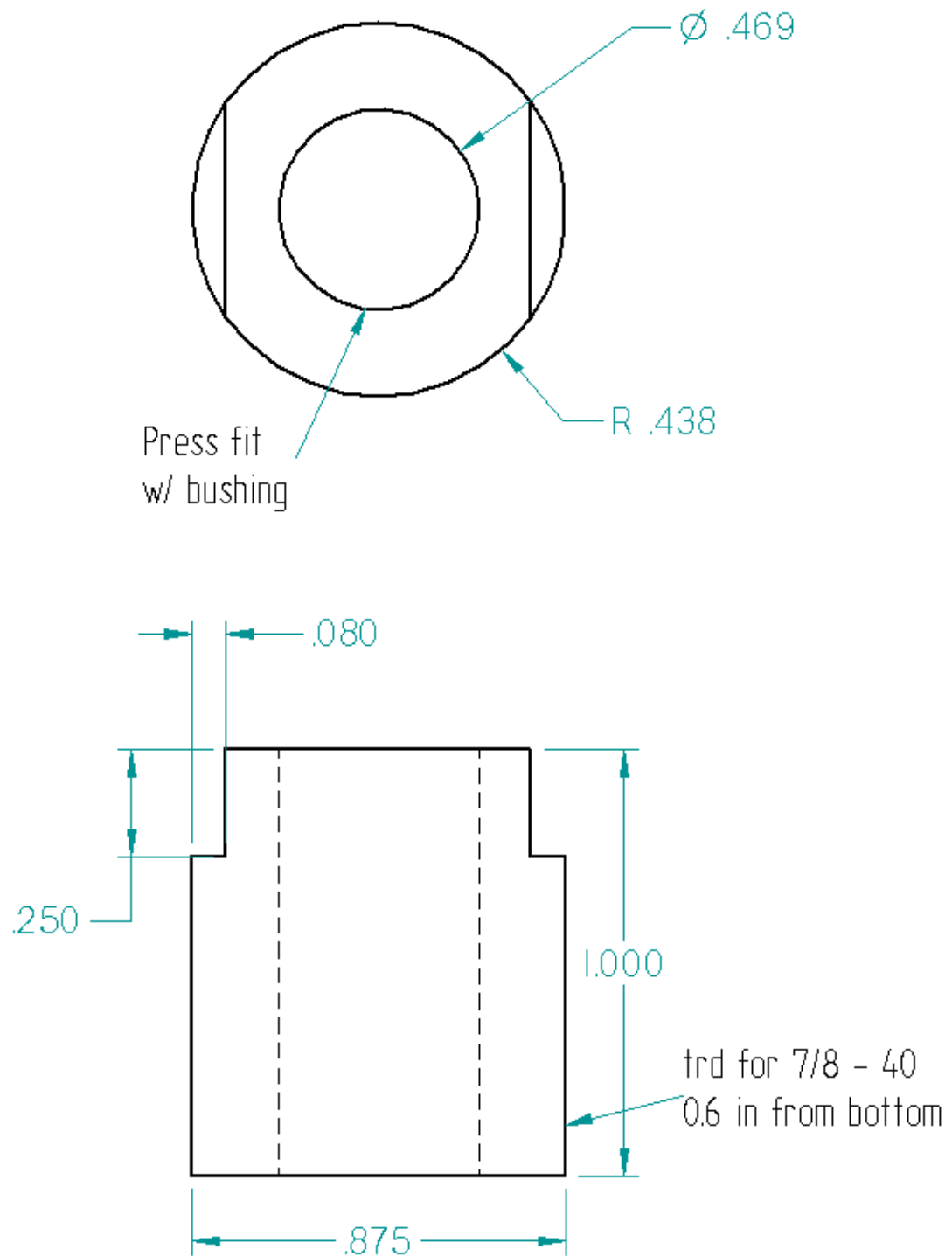


Figure A.15: Upper cap of sample casing for modified transducer which acts as the prestress bolt made of AISI 1018 magnetic steel.

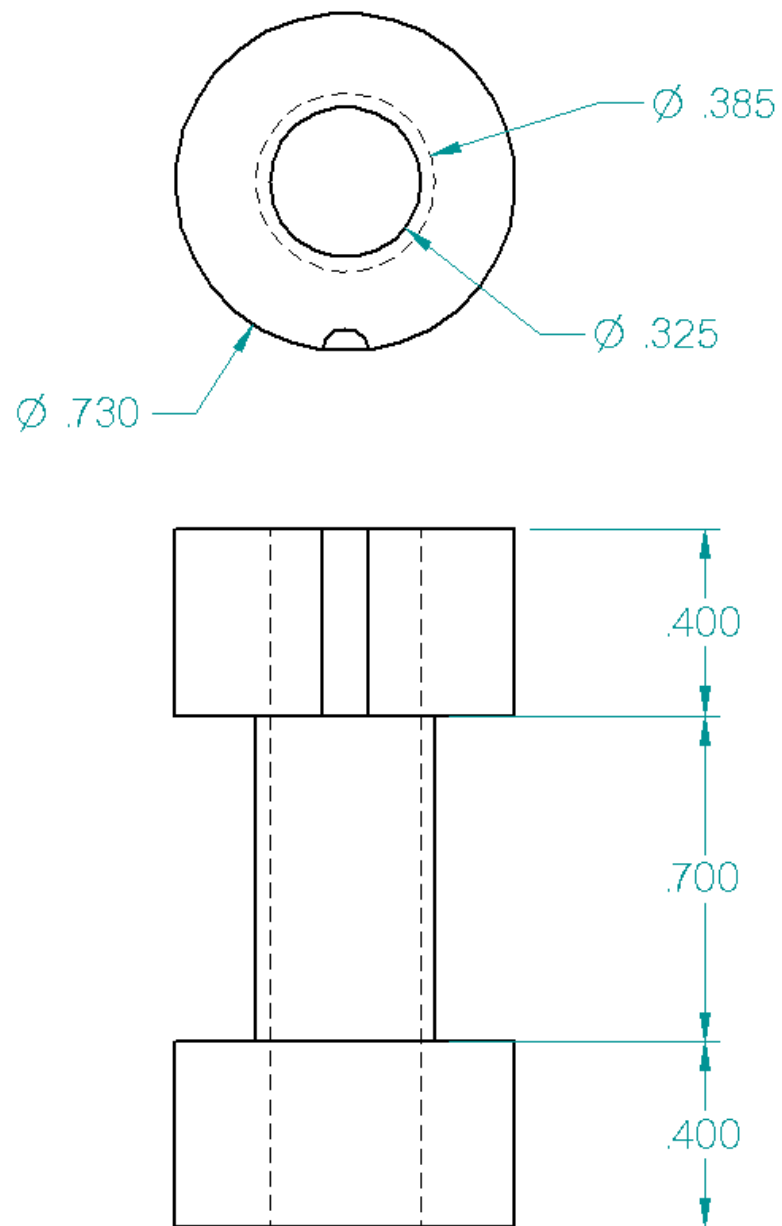


Figure A.16: Pick-up coil spool for modified transducer made of Aluminum 6061-T6.

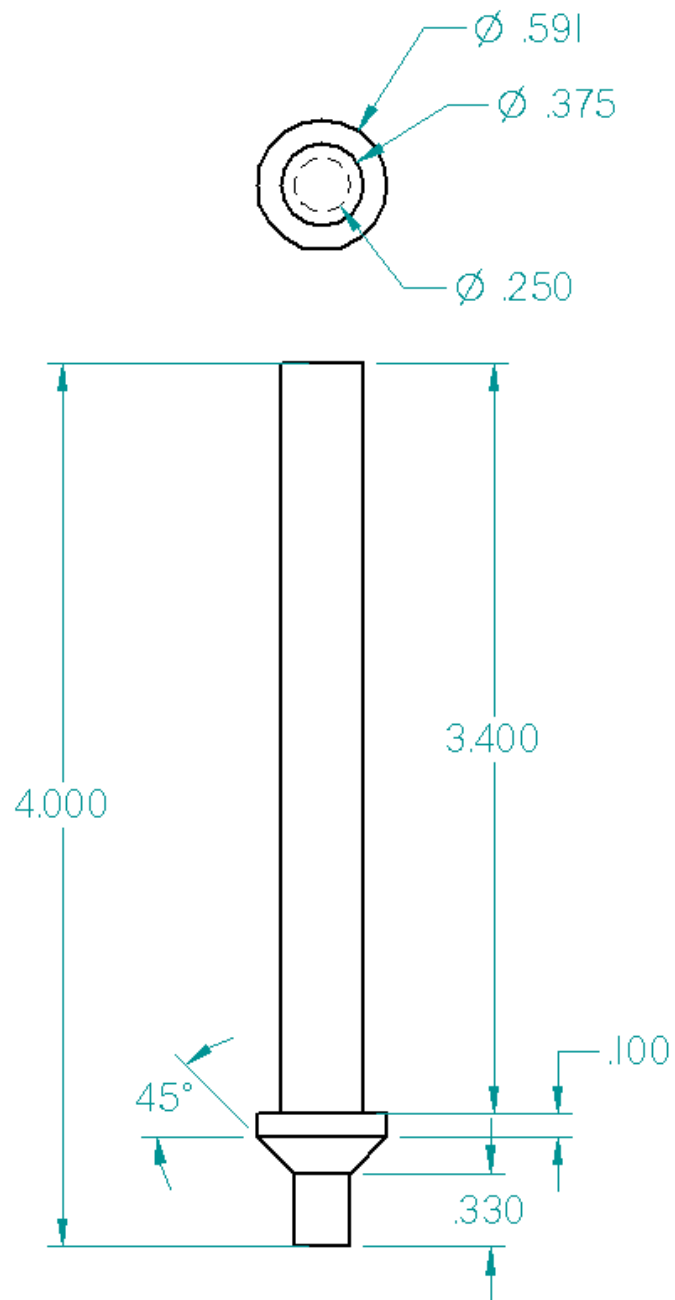


Figure A.17: Push rod for modified transducer made of AISI 1018 magnetic steel.

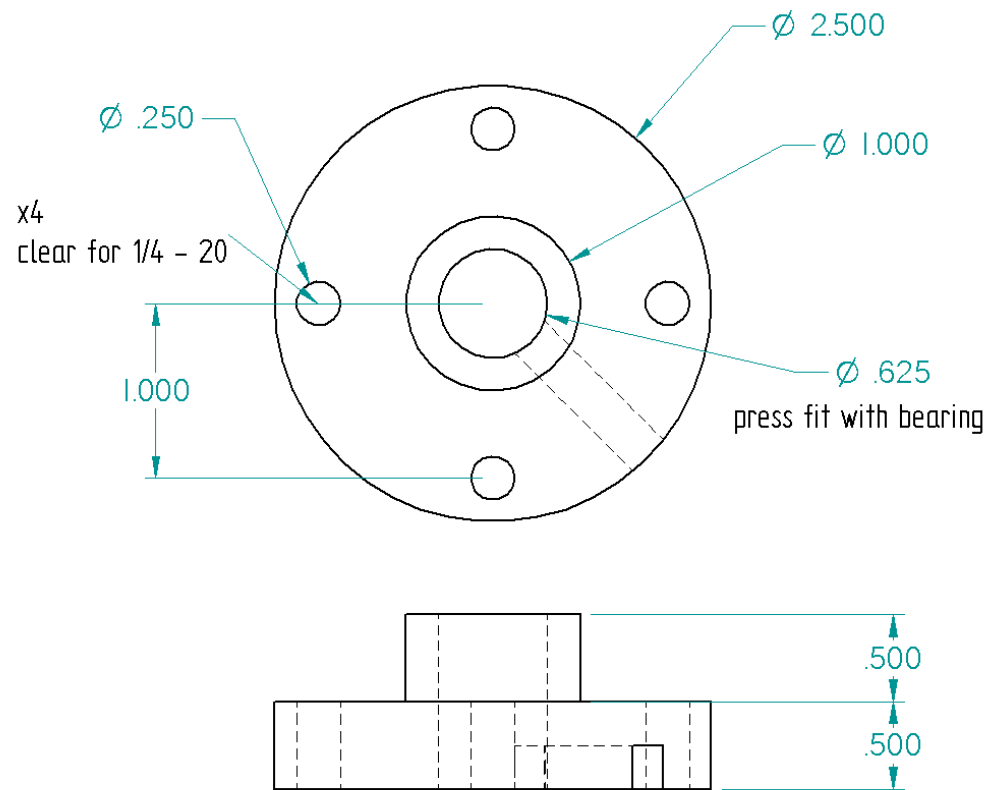


Figure A.18: Bearing brace for modified transducer made of AISI 1018 magnetic steel.

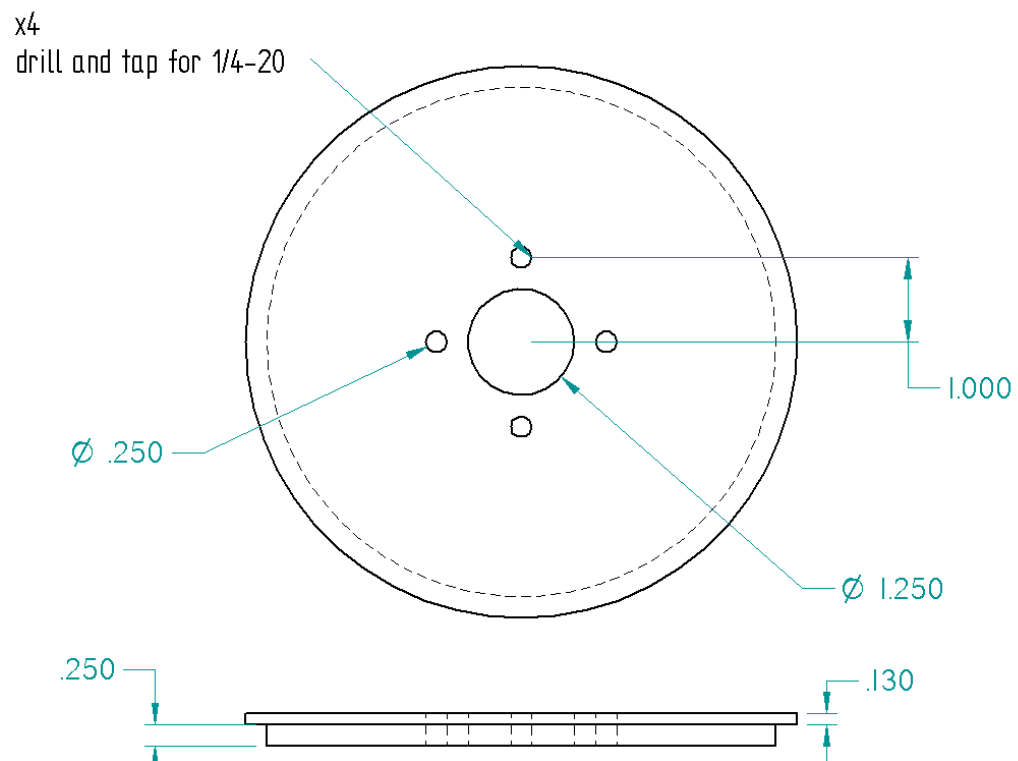


Figure A.19: Top plate for modified transducer made of AISI 1018 magnetic steel.



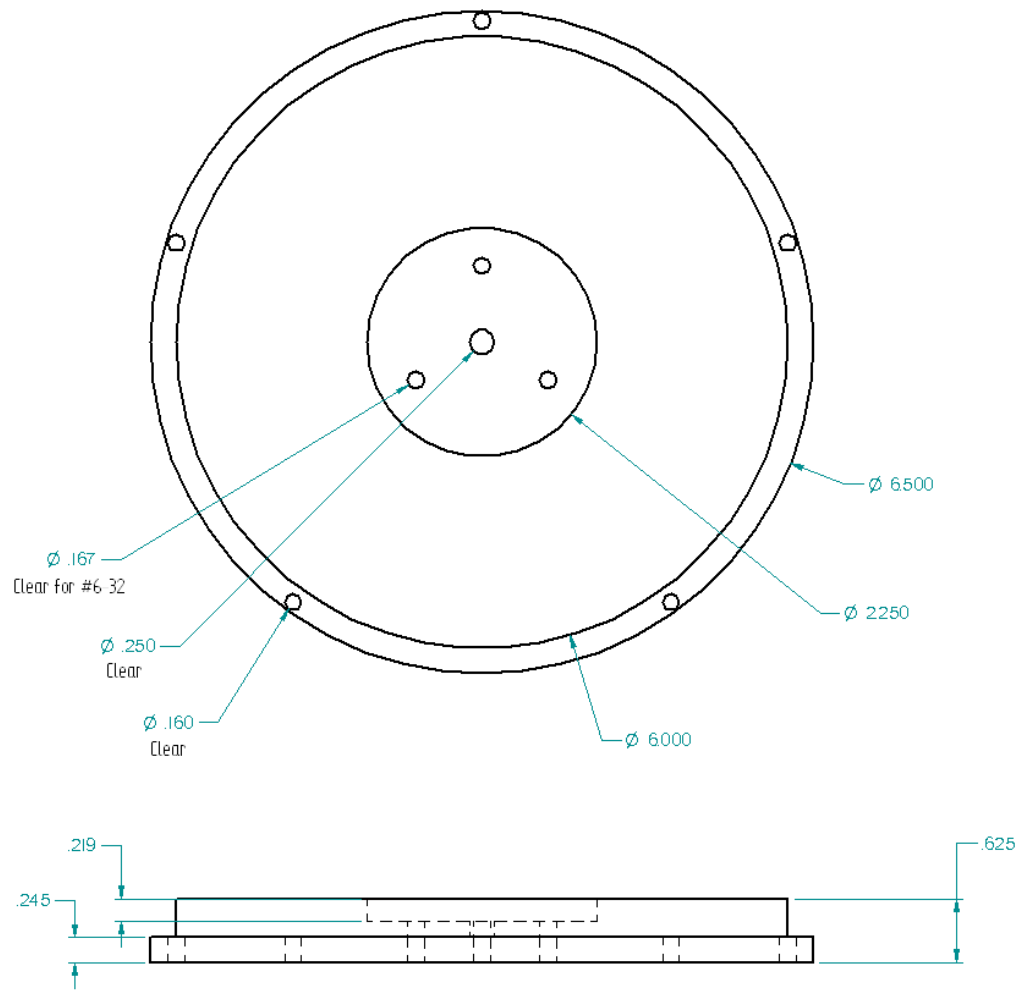


Figure A.20: Bottom plate for modified transducer made of AISI 1018 magnetic steel.

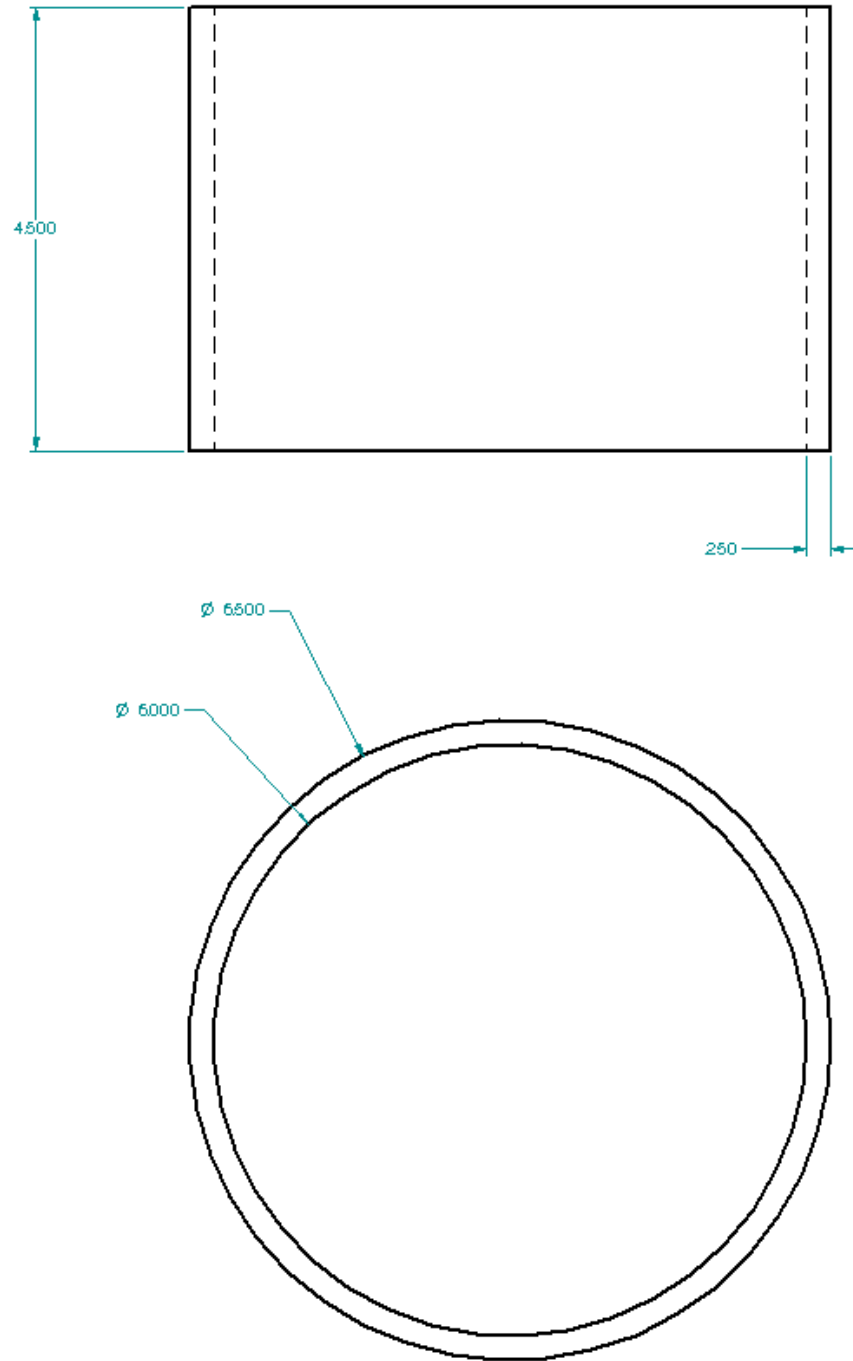


Figure A.21: Outer casing for modified transducer made from AISI 1018 magnetic steel pipe.

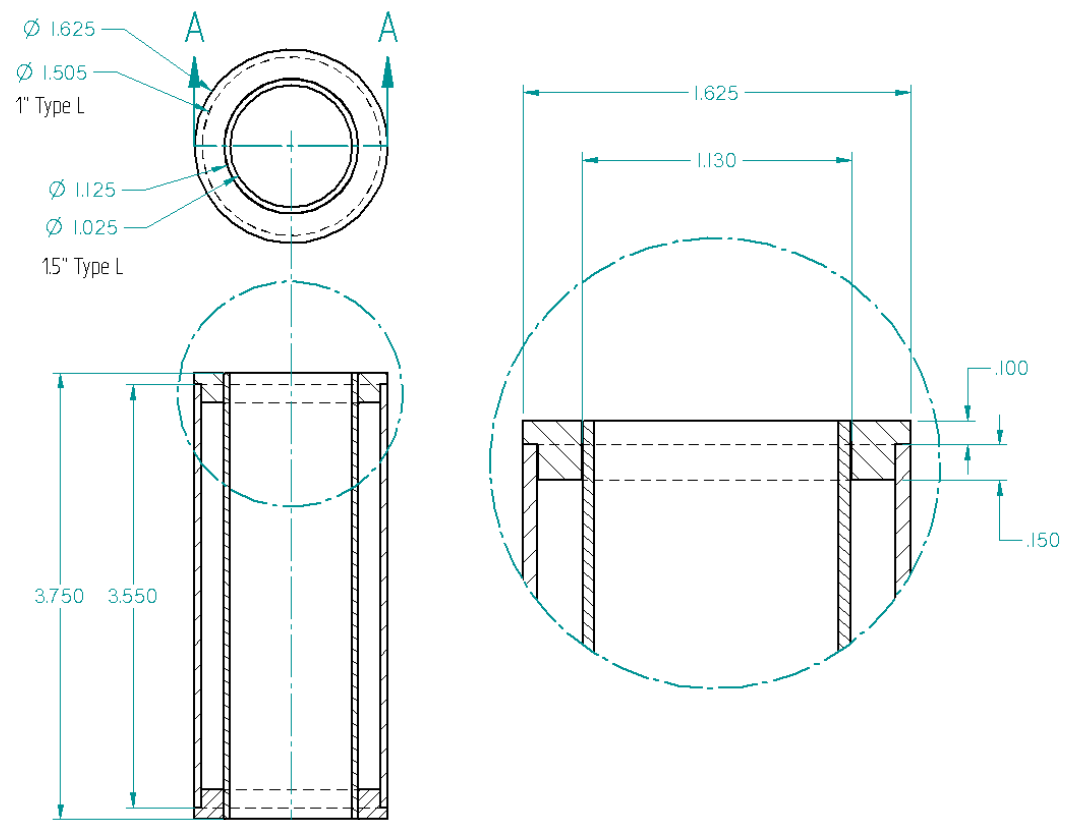


Figure A.22: Cooling sleeve for modified transducer made of copper piping.

## APPENDIX B

### MODEL CODE

#### B.1 Stochastic Homogenization Code

```

function [eps,Htrun] = FEmodel_val(x,pc,co)

switch pc
case 1
    sigma = -0.0125e6;
case 2
    sigma = -0.13e6;
case 3
    sigma = -0.27e6;
case 4
    sigma = -0.41e6;
case 5
    sigma = -0.62e6;
case 6
    sigma = -1.79e6;
case 7
    sigma = -4.15e6;
end

n = x(1);
k2_bar = x(2)*10^6;
c = x(3);
b_bar = x(4)*10^4;

% Find k2_max and H_max such that integration is over part of bell curve
% >90%*max.
k2_max = k2_bar*exp((2*c)*sqrt(-log(.01)));
H_max = sqrt(-2*b_bar^2*log(.01));

K=0;
k2_min = 0; %35e3;
H_min = -H_max;
ss = 'm';
pp = stress_strain;
eps_s=ppval(pp,sigma);

% Load Data
dc = pc;
[eps_d,H_d] = dat_fun(dc);
ldat = length(H_d);

% Input Magnetic Field
H = 700e3*sin([0:pi/ldat:pi]);

% Gaussian Quadrature Set up (1st variable is k, 2nd is H)
gorder = 4; % Number of gaussian points per interval
N1 = 26; % Number of intervals in first variable
N2 = 26; % Number of intervals in second variable

b1(1) = k2_min; % First boundary point for first variable
b1(N1+1) = k2_max; % Last boundary point for first variable
b2(1) = H_min; % First boundary point for second variable
b2(N2+1) = H_max; % Last boundary point for second variable

[t,w] = glen_quad_zw(gorder); % Get gaussian points and weights for standard interval

int_size1 = (b1(N1+1) - b1(1))/N1; % Interval size for first variable
int_size2 = (b2(N2+1) - b2(1))/N2; % Interval size for second variable

for s1=2:(N1+1)
    b1(s1) = b1(s1-1)+int_size1; % Define boundary points for each interval var 1
end

for s2=2:(N2+1)

```

```

        b2(s2) = b2(s2-1)+int_size2;          % Define boundary points for each interval var 2
    end
    % Scaling to interval sizes
    c1=.5*(int_size1);
    m1=.5*(int_size1);
    ts1 = c1+m1.*t;

    c2=.5*(int_size2);
    m2=.5*(int_size2);
    ts2 = c2+m2.*t;

    n_points1 = gorder*N1;    % Number of points
    n_points2 = gorder*N2;    % Number of points

    ts1r=[ts1(4);ts1(1:3)];
    ts2r=[ts2(4);ts2(1:3)];
    wr=[w(4);w(1:3)];

    for s3=1:n_points1
        x1(s3) = b1(ceil(s3/gorder))+ts1r(rem(s3,gorder)+1);
        w1(s3) = m1*wr(rem(s3,gorder)+1);
    end

    for s4=1:n_points2
        x2(s4) = b2(ceil(s4/gorder))+ts2r(rem(s4,gorder)+1);
        w2(s4) = m2*wr(rem(s4,gorder)+1);
    end

    % Finding the Double Integral

    %Weighted distributions
    W1 = w1.*exp(-(log(x1./k2_bar)./(2*c)).^2);
    W2 = w2.*exp(-(x2.^2)./(2*b_bar^2));

    % Determine which kernals to ignore
    gk = good_kern(x2,x1,n,sigma,eps_s);

    Int(1) = 0;
    for s5 =2:length(H)
        Int(s5) = W1*(xi_bar_v(H(s5-1),H(s5),x2,x1,sigma,eps_s,n,K) .*gk)*W2';
    end

    C = -eps_s*10^6/max(abs(Int(2:length(H))))*.99;
    eps = C.*Int(2:length(H));
    Htrun=H(2:length(H));

```

```

function pp = stress_strain

% This function find the piecewise continuous polynomial fit to the the
% stress vs maximum strain data for our sample. It is designed to be used
% with FEmodel.

eps = [4.1000
       2.1455 %2.1170
       1.8158 %1.7776
       1.5743 %1.5572
       1.2416
       0.9617
       0.7295
       0.6282
       0.5508
       0.4794
       0.4020
       0.3543
       0.2650
       0.2174
       0.1816
       0.1638
       0.1399
       0.1280
       0.0983
       0.0863
       0.0744
       0.0804
       0.0625
       0.0625
       0.0506]*-10^-3;

sigma = [0.0121
        0.13 %0.1551
        0.27 %0.2792
        0.41 %0.4033
        0.6515
        0.9617
        1.7684
        2.6370
        3.4436
        4.1262
        4.9328
        5.5533
        7.1044
        8.5315
        9.8345
        11.2616
        12.7508
        14.0538
        16.9080
        19.7001
        27.8904
        31.3030
        34.5295
        51.4685
        58.1696]*-10^6;

pp = pchip(sigma,eps);

temp1 = [-60e6:1000:0];

```

```

function [z,w] = gquad_zw(n)

% This function is a lookup table for the gaussian points and weights for
% various order gaussian quadratures -> n=1,2,3,4,5,9,14. The data was
% taken from Applied Numerical Methods, Carnahan, Luther, and Wilkes -
% 1969. p. 103 and CRC Standard Mathematical Tables and Formulae.

switch n
case 2,
    z=[-0.577350269189626; 0.577350269189626];
    w=[1;1];
case 3,
    z=[-0.774596669241483; 0; 0.774596669241483];
    w=[.555555555555556; .888888888888889; .555555555555556];
case 4,
    z=[-0.861136311594053; -0.339981043584856; 0.339981043584856; 0.861136311594053];
    w=[0.347854845137454; 0.652145154862546; 0.652145154862546; 0.347854845137454];
case 5,
    z=[-0.906179845938664; -0.538469310105683; 0; 0.538469310105683; 0.906179845938664];
    w=[0.236926885056189; 0.478628670499366; 0.568888888888889; 0.478628670499366; ...
        0.236926885056189];
case 6,
    z=[-0.932469514203152; -0.661209386466265; -0.238619186083197; 0.238619186083197; ...
        0.661209386466265; 0.932469514203152];
    w=[0.171324492379170; 0.360761573048139; 0.467913934572691; 0.467913934572691; ...
        0.360761573048139; 0.171324492379170];
case 7,
    z=[-0.9491079123; -0.7415311856; -0.4058451514; 0.0; 0.4058451514; 0.7415311856; ...
        0.9491079123];
    w=[0.1294849662; 0.2797053915; 0.3818200505; 0.4179591837; 0.3818200505; 0.2797053915; ...
        0.1294849662];
case 8,
    z=[-0.9602898565; -0.7966664774; -0.5255324099; -0.1834346425; 0.1834346425; 0.5255324099; ...
        0.7966664774; 0.9602898565];
    w=[0.1012285363; 0.2223810345; 0.3137066459; 0.3626837834; 0.3626837834; 0.3137066459; ...
        0.2223810345; 0.1012285363];
case 9,
    z=[-0.9681602395; -0.8360311073; -0.6133714327; -0.3242534234; 0.0; 0.3242534234; ...
        0.6133714327; 0.8360311073; 0.9681602395];
    w=[0.0812743883; 0.1806481607; 0.2606106964; 0.3123470770; 0.3302393550; 0.3123470770; ...
        0.2606106964; 0.1806481607; 0.0812743883];
case 10,
    z=[-0.9739065285177172; -0.865063366688985; -0.679409568299024; -0.433395394129247; ...
        -0.148874338981631; 0.148874338981631; 0.433395394129247; 0.679409568299024; ...
        0.865063366688985; 0.9739065285177172];
    w=[0.066671344308688; 0.149451349150581; 0.219086362515982; 0.269266719309996; ...
        0.295524224714753; 0.295524224714753; 0.269266719309996; 0.219086362515982; ...
        0.149451349150581; 0.066671344308688];
case 15
    z=[-0.987992518020485; -0.937273392400706; -0.848206583410427; -0.724417731360170; ...
        -0.570952172608539; -0.394151347077563; -0.201194093997435; 0; 0.201194093997435; ...
        0.394151347077563; 0.570952172608539; 0.724417731360170; 0.848206583410427; ...
        0.937273392400706; 0.987992518020485];
    w=[0.030753241996117; 0.070366047488108; 0.107159220467172; 0.139570677926154; ...
        0.166269205816994; 0.186161000115562; 0.198431485327111; 0.202578241925561; ...
        0.198431485327111; 0.186161000115562; 0.166269205816994; 0.139570677926154; ...
        0.107159220467172; 0.070366047488108; 0.030753241996117];
end

```



```

function eps_mod = xi_bar_v(H,H_next,Hi,k2,sigma,eps_s,n,K)

% Define Coefficients
S=0;
mu_0 = 1.256e-006; %NA^-2
Ms = 622000; %Am^-1
rho=1;
Y= 209570;
eps_th = -60000e-6;
H1 = 10750; % average of measured values
eps_2 = -5.7612e-023*sigma^3 + -4.0960e-016*sigma^2 + -8.5320e-010*sigma + -6.3526e-004;
% 3rd order fit (only 4 data points)

slope=H_next-H;
Hy=H+Hi;

[Hy_m,k2_m] = meshgrid(Hy,k2);

c1 = eps_s.*sigma + 1/2*S.*sigma.^2 + mu_0*Ms*H1 - Y;
c2_m = eps_s.*sigma + 1/2*S.*sigma.^2 + Y - 2*k2_m.*eps_2./eps_th;

k1_m=n.*k2_m;

xi_s = eps_s/eps_th;

xi1 = (slope>=0).*(1./(2.*rho.*k1_m).*(eps_s*sigma+.5*S*sigma^2+mu_0.*Ms.*Hy_m-rho*c1-Y + K.*Hy_m)) ...
      + (slope<0).*(1./(2.*rho.*k2_m).*(eps_s*sigma+.5*S*sigma^2+mu_0.*Ms.*Hy_m-rho.*c2_m+Y + K.*Hy_m));

xi = (xi1<xi_s).*xi1 + (xi1>xi_s).*xi_s; % Original code

eps_mod = eps_th.*xi;

```

## B.2 Parameter Identification Code

```
% Constrain Optimization for the FEmodel
tic
% Case
dc = 4; % Remember to change this in FE_opt and my_const as well

%fun = @FEmodel_fun;
fun = @Fun_opt;
const = @my_const;

%k_max_i = 7; % *10^6 initial guess for k_max (7.1e6,
%k_max_u = 8; % *10^6 upper bound on k_max (4e6,
%k_max_l = 1; % *10^6 lower bound on k_max (3e6
%H_max_i = .036; % *10^4 initial guess for H_max (3.5e4
%H_max_u = .1; % *10^4 upper bound on k_min (1e4
%H_max_l = .001; % *10^4 lower bound on k_min (.1e4
n_i = 1.2; % initial guess for n (1.27
n_u = 2; % upper bound on n (2,
n_l = 1; % lower bound on n (1,
k_bar_i = 1; % *10^6 initial guess for k_bar (1.32e6
k_bar_u = 3; % *10^6 upper bound to k_bar (3e6
k_bar_l = .5; % *10^6 lower bound to k_bar (.7e6
c_i = .4;
c_u = 1;
c_l = .1;
b_i = 2;
b_u = 5;
b_l = .01;

ub = [n_u,k_bar_u,c_u,b_u];
lb = [n_l,k_bar_l,c_l,b_l];
x0 = [n_i,k_bar_i,c_i,b_i];
%x0 = [1.1207,0.75325,0.99901,0.010304];

%A = -1*[1,1,2*sqrt(-log(.01)),0];
%b = make_b(dc);

%[1.0565, 0.82232, 0.8301, 0.019501][x,fval] = fmincon(fun,x0,[],[],[],[],lb,ub); % Case 1,2
[x,fval] = fmincon(fun,x0,[],[],[],[],lb,ub,const); % Case 3
fval

% Load Data
%[eps_d,H_d] = data_stgage(dc);
[eps_d,H_d] = dat_fun(dc);
ldat = length(H_d);

% Evaluate FEmodel and chose values
[eps,H] = FEmodel_val(x,dc,'r');

figure(10); hold on; plot(H_d,eps_d,'b'); plot(H_d,eps,'r');
legend('data','model');

format short g
x
toc
```

```

function f = Fun_opt(x)

dc=4;

% Evaluate Model with these parameters
[eps,H] = FEmodel_val(x,dc,'r');

% Load Data for this case
[eps_d,H_d] = dat_fun(dc);

% Calculate Error

i1 = find(eps_d==0);
i2 = find(H==max(H));

%----- Absolute Value of the Difference
err = abs(eps(i1+1:length(eps_d)-1)-eps_d(i1+1:length(eps_d)-1));
%f = sum(err);
f = mean(err);
%[f,in] = max(err)
%max_per = max(err)/eps_d(i1+in-1)


function gk = good_kern(Hi,k2,n,sigma,eps_s);

H = 700e3;

S=0;
mu_0 = 1.256e-006; %NA^-2
Ms = 622000; %Am^-1
rho=1;
Y= 209570;
eps_th = -60000e-6;
H1 = 10750; % average of measured values
eps_2 = -5.7612e-023*sigma^3 + -4.0960e-016*sigma^2 + -8.5320e-010*sigma + -6.3526e-004;
% 3rd order fit (only 4 data points)

K = 0;

Hy=H+Hi;

[Hy_m,k2_m] = meshgrid(Hy,k2);

k1_m=n.*k2_m;

c1 = eps_s.*sigma + 1/2*S.*sigma.^2 + mu_0*Ms*H1 - Y;
c2_m = eps_s.*sigma + 1/2*S.*sigma.^2 + Y - 2*k2_m.*eps_2./eps_th;

xi1 = (1./(2.*rho.*k1_m).*(eps_s*sigma+.5*S*sigma^2+mu_0.*Ms.*Hy_m-rho*c1-Y + K.*Hy_m));

gk = xi1>=abs(eps_s)/abs(eps_th);

```

```

function [c,ceq] = my_const(x)

pc = 4;

switch pc
    case 1
        sigma = -0.0125e6;
    case 2
        sigma = -0.13e6;
    case 3
        sigma = -0.27e6;
    case 4
        sigma = -0.41e6;
    case 5
        sigma = -0.62e6;
    case 6
        sigma = -1.79e6;
    case 7
        sigma = -4.15e6;
end

n = x(1);
k2_bar = x(2)*10^6;
c = x(3);
b_bar = x(4)*10^4;

H = 700e3;

p = .1; % Reduction of constraint parameter

S=0;
mu_0 = 1.256e-006; %NA^-2
Ms = 622000; %Am^-1
rho=1;
Y= 209570;
eps_th = -60000e-6;
H1 = 10750; % average of measured values
eps_2 = -5.7612e-023*sigma^3 + -4.0960e-016*sigma^2 + -8.5320e-010*sigma + -6.3526e-004;
% 3rd order fit (only 4 data points)
pp = stress_strain;
eps_s=ppval(pp,sigma);
K = 0;
k2_max = k2_bar*exp((2*c)*sqrt(-log(.01)));
Hi_max = sqrt(-2*b_bar^2*log(.01));

Hy=H-Hi_max;

k1_m=n.*k2_max;

c1 = eps_s.*sigma + 1/2*S.*sigma.^2 + mu_0*Ms*H1 - Y;

xi1 = (1./(2.*rho.*k1_m).*(eps_s*sigma+.5*S*sigma^2+mu_0.*Ms.*Hy-rho*c1-Y + K.*Hy));
%xi2 = (1./(2.*rho.*k2_m).*(eps_s*sigma+.5*S*sigma^2+mu_0.*Ms.*Hy_m-rho.*c2_m+Y + K.*Hy_m));

c = abs(eps_s)/abs(eps_th)*p - xi1;
ceq = 0;

```

```

% This will load the data for comparison with the model.

function [eps,H] = dat_fun(c)
%c = 4;

l = 0.883; % in

load data/steeldata_manip.mat; % load steel data

switch c
    case 1
        load data/0002;
    case 2
        load data/00040;
    case 3
        load data/00042;
    case 4
        load data/00044;
    case 5
        load data/00048;
    case 6
        load data/00054;
    case 7
        load data/00060;
end

H = X1(:,2)*20*167*79.58/1000; % kA/m
eps1 = X3(:,2)*1e-3/1.26/1*1e6; % micro-strain

%eps2 = eps1*.62;
eps2 = eps1;

% Truncate data to 1/2 cycle

np = length(H);

i1 = find(H(round(np/10):np)>=0);
H = H(i1(1)+round(np/10)-1:length(H));
eps2 = eps2(i1(1)+round(np/10)-1:length(H));

i2 = find(H<0);
H = H(1:i2(1));
eps2 = eps2(1:i2(1));

% Subtract steel effects

eps_st_long = interp(eps_st, round(length(eps2)/length(eps_st)));

if length(eps_st_long) > length(eps2)
    eps_st_long = eps_st_long(1:length(eps2));
    num_cut_points = length(eps_st_long) - length(eps2);
elseif length(eps_st_long) < length(eps2)
    eps2 = eps2(1:length(eps_st_long));
    num_cut_points = length(eps_st_long) - length(eps2);
end

eps = eps2 - eps_st_long;
eps = eps - max(eps);

eps = .6*eps; %apply correction factor (grrr)

```

```

function f = Fun_tot_opt(x)

for dc = 1:4 % Data for Case

% Evaluate Model with these parameters

[eps,H] = FEmodel_val(x,dc,'r');

% Load Data for this case

[eps_d,H_d] = dat_fun(dc);

% Calculate Error

i1 = find(eps_d==0);
i2 = find(H==max(H));

%----- Absolute Value of the Difference
err = abs(eps(i1:length(eps_d))-eps_d(i1:length(eps_d)))';
%err = abs(eps(i1+1:length(eps_d)-1)-eps_d(i1+1:length(eps_d)-1))'./abs(eps_d(i1+ ...
1:length(eps_d)-1))';
%err_tot(:,dc) = sum(err);
err_tot(:,dc) = mean(err);
%err_tot(:,dc) = max(err);

end

f = sum(err_tot);

```

## B.3 Kernel Model Code

```

clear all

% Input Measured Quantities

mu_0 = 1.256e-6; %NA^-2
Ms = 0.622e6; %Am^-1
DSyy = 0.0; %Pa^-1
sigma_b = -15e6; %Pa
epsilon_th = -60000e-6;
epsilon_M = [-4100e-6;-1500e-6*.65;-620*.65];

epsilon_sp_p = [-4050e-6;-1265e-6;-730e-6;-455e-6];
sigma_p_p = [-0.0121e6; -0.62e6; -1.79e6; -4.15e6];
H1_p = [12e3;10e3;11e3;10e3]; %A/m
epsilon_2_p = [-625e-6;-250e-6;-90e-6;-31e-6];
H3_p = [180e3;125e3;180e3;250e3]; %A/m

p = 1;
epsilon_sp = epsilon_sp_p(p);
sigma_p = sigma_p_p(p);
H1 = H1_p(p);
epsilon_2 = epsilon_2_p(p);
H3 = H3_p(p);
epsilon_M = epsilon_M_p(p);

Yxi = 2.0957e+005;
n = 1.5;

% Inputs

h = 1e3;
Hy = 650e3*sin([0:.01:pi]);
sigma_a = -0.0125e6;
ss = 'b';

% Calculate Needed Coefficients

k2 = mu_0*Ms*H3*epsilon_th/2/(epsilon_sp - epsilon_2)
k1 = n*k2;
c1 = epsilon_sp.*sigma_p + 1/2*DSyy.*sigma_p.^2 + mu_0*Ms*H1 - Yxi
c2 = epsilon_sp.*sigma_p + 1/2*DSyy.*sigma_p.^2 + Yxi -
    2*k2.*epsilon_2./epsilon_th
epsilon_s0 = epsilon_sp*sigma_b^2/(sigma_p-sigma_b)^2

% The Equations

epsilon_s = epsilon_s0*((sigma_a/sigma_b)^2-2*sigma_a/sigma_b+1);
xi_up = 1/(2*k1)*(epsilon_s*sigma_a+0.5*DSyy*sigma_a^2+mu_0*
    Ms*Hy(1:ceil(.5*length(Hy)))-c1-Yxi);
xi_down = 1/(2*k2)*(epsilon_s*sigma_a+0.5*DSyy*sigma_a^2+mu_0*
    Ms*Hy(ceil(.5*length(Hy)):length(Hy))-c2+Yxi);

% Finding the section break points

xi_s = epsilon_s/epsilon_th;

[i1] = find(abs(xi_up) > abs(xi_s));
[i2] = find(abs(xi_down) < abs(xi_s));

if isempty(i1)
    i1(1) = length(xi_up);
end

```

```

if isempty(i2)
    i2(1) = length(xi_down);
end

% Truncating and Combining the data

xi_up_keep = xi_up(1:(i1(1)-1));
xi_down_keep = xi_down(i2(1):length(xi_down));
mid_len = length(Hy)-length(xi_up_keep)-length(xi_down_keep);
xi = [xi_up_keep,xi_s.*ones(1,mid_len),xi_down_keep];

% Convert to Strain

eps_mod = epsilon_th.*xi;

```



## BIBLIOGRAPHY

- [1] F. Ahmadkhanlou, G. Washington, Y. Wang, and S. Bechtel. The development of variably compliant haptic systems using magnetorheological fluids. *Proceedings of SPIE Smart Structures and Materials Conf.*, 5757:491–502, March 2005.
- [2] Answers.com and Wikipedia. Smart material. [http:// www.answers.com/ topic/ smart-material](http://www.answers.com/topic/smart-material), Nov. 2005.
- [3] K Bhattacharya and RV Kohn. Symmetry, texture and the recoverable strain of shape-memory polycrystals. *Acta Mater.*, 44(2):529–542, 1996.
- [4] Richard M. Bozorth. *Ferromagnetism*. D. Van Nostrand Company, Inc, New York, 1951.
- [5] VD Buchel’nikov, VS Romanov, AN Vasil’ev, T Takagi, and VG Shavraov. Model of colossal magnetostriction in the martensite phase of ni-mn-ga alloys. *Journal of Experimental and Theoretical Physics*, 93(6):1302–1306, 2001.
- [6] WJ. Buehler, JV. Gilfrich, and RC. Wiley. Effect of low-temperature phase changes on the mechanical properties of alloys near composition tni. *Journal of Applied Physics*, 34:1475, 1963.
- [7] Brice Carnahan, H.A. Luther, and James O. Wikes. *Applied Numerical Methods*. Wiley, New York, 1969.
- [8] V.A. Chernenko, V.A. L’vov, and E. Cesari. Martensitic transformation in ferromagnets: experiment and theory. *Journal of Magnetism and Magnetic Materials*, (196-197):859–860, 1999.
- [9] Soshin Chikazumi. *Physics of Magnetism*. Wiley Series on the Science and Technology of Materials. John Wiley & Sons, Inc, New York, 1964.
- [10] A.E. Clark. *Ferromagnetic Materials*, chapter 7: Magnetostrictive Rare Earth-Fe<sub>2</sub> Compounds, pages 531–589. North Holland Publishing Company, 1980.

- [11] AE Clark, JB Restorff, M Wun-Fogle, TA Lograsso, and DL Schlager. Magnetostrictive properties of body-centered cubic fe-ga and fe-ga-al alloys. *IEEE Transactions on Magnetics*, 36(5):3238, 2000.
- [12] Chemical Rubber Company. *CRC Standard Mathematical Tables and Formulae*. CRC Press, Boca Raton, 30 edition, 1996.
- [13] R.D. Cullity. *Introduction to Magnetic Materials*. Addison-Wesley Series in Metallurgy and Materials. Addison-Wesley Publishing Company, 1 edition, 1972.
- [14] Marcelo J. Dapino, Frederick T. Calkins, and Alison B. Flatau. Measured Terfenol-D material properties under varied applied magnetic field levels. *Proceedings of SPIE Smart Structures and Materials Conf.*, 2717(66), 1996a.
- [15] MJ Dapino. *Encyclopedia of Smart Materials*, chapter Magnetostrictive Materials: Their Use in Smart Structure Applications, pages 600–620. John Wiley & Sons, Inc., New York, 2002.
- [16] MJ Dapino, RC Smith, LE Faidley, and AB Flatau. A coupled structural-magnetic strain and stress model for magnetostrictive transducers. *Journal of Intelligent Material Systems and Structures*, 11(2):135–152, Feb 2000.
- [17] MJ Dapino, RC Smith, and AB Flatau. Structural-magnetic strain model for magnetostrictive transducers. *IEEE Transactions on Magnetics*, 36(3):545–556, May 2000.
- [18] T Duerig, D Stoeckel, and D Johnson. Sma: smart materials for medical applications. *Proceedings of SPIE European Workshop on Smart Structures in Engineering and Technology*, 4763:7–15, 2003.
- [19] LE Faidley, MJ Dapino, GN Washington, and TA Lograsso. Reversible strain in Ni-Mn-Ga with colinear field and stress. *Proc. SPIE Smart Structures and Materials*, (5761):501–512, 2005.
- [20] LeAnn E. Faidley, Marcelo J Dapino, Gregory N Washington, and Thomas A. Lograsso. Dynamic response in the low-kHz range and Delta-E effect in ferromagnetic shape memory Ni-Mn-Ga. *Proceedings of IMECE 2003*, (43198), 2003.
- [21] Alison B. Flatau, Marcelo J. Dapino, and Frederick T. Calkins. High bandwidth tunability in a smart vibration absorber. *J. Intell. Mater. Syst. and Struct.*, 11(12):923–929, Dec 2000.
- [22] FX Gil, JM Manero, and JA Planell. Relevant aspects in the clinical applications of niti shape memory alloys. *Journal of Materials Science: Materials in Medicine*, 7(7):403–406, July 1996.

- [23] DL Hall and AB Flatau. Broadband performance of a magnetostrictive shaker. *Journal of Intelligent Material Systems and Structures*, 6(1):109–116, Jan 1995.
- [24] O. Heczko and K. Ullakko. Effect of temperature on magnetic properties of  $Ni - Mn - Ga$  magnetic shape memory (MSM) alloys. *IEEE Transactions on Magnetics*, 37(4):2672–2674, July 2001.
- [25] L Hirsinger and C Lexcellent. Modelling detwinning of martensite platelets under magnetic and (or) stress actions on nimnga alloys. *Journal of Magnetism and Magnetic materials*, 254-255:275–277, 2003.
- [26] R.D. James and R. Tickle. Large field-induced strains in ferromagnetic shape memory materials. *Materials Science and Engineering A (Switzerland)*, 273-275:320–325, Dec 1999.
- [27] R.D. James and M. Wuttig. Alternative smart materials. *Proceed. of SPIE Symposium on Smart Structures and Materials 1996*, 2715:420–426, March 1996.
- [28] R.D. James and M. Wuttig. Magnetostriction of martensite. *Philosophical Magazine A*, 77(5):1273–1299, 1998.
- [29] David Jiles. *Magnetism and Magnetic Materials*. Chapman & Hall, 1995.
- [30] X. Jin, M. Marioni, D Bono, S.M. Allen, R.C. O’Handley, and T.Y. Hsu. Empirical mapping of Ni-Mn-Ga properties with composition and valence electron concentration. *Journal of Applied Physics*, 91(10), May 2002.
- [31] MR Jolly. Properties and applications of commercial magnetorheological fluids. *Journal of Intelligent Material Systems & Structures*, 10(1):5, 1999.
- [32] T Kakeshita, K Shimizu, S Funada, and M Date. Magnetic field-induced martensitic transformations in disordered and ordered fe-pt alloys. *Transactions of Japan Insitute of Metals*, 25:837–844, 1984.
- [33] H. Kato, Y. Liang, and M. Taya. Stress-induced fcc/fct phase transformation in fe-pd alloy. *Scripta Materialia*, 46:471–475, 2002.
- [34] H Kato, T Wada, Y Liang, T Tagawa, M Taya, and T Mori. Martensite structure in polycrystalline fe-pd. *Materials Science and Engineering*, A332:134–139, 2002.
- [35] RA Kellogg. *Development and modeling of iron gallium alloys*. PhD thesis, Iowa State University, Ames, IA, 2003.
- [36] Rick Allen Kellogg. *Delta-E effect in Terfenol-D and its application in a tunable mechanical resonator*. PhD thesis, Iowa State University, 2000.

- [37] B Kiefer and D Lagoudas. Modeling of the magnetic field-induced martensitic variant reorientation and the associated magnetic shape memory effect in msma. *Proceedings of SPIE Smart Structures and Materials Conf.*, 5761:454–465, 2005.
- [38] B Kiefer and D Lagoudas. Magnetic field-induced martensitic variant reorientation in magnetic shape memory alloys. *Philosophical Magazine*, forthcoming.
- [39] Bjorn Kiefer and Dimitris C. Lagoudas. Phenomenological modeling of ferromagnetic shape memory alloys. *Proceedings of SPIE Smart Structures and Materials Conf.*, 5387:164–176, July 2004.
- [40] A. Kumada. A piezoelectric ultrasonic motor. *Japanese Journal of Applied Physics*, 24:739, 1986.
- [41] N Lanska, O Soderberg, A Sozinov, Y Ge, K Ullakko, and VK Lindroos. Composition and temperature dependence of the crystal structure of ni-mn-ga alloys. *Journal of Applied Physics*, 95(12):8074 – 8078, June 2004.
- [42] Y Liang, T Wada, H Kato, T Tagawa, M Taya, and T Mori. Straining of a polycrystal of fe-pd with martensite structure by uniaxial loading. *Materials Science and Engineering*, A338:89–96, 2002.
- [43] A.A. Likhachev, A. Sozinov, and K. Ullakko. Influence of external stress on the reversibility of magnetic-field-controlled shape memory effect in Ni-Mn-Ga. *Proceedings of SPIE Smart Structures and Materials Conf.*, 4333:197–206, 2001.
- [44] A.A. Likhachev and K. Ullakko. Quantitative model of large magnetostrain effect in ferromagnetic shape memory alloys. *EPJdirect B2*, pages 1–9, 1999.
- [45] A.A. Likhachev and K. Ullakko. Magnetic-field-controlled twin boundaries motion and giant magneto-mechanical effects in Ni-Mn-Ga shape memory alloy. *Physics Letters A*, (275):142–151, October 2000.
- [46] A.A. Likhachev and K. Ullakko. Quantitative model of large magnetostrain effect in ferromagnetic shape memory alloys. *Eur. Phys. J B*, (14):263–267, 2000.
- [47] A.A. Likhachev and K. Ullakko. The model of magnetic-field-controlled shape memory effect in *NiMnGa*. *J. Phys. IV France*, 11(Pr8):293–298, 2001.
- [48] A. Likhachev and K. Ullakko. The model development and experimental investigation of giant magneto-mechanical effects in *Ni – Mn – Ga*. *Journal of Magnetism and Magnetic Materials*, 226-230(2):1541–1543, May 2001.
- [49] V.A. L’vov, E.V. Gomonaj, and V.A. Chernenko. A phenomenological model of ferromagnetic martensite. *J. Phys.: Condens. Matter*, 10:4587–4596, 1998.

- [50] V.A. L'vov, S.P Zagorodnyuk, and V.A. Chernenko. A phenomenological theory of giant magnetoelastic response in martensite. *Eur. Phys. J B*, (27):55–62, 2002.
- [51] A. Malla. Effect of composition of the magnetic and elastic properties of shape memory Ni-Mn-Ga. Master's thesis, The Ohio State University, June 2003.
- [52] A. Malla, M. Dapino, and T. Lograsso. Effect of composition on the magnetic and elastic properties of shape memory NiMnGa. *Proceedings of SPIE Smart Structures and Materials Conf.*, March 2003.
- [53] A. Malla, MJ Dapino, TA Lograsso, and DL Schlagel. Large magnetically-induced strains in  $Ni_{50}Mn_{28.7}Ga_{21.3}$  driven with collinear field and stress. *Journal of Applied Physics*, (In review).
- [54] Lawrence E. Malvern. *Introduction to the Mechanics of a Continuous Medium*. Prentice-Hall, Inc, 1969.
- [55] J Manzo, E Garcia, A Wickenheiser, and G Horner. Design of a shape-memory alloy actuated macro-scale morphing aircraft mechanism. *Proceedings of SPIE Smart Structures and Materials Conf.*, 5764:232–240, 2005.
- [56] Miguel A. Marioni, Samuel M. Allen, and Robert C. O'Handley. Nonuniform twin-boundary motion in Ni-Mn-Ga single crystals. *Applied Physics Letters*,, 84(20):4071 – 4073, May 2004.
- [57] MIDE. Smart material consulting. [http://www.mide.com/serv\\_smart\\_materials\\_consulting.html](http://www.mide.com/serv_smart_materials_consulting.html), Nov. 2005.
- [58] Y. Murakami and D. Shindo. Magnetic domain structure in a ferromagnetic shape memory alloy  $ni_{51}fe_{22}ga_{27}$  studied by electron holography and lorentz microscopy. *Applied Physics Letters*, 82(21):3695 – 3697, May 2003.
- [59] S.J. Murray, M. Farinelli, C. Kantner, J.K. Huang, S.M. Allen, and R.C. O'Handley. Field-induced strain under load in  $Ni - Mn - Ga$  magnetic shape memory materials. *Journal of Applied Physics*, 83(11):7297–7299, June 1998.
- [60] S.J. Murray, M. Marioni, S.M. Allen, R.C. O'Handley, and T.A. Lograsso. 6% magnetic-field-induced strain by twin-boundary motion in ferromagnetic Ni-Mn-Ga. *Applied Physics Letters*,, 77(6):886–888, 2000.
- [61] S.J. Murray, M. Marioni, P.G. Tello, S.M. Allen, and R.C. O'Handley. Giant magnetic-field-induced strain in Ni-Mn-Ga crystals: experimental results and modeling. *Journal of Magnetism and Magnetic Materials*,, 226-230:945–947, May 2001.

- [62] S.J. Murray, M.A. Marioni, A.M. Kukla, J. Robinson, R.C. O’Handley, and S.M. Allen. Large field induced strain in single crystalline  $Ni - Mn - Ga$  ferromagnetic shape memory alloy. *Journal of Applied Physics*, 87(9):5774–5776, May 2000.
- [63] S.J. Murray, R.C. O’Handley, and S.M. Allen. Model for discontinuous actuation of ferromagnetic shapem memory alloy under stress. *Journal of Applied Physics*, 89(2):1295–1301, Jan 2001.
- [64] VA Neelakantan, GN Washington, and NK Bucknor. Two-stage actuation system using dc motors and piezoelectric actuators for controllable industrial and automotive brakes and clutches. *Proceedings of SPIE Smart Structures and Materials Conf.*, 5762:275–286, March 2005.
- [65] DT Nosse and MJ Dapino. Compact actuation through magnetorheological flow control and rectification of magnetostrictive vibrations. *Proceedings of SPIE Smart Structures and Materials Conf.*, 5764:262–273, 2005.
- [66] C.J. O’Connor, V.O. Golub, A.Y. Vovk, V.V. Kotov, P.Yakovenko, and K. Ulakko. Influence of thermal treatment of local structure and magnetic properties of  $Ni - Mn - Ga$  alloys. *IEEE Transactons on Magnetics*, 38(5):2844–2846, Sept 2002.
- [67] R.C. O’Handley. *Modern Magnetic Materials: Principles and Applications*. John Wiley & Sons, Inc., 2000.
- [68] Rorbert C O’Handley. Model for strain and magnetization in magnetic shape-memory alloys. *Journal of Applied Physics*, 83(6):3263–3270, March 1998.
- [69] Rorbert C. O’Handley, S.J. Murray, Miguel A. Marioni, H. Nembach, and S.M. Allen. Phenomenology of giant magnetic-field induced strain in ferromagnetic shape-memory materials. *J. Appl. Phys.*, 87(9):4712–4717, May 2000.
- [70] K Oikawa, T Ohta, F Gijima, T Ohmori, R Kainuma, and K Ishida. Phase equilibria and phase transformations in new b2-type ferromagnetic shape memory alloys of co-ni-ga and co-ni-al systems. *Materials Transactions*, 42:2472–2475, 2001.
- [71] K Oikawa, L Wulff, T Iijima, G Gejima, T Ohmori, A Fujita, K Fukamichi, R Kainuma, and K Ishida. Promissing ferromagnetic ni-co-al shape memory alloy system. *Applied Physics Letters*, 81:3290–3292, 2001.
- [72] M. Pasquale, C. Sasso, S. Besseghini, F. Passaretti, and E. Villa. Effect of texturing on magnetically activated properties of polycrystalline  $NiMnGa$  alloys. *Preprint Journal de Physique, ESOMAT (Como)*, Sept 2000.

- [73] M. Pasquale, C.P. Sasso, S. Beseghini, F. Passaretti, and E. Villa. *NiMnGa* polycrystalline magnetically activated shape memory alloys. 2000.
- [74] Jason Paulsen. *Private Correspondence from DoE - Ames Lab - Magnetism Focus*. August 2003.
- [75] Jim Restorff. *Private Correspondence from Naval Surface Warfare Center - Magnetic Materials Group*. December 2003.
- [76] Marc L. Richard. *Systematic analysis of the crystal structure, chemical ordering, and microstructure of Ni-Mn-Ga ferromagnetic shape memory alloys*. PhD thesis, Massachusetts Institute of Technology, Sept. 2005.
- [77] VG Shavraov, AA Glebov, IE Dikshtein, VV Koledov, DA Kosolapov, EP Krasnoperov, T Takagi, AA Tulaykova, and AA Cherechukin. Observation of the one-way shape memory effect in ni-mn-fe-ga heusler alloy due to the magnetic field induced martensite-austenite transition. *Journal of Radioelectronics*, (5), 2001.
- [78] Ralph C. Smith. Modeling techniques for magnetostrictive actuators. *Proceedings of SPIE Symposium on Smart Structures and Materials*, 3041:24–253, March 1997.
- [79] Ralph C. Smith. *Smart Material Systems: Model Development*. Society for Industrial & Applied Mathematics, Philadelphia, PA, 2005.
- [80] Ralph C. Smith and Jordan E. Massad. A unified methodology for modeling hysteresis in ferroelectric, ferromagnetic, and ferroelastic materials. Technical Report CRSC-TR01-10, CRSC, NC State, April 2001.
- [81] Ralph C. Smith, Stefan Seelecke, Zoubeida Ounaies, and Joshua. Smith. A free energy model for hysteresis in ferroelectric materials. *Journal of Intelligent Material Systems and Structures*,, to appear.
- [82] RC Smith and MJ Dapino. A stress-dependent hysteresis model for ferromagnetic transducer materials. *Proc. ASME, Orlando, FL*, IMECE2005(80394), 2005.
- [83] RC Smith, MJ Dapino, TR Braun, and AP Mortensen. A homogenized energy framework for ferromagnetic hysteresis. *IEEE Transactions on Magnetics*, (in review).
- [84] Alexei Sozinov, A.A. Likhachev, N. Lanska, and Kari Ullakko. Giant magnetic-field-induced strain in NiMnGa seven-layered martensitic phase. *Applied Physics Letters*,, 80(10):1746–1748, March 2002.

- [85] AV Srinivasan and DM McFarland. *Smart Structures: Analysis and Design*. Cambridge University Press, 2001.
- [86] R. Tickle, R.D James, T. Sheild, M. Wuttig, and V.V Kokorin. Ferromagnetic shape memory in the NiMnGa system. *IEEE Trans. Magn*, 35:4301–4310, 1999.
- [87] R. Tickle, R.D. James, T. Shield, and P. Schumacher. Ferromagnetic shape memory in the *NiMnGa* system. *Submitted to J. Applied Physics*, 1997.
- [88] Robert Tickle. *Ferromagnetic Shape Memory Materials*. PhD thesis, Texas A&M, 2000.
- [89] K. Ullakko. Magnetic control of shape memory effect. In *International Conference on Martensitic Transformations ICOMAT-95*, Lausanne, Switzerland, 20-25 August 1995. Ecole Polytechnique Federale de Lausanne.
- [90] K. Ullakko. Large-stroke and high-strength actuator materials for adaptive structures. In *Proc. of 3rd International Conference on Intelligent Materials and 3rd European Conference on Smart Structures and Materials*, Lyon, France, June 1996. INSA de Lyon, France and University of Stratchlyde, UK.
- [91] K. Ullakko, P.T. Jakovenko, and V.G. Gavriljuk. New developments in actuator materials as reflected in magnetically controlled shape memory alloys and high-strength shape memory steels. *Proc. of Symposium on Smart Structures and Materials*, Feb 1996.
- [92] Kari Ullakko. Magnetically controlled shape memory alloys: A new class of actuator materials. *Journal of Materials Engineering and Performance*, 5(3):405–409, June 1996.
- [93] Kari Ullakko, J.K. Huang, C. Kantner, R.C. O’Handley, and V.V. Kokorin. Large magnetic-field-induced strains in Ni<sub>2</sub>MnGa single crystals. *Appl. Phys. Lett.*, 69(13):1966–1968, September 1996.
- [94] T Wada, T Tagawa, and M Taya. Martensitic transformation in pd-rich fe-pd-pt alloy. *Scripta Materialia*, 48:207–211, 2003.
- [95] G.N. Washington. Introduction to smart materials and intelligent systems: Me 774 class notes. 2002.
- [96] CM Wayman and TW Duerig. *Engineering Aspects of Shape Memory Alloys*, chapter An Introduction to Martensite and Shape Memory, pages 3–20. Butterworth-Heinemann, 1990.
- [97] M Wuttig, J Li, and C Craciunescu. A new ferromagnetic shape memory alloy system. *Scripta Materialia*, 44:2393–2397, 2001.